UNIVERSITY OF SOUTHAMPTON

FACULTY OF PHYSICAL SCIENCES AND ENGINEERING

School of Electronics and Computer Science

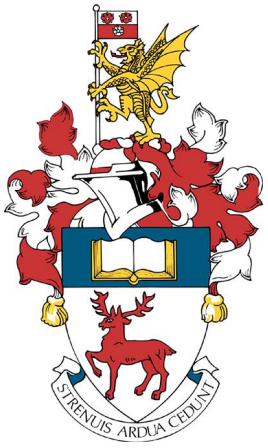

Investigation of High Current Heaterless Hollow Cathode Ignition

by

Alexander J.N. Daykin-Iliopoulos

Supervised by:

Professor Steve B. Gabriel and Dr Igor O. Golosnoy

Thesis for the degree of Doctor of Philosophy

April 2019

UNIVERSITY OF SOUTHAMPTON

ABSTRACT

FACULTY OF PHYSICAL SCIENCES AND ENGINEERING

Thesis for Doctor of Philosophy

INVESTIGATION OF HIGH CURRENT HEATERLESS HOLLOW CATHODE IGNITION

Alexander J.N. Daykin-Iliopoulos

The development of long life high powered hollow cathodes is of importance to meet the demand of increasingly powerful Gridded Ion Engines and Hall Effect Thrusters. High current (≥30 A) cathodes typically operate with a LaB_6 emitter which operates at higher temperatures than a BaO-W emitter, thus posing a significant challenge for heater reliability. The heater component commonly used to raise the emitter to thermionic temperatures, has inherent reliability issues from thermal fatigue caused by the thermal cycling with large temperature variations. A self-heating hollow cathode allows for potentially higher reliability through the design simplicity of removing the heater component. This also results in significant cost savings, as well as savings in the mass, volume, ignition time and ignition power.

To investigate heaterless ignition, a novel high current heaterless hollow cathode (HHC) has been designed, constructed, and tested. Critically this system for the first time, controls the discharge current rise and attachment through heaterless ignition, to maintain a diffusive heating discharge that raises the emitter to the thermionic temperatures, without discharge localisation that can lead to high erosion and melting. The developed system successfully demonstrated operation up to 30 A, achieving proof of concept. This system also overcomes the need for excessive ignition voltages or propellant pulsing, with a reduced keeper orifice that enables ignition with <350 V, and nominal flow rates (<15 sccm). The system has also demonstrated full ignition in 50 seconds compared with conventional ignition which can require >15 minutes; additionally, the system requires as little as $1/6^{th}$ of the ignition energy compared to that of conventional ignitions.

The novel HHC's performance was characterised for the breakdown, heating, transition and thermionic phases of ignition, with operation tested in Xe, Ar and Kr. Thermocouples placed along the emitter axis provided emitter thermal profile trends through ignition and optical pyrometry has allowed measurements of the emitter tip temperature of an HHC for the first time. The internal cathode-keeper plasma has been investigated using optical emission spectroscopy to determine the plasma electron density.

TABLE OF CONTENTS

LIST OF TABLES

LIST OF FIGURES

ACADEMIC THESIS: DECLARATION OF AUTHORSHIP

I, Alexander J. N. Daykin-Iliopoulos declare that this thesis entitled *Investigation of High Current Heaterless Hollow Cathode Ignition* and the work presented in it are my own and has been generated by me as the result of my own original research.

I confirm that:

1. This work was done wholly or mainly while in candidature for a research degree at this University;
2. Where any part of this thesis has previously been submitted for a degree or any other qualification at this University or any other institution, this has been clearly stated;
3. Where I have consulted the published work of others, this is always clearly attributed;
4. Where I have quoted from the work of others, the source is always given. With the exception of such quotations, this thesis is entirely my own work;
5. I have acknowledged all main sources of help;
6. Where the thesis is based on work done by myself jointly with others, I have made clear exactly what was done by others and what I have contributed myself;
7. Parts of this work have been published as: [1-8]

Signed: .....

Date:.....

ACKNOWLEDGEMENTS

I would like to thank my main supervisor Prof. Steve Gabriel for his mentorship and guidance throughout this project. He regularly comes to the laboratory to provide technical advice and critically, the moral support to persevere with the experiments, despite significant setbacks and challenges commonly faced within such research. His general enthusiasm for work and life has made it inspiring and joyful to work with.

In addition, I am indebted to my secondary supervisor Dr. Igor Golosnoy, for constantly providing his plasma physics expertise, which immensely aided this project. When entering his office for a quick question, you often find yourself leaving hours later, though always significantly enlightened after in-depth discussions on plasma physics theory. It has been a pleasure to work with such a learned researcher with unwavering passion for learning coupled with his characteristic Russian humour.

I would like to express my gratitude to the Tony Davis High Voltage Laboratory, led by Paul Lewin and Neil Palmer, for their assistance in the facility set-up and technical support, also thanks to the ECS workshop led by Mark Long, for fabrication, construction and modification of the heaterless hollow cathode models.

Also, I am grateful to Kenichi Kubota and Ikkoh Funaki from the Japan Aerospace Exploration Agency (JAXA) for providing valuable experimental and modelling assistance, as well as guidance from their past electric propulsion experiences. In addition, thanks are due to Franco Bosi from Mars Space Ltd (MSL), who gave huge support in spectrographic analysis.

I would also like to thank the members of our electric propulsion group for technical brainstorming and moral support. Starting with those who have been here the longest, Cristian Dobranszki, Fabio Coccaro, Nazareno Fazio and Duncan Bell. Also, I would like to thank the other office mates both at the UoS and MSL, who I often lunched with and shared a very enjoyable working environment together.

I owe a great debt of gratitude to my family, who supported me through this, at times, arduous PhD process. Finally, I am indebted to my partner Xinyang Lu who I met during this PhD and who continually supported and assisted me through the process.

NOMENCLATURE

A	=	Richardson's constant (120 A cm^{-2} K^{-2})
A_g	=	Townsend experimentally determined gas property (cm^{-1} $Torr^{-1}$)
$A_\emptyset$	=	Orifice cross-sectional area (m^2)
B	=	Material specific correction factor
B_g	=	Townsend experimentally determined gas property (V cm^{-1} $Torr^{-1}$)
C	=	Capacitance (F)
D	=	Corrected Richardson's constant (A cm^{-2} K^{-2})
E	=	Electric field (V m^{-1})
E_S	=	Emitter evaporation rate (kg s^{-1})
I	=	Current (A)
J	=	Current density (A m^{-2})
J_C	=	Current density at the cathode (A m^{-2})
J_{Cl}	=	Space charge limited current density (A m^{-2})
L_e	=	Emitter lifetime (s)
M_a	=	Atomic mass (u)
M_e	=	Electron mass (~$9.109*10^{-31}$ kg)
N	=	Gas density (kg m^{-3})
Q	=	Stored charge (C)
R	=	Circuit resistance (Ω)
R_g	=	Gas constant (8.314 J mol^{-1} K^{-1})
R_p	=	Plasma discharge resistance (Ω)

S	=	Exposed emitter surface (m^2)
S_A	=	Emitter surface area (m^2)
S_{ID}	=	Emitter inner diameter (m)
S_L	=	Emitter length (m)
S_{OD}	=	Emitter outer diameter (m)
S_V	=	Emitter surface volume (m^3)
S_{real}	=	Real surface area (m^2)
S_{mod}	=	Model surface area (m^2)
T	=	Temperature (K)
T_e	=	Electron temperature (K)
T_g	=	Gas temperature (K)
T_i	=	Indicated temperature (K)
V	=	Voltage (V)
V_A	=	Anode fall voltage (V)
V_B	=	Breakdown voltage (V)
$V_{B_{min}}$	=	Minimum breakdown voltage (V)
V_a	=	Anode discharge voltage (V)
V_c	=	Cathode fall voltage (V)
V_k	=	Keeper discharge voltage (V)
V_p	=	Plasma discharge voltage (V)
V_s	=	Supply voltage (V)
a_{eff}	=	Atomic radius (m)
c	=	Speed of light in the medium ($2.998*10^5$ m s^{-1})

d	=	Distance between electrodes (m)
d_c	=	Cathode fall thickness (m)
$d_\emptyset$	=	Orifice diameter (m)
e	=	Electron charge (~$1.602*10^{-19}$ C)
j_s	=	Energy per time per area (W m^{-2})
k	=	Thermal conductivity
k_b	=	Boltzmann constant (~$1.381*10^{-23}$ m^2 kg s^{-2} K^{-1})
$l_\emptyset$	=	Orifice length (m)
$\dot{m}$	=	Mass flow rate (kg s^{-2})
m_e	=	Emitter mass (kg)
n_e	=	Plasma electron density (m^{-3})
p	=	Pressure (Pa)
$\vec{q}$	=	local heat flux density (W m^{-2})
w	=	Emission spectrum full width at half maximum (m)
α	=	Experimentally found constant
γ_c	=	Heat capacity ratio
γ_{se}	=	Secondary electron emission coefficient
ε	=	Emissivity
ε_{eff}	=	Effective emissivity
ε_F	=	Fermi energy (eV)
ε_{iz}	=	Ionization potential of the primary ion (eV)
ε_e	=	Electron energy (eV)
ε_Φ	=	Surface work function (eV)

ϵ_0	=	Vacuum permittivity (~$8.85*10^{-12}$ F m^{-1})
ζ	=	Optical transmittance
$\emptyset$	=	Temperature dependent work function (eV)
$\emptyset_o$	=	Classical work function (eV)
λ	=	Wavelength (m)
μ_i	=	Ion mobility (m^2 s^{-1} V^{-1})
ξ	=	Viscosity (kg m^{-1} s^{-1})
π	=	Mathematical constant (~3.142)
ρ_e	=	Emitter density (kg m^{-3})
σ	=	Stefan-Boltzmann constant ($5.670*10^{-8}$ kg s^{-3} K^{-4})
ψ_e	=	Emitter relative density ratio

DEFINITIONS AND ABBREVIATIONS

EP	=	Electric propulsion
ESA	=	European Space Agency
GEO	=	Geosynchronous equatorial orbit
GIE	=	Gridded ion engines
HC	=	Hollow cathodes
HET	=	Hall effect thrusters
HHC	=	Heaterless hollow cathode
IAT	=	Ion acoustic turbulence
ICS	=	Ignition control system
JAXA	=	Japan Aerospace Exploration Agency
LEO	=	Low earth orbit
MFC	=	Mass flow rate
MSL	=	Mars Space Ltd.
NASA	=	National Aeronautics and Space Administration
sccm	=	Standard cubic centimetres per minute
TRL	=	Technology readiness level

CHAPTER 1

INTRODUCTION

1.1 ELECTRON SOURCES

Electron emission is both a fundamental interest and an enabling tool for physicists and engineers in numerous fields. Thomas Edison discovered electron emission in 1880 [9] with a modified incandescent lightbulb which incorporated an additional electrode connected to a galvanometer, which as the bulb current increased to sufficiently high magnitudes the galvanometer began to deflect due to current passing through its coils [10]. Prior reporting of the phenomenon was made by E. Becquerel in 1853 [10, 11], though the field did not progress until Edison's re-discovery and thus the phenomenon was referred to at the time as the Edison effect, and more recently is known as thermionic emission of electrons. One of the first devices utilising this effect was the vacuum tube diode patented by Fleming in 1904 [12]. Today electron sources are an essential part of life, utilised in countless wide-ranging devices, such as, microwave ovens, radar, electron microscopes, particle accelerators and spacecraft propulsion.

These electron sources use one or a combination of emission mechanisms, such as, thermal, field, photo and secondary electron emission as well as the collisional plasma ionisation mechanism. All of which are mechanisms for raising the electron energy to overcome the work function or ionisation energy of the medium. Once the electrons are emitted, they are typically manipulated electrostatically and/or electromagnetically for the intended application.

The applicability of each emission mechanisms for a given purpose, is determined by the governing parameters of the respective mechanisms. In the early 1900's equations were formed for predicating the emission generated via these emission mechanisms. Although generalisations

and modifications to the canonical form of these equations has taken place over the last century, and continue to do so, their scientific popularity and widespread use is testimony to their reasonable account of the phenomena [13]. However, clear understanding of these equations' accuracy, limits and assumptions are paramount for appropriate implementation. Below is a summary table of the main emission mechanisms and their typical applications.

Table 1.1: Overview of surface emission electron sources

Electron emission mechanism	Predictive operating principle	Typical operational configurations	Example applications
Thermionic	Richardson–Laue–Dushman, Child-Langmuir law	Filament (directly and indirectly heated), hollow cathode	Electron lithography, X-Ray sources, scanning electron microscope, space propulsion
Photoemission	Fowler–DuBridge	Photocathode	Photomultipliers, Photospectroscopy, night vision, free electron lasers
Field emission	Fowler-Nordheim	Needle, Field emitter arrays	Field effect scanning microscopes
Secondary electron emission	Baroody	Radio Frequency cathodes	Material coating

1.2 SPACECRAFT PROPULSION ELECTRON SOURCES

Electron sources are an essential component of in-space electric propulsion (EP) systems, such as Gridded Ion Engines (GIEs) and Hall Effect Thrusters (HETs). In-space electron sources were demonstrated with the first GIE flight operation on the NASA SERT-1 spacecraft in 1964 [14]. EP use in satellites has been growing ever since and today is a mature and widely used technology. This growth has predominantly been driven by increasing demand for cost-effective commercial geostationary orbiting (GEO) telecommunication satellites, with currently over 15 such launches per year [15]. However, there is also increasing EP utilisation for deep-space scientific missions, such as the NASA Dawn and the ESA BepiColombo missions. Finally, prominently coming into the field are mini-satellite mega constellations such as the OneWeb constellation with around nine

hundred 150 kg satellites planned for launch from 2019-2021 and over 1500 additional satellites under consideration for network expansion [16]. This is set to drastically increase the number of EP system flights.

For these space propulsion applications, the type of electron source overwhelmingly used is a thermionic cylindrical hollow cathode, referred within the space propulsion field simply as a *Hollow Cathode* (HC). The widespread use of this electron source type and geometry for EP is due to the demonstrated high emission currents (~1-300 A), lifetime (>5 years, 5000 cycles) and relatively low power usage (<50-500W).

Most GIEs require two HCs to operate, the first a *discharge cathode*, which provides electrons to ionise the propellant, thus enabling the ion beam generation and the second cathode a *neutraliser*, which emits electrons from the spacecraft to neutralise the charge build-up from the thruster's emitted ions. HETs alternatively utilise just one hollow cathode for the combined purpose, in addition to magnetically containing some of the electrons emitted, which in turn creates a space charge effect that accelerates the ions producing thrust.

1.2.1 CONVENTIONAL IN-SPACE HOLLOW CATHODES

Conventional in-space hollow cathodes consist of a cylindrical cathode tube with a constricting orifice at one end as shown in Figure 1.1. Typically, the cathode tube is constructed from refractory metal due to the high melting temperature and favourable mechanical properties. A low work emitter, which can also be referred to as an insert, is placed internally at the end of the cylindrical cathode tube. This emitter is traditionally made from a porous tungsten with impregnated barium oxide mixture (BaO-W) or lanthanum hexaboride (LaB_6), which is increasingly being used due to the reduced contamination issues, and especially for higher current cathodes due to the high current density ($> 10 \frac{A}{cm^2}$) with emission from the bulk material despite LaB_6 having a low but relatively higher work function (2.66 eV). Around the cathode tube there is a co-axial heater, which is used to heat the cathode tube and in-turn the emitter to thermionic emission temperatures. The heater is sheathed typically by ceramic to electrically isolate the heater from the cathode body. Around the heater, multi-layered insulation is used to assist in raising the emitter to emission temperatures via reducing the radiative loss - commonly multiple layers of tantalum or molybdenum foil is used, this material selection is common due to the low emissivity. An additional electrode is used to aid in maintaining and initiating the discharge and is referred to as a keeper. This keeper can enclose the hollow cathode or be an extraction orifice plate, that is placed downstream of the cathode orifice.

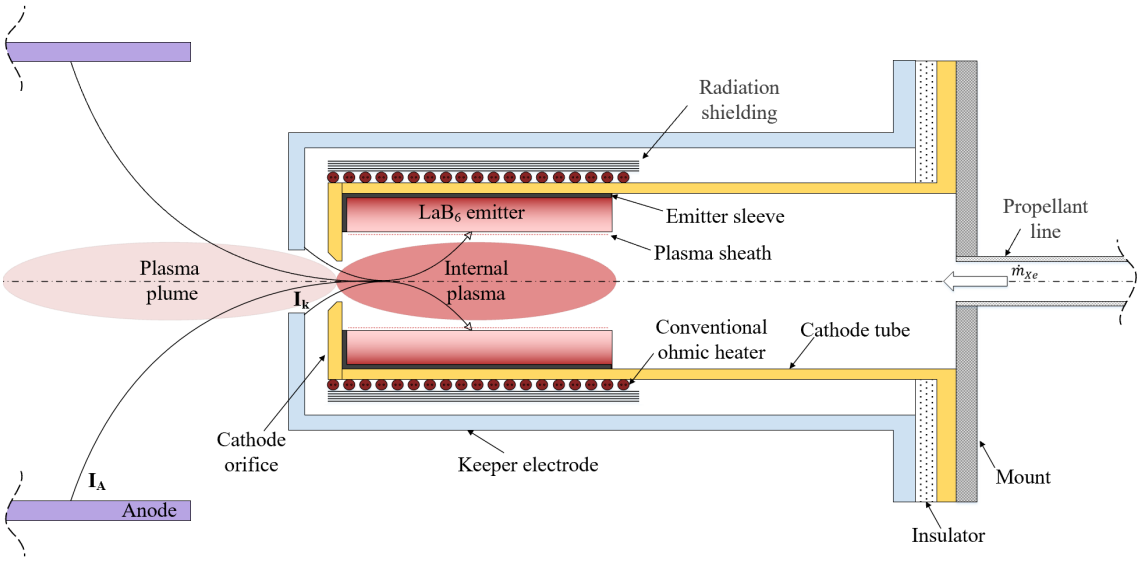

Figure 1.1: Schematic of a conventional in-space LaB_6 hollow cathode in anode mode testing.

Once the heater raises the emitter temperature to thermionic temperatures, propellant is fed through the cathode tube toward the constricting cathode orifice. Conventionally the propellant is a noble gas due to the low chemical reactivity. Xenon is predominantly used due to the low ionisation energy and high atomic mass, although historically mercury was used, and currently due to rising costs of xenon [17], krypton, argon [18] and gas mixture alternatives [19] are being tested. The propellant that is supplied is predominantly ionised through collisions with the thermionically emitted electrons. The electrons are then electrostatically extracted from the cathode by applying a potential to the keeper electrode. This keeper discharge is then transferred to an anode by applying a potential to the anode, delivering the emission current required. The anode testing mode shown in Figure 1.1 simulates operation with a given electric propulsion system, such as a HET or GIE.

The physics of the conventional cathode ignition is shown in Figure 1.2. First the emitter temperature is increased indirectly, through the cathode tube, by the heater. Secondly after sufficient heating time, 10-20 minutes, the emitter begins to non-negligibly thermionically emit electrons. Thirdly, with a keeper potential applied the emitted electrons partially ionise the propellant, which is injected through the cathode, this allows for a quasi-neutral plasma emission from the cathode orifice, which is therefore not space charge limited. Fourthly, the ions bombard the emitter, and this bombardment heats the emitter such that the heater component can be switched off, and the heat flux direction shown in Figure 1.2 reverses. The hollow cylinder cathode geometry allows for the hollow cathode effect [20], in which electron emission yields are increased by pendulum motion of the electrons within the hollow cylinder cathode.

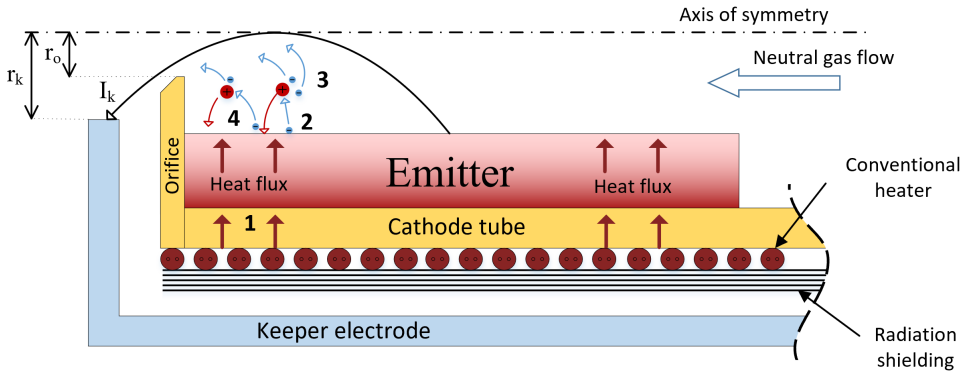

Figure 1.2: Schematic of conventional in-space hollow cathode ignition.

1.3 MOTIVATION FOR HEATERLESS HOLLOW CATHODE RESEARCH

As discussed, thermionic hollow cathodes depend upon ohmic heaters to raise the emitter temperature to 1200 – 1700 °C depending on the insert material used and discharge current required. A current state-of-the-art heater solution is where electric current passes through a resistive tungsten-rhenium wire coiled in an alumina ceramic support. Overall, the design attempts to minimise thermal shock effects, where the thermal gradients along a component are non-uniform causing differing expansion, and thus stressing the component. Additionally, it attempts to reduce the chance of shorting and maximise heat input to the emitter, however this heating system has several drawbacks:

1) Inherent reliability issues of the heater due to the thermal fatigue as a result of a high number of thermal cycles, which can be over 5000 [21, 22], compounded by the vibrational stress during launch and acceptance testing. Also the thermal fatigue is exacerbated by the large temperature variations which can be from ambient to as high as 1650 °C for a LaB_6 emitter, with a corresponding current density of 10 A/cm^2 [23] – this emitter type is increasingly being adopted internationally due to the easier handling requirements and the high emission densities achievable. The heater sub-component is a mission critical component, such that the failure of the heater incapacitates the cathode and thus in turn the whole propulsion system, hence potentially causing mission failure.
2) The heater requires extra complexity of the power processing unit (PPU) due to the additional supply and connections required, overall the heater adds extra mass and volume of the hollow cathode, which can be exacerbated by the addition of redundant heater components that have been added for some flight models due to the mentioned reliability issues [24, 25].
3) Significant portion of the hollow cathode cost is for the heater component, due to the specialised double sheathed spiral tungsten-rhenium wire construction and technical

placement on the cathode tube. In addition, there is large development costs for the heater, due to often having to undergo an individual qualification campaign as it is a mission critical sub-component.

4) Long ignition times in the order of 15 minutes or more [26] caused by the long response times for the heater to heat up and indirectly increase the emitter temperature through the cathode tube. This indirect heating also causes larger energy consumption through ignition from the radiation from the heater sheath and conduction losses though the heater support and cathode tube.

Due to these drawbacks it would be beneficial to remove the mission critical heater sub-component and ignite the HC with a simplified ignition system. Removal of the heater component can allow greater reliability through design simplicity, as well as potential savings in mass, volume, power and ignition times.

1.4 HEATERLESS HOLLOW CATHODE CONCEPT

With a heaterless hollow cathode (HHC), the ignition and heating of the emitter is driven by a discharge between the keeper and the cathode body or with the keeper and emitter directly. As such the emitter is raised to the equilibrium thermionic temperatures by the discharge itself from ion bombardment heating, without requiring an additional ohmic heating component. This does require though an order of magnitude higher potential to initiate the discharge due to the lack of thermionic seed electrons. However, the direct heating of the emitter can establish thermionic emission quickly as only a fine layer of the emitter surface is required to reach thermionic temperatures for thermionic emission to begin. As mentioned, the conventional HCs can take over 15 minutes to be ignited, whereas heaterless ignition has been demonstrated within seconds [27].

Heaterless hollow cathode ignition undergoes three main phases to transition from dormant to nominal operation: breakdown, glow discharge, and arc discharge. The heaterless ignition mechanisms are shown in Figure 1.3. Firstly, propellant is injected into the cathode tube, raising the pressure between the cathode and keeper electrodes, with a few seed electrons naturally present. Secondly, a potential is applied between these electrodes, accelerating the seed electrons, causing a Townsend avalanche [28, 29], electrically breaking down the gas. Thirdly, with enough current limitation, by the power supply or from electrical resistance in the circuit, a glow discharge forms, where ions accelerate to the emitter resulting in the secondary emission sustained discharge and emitter heating from ion bombardment. Once the emitter reaches the required thermionic temperatures, >1100 °C, it begins to thermionically emit. Fourthly, with sufficient thermionic

emission a transition occurs to a thermionically sustained discharge, and the self-heating mechanism is again primarily through ion bombardment, though it is higher density and lower energy bombardment. The discharge electron production is from thermionic emission, and hence characteristic of an arc discharge. This is the final stage and hence the HHC is considered to be in nominal operation and can transfer the discharge to an anode as with a conventional HC. Initiation of one phase does not guarantee progression to the next phase(s) [27] such that breakdown or heating alone is not full ignition. When all three stages are complete the heaterless and conventional HCs operate with the same heating mechanism of ion bombardment.

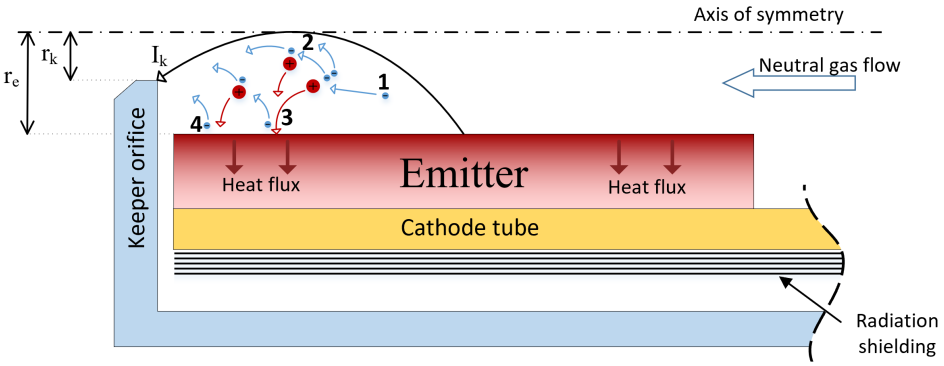

Figure 1.3: Schematic of heaterless hollow cathode ignition.

It is important that the heaterless ignition process is specifically defined, due to the heating mechanism differences with conventional ignition. Full heaterless ignition is the successful transition through all three stages from breakdown, glow discharge and arc discharge (nominal operation). It is important to note that full heaterless ignition does not require the whole HC device to have reached steady state temperatures, or even the whole emitter. Such that nominal operation can be achieved with as little as the top layers of the emitter (perhaps merely a few microns thick) reaching thermionic emission temperatures. After which, there can be small operational changes occurring over time while the steady state temperature is reached. The time for the HHC to reach thermionic temperatures from dormant is dependent on the discharge power, as conventional HCs are dependent on the heater power.

1.5 RESEARCH OBJECTIVES

It is known that conventional hollow cathodes can be *hard started* from cold by passing very high flow rates (>50 sccm) and applying very high voltages (>1 kV) to the keeper with a non-diffuse arc discharge, but such an approach can lead to unacceptable propellant usage and strong non-uniform erosion with thermal shock [27, 30], hence that approach has commonly been avoided. Thus, this research investigates heaterless ignition while attempting to overcome these challenges

associated with ignition from cold. For the technology to be viable for purpose, ignition must be demonstrated with nominal flow rates (<20 sccm) and moderate ignition voltages (<500 V), while maintaining comparable performance with that of conventional HCs. Furthermore, the development of high-powered hollow cathodes is of importance to meet the demand of increasingly powerful GIEs and HETs [31]. As such, this research systematically investigates the influencing parameters and governing mechanisms of heaterless ignition to enable the development of reliable high power (≥30 A) heaterless hollow cathodes.

The main objectives of the research are as follows:

- The development of a high power HHC system which enables ignition with nominal flow rates, and moderate ignition voltages, with the specific goal of adapting the ignition process to ensure diffusive discharge attachment to minimise the melting/erosion that rendered past HHCs inoperable [27].
- Developing and investigating the ignition power management, which allows for repeatable uniform diffusive attachment. This is to be produced with the aim of insuring only passive controls are required, as any additional complexity to the PPU offsets the benefits of heater supply removal.
- Investigating the minimum breakdown voltage to initiate HHC start up, to minimise impact on the PPU and on HHC erosion. As such the cathode-keeper separation, keeper orifice sizes, and pressure parameters influencing breakdown voltage is determined.
- Characterisation of the ignition heating and transition phases to enable understanding of the operational parameters which induce diffusive attachment. This will be achieved by investigation of the emitter thermal profile, VI characteristics, and optical analysis, in relation to the operational and design parameters.
- Determine the HHC nominal operation performance in relation to current state-of-the-art HCs, to assess the viability of this novel heaterless approach.

1.6 THESIS OVERVIEW

This first chapter introduced the general field of electron sources and that of modern in-space cathodes, describing the differences between conventional and heaterless ignition. This included the explanation of the motivation and objectives of this investigation into heaterless ignition.

Following this introductory chapter, Chapter 2 provides a critical review of heaterless ignition research conducted to date, with detailed comparison of HHC design types and performances reported. The enhancements and limitations of the systems presented are outlined.

Chapter 3 follows with the theoretical background for heaterless ignition, which is not in common with that of conventional in-space cathodes, thus requiring overview. Breakdown, glow discharge, and arc discharge theory are reviewed.

Chapter 4 provides a detailed description of the experimental apparatuses, including diagnostics used for investigating the novel HHC. Additionally, the operational procedures for HHC operation are detailed.

The methodology for the design of the novel high powered HHC, utilising the knowledge from the theoretical background and review of past HHC literature is described in Chapter 5.

The results of the HHC experimental proof of concept tests and investigations are presented and discussed in Chapter 6, including characterisation of ignition from breakdown to nominal operation, and demonstration of the HHC nominal operation up to 30 A with comparison to a conventional state-of-the-art HC.

Finally, in Chapter 7, this thesis is concluded with a summary of the main research findings and recommendations for future research to be conducted.

CHAPTER 2

REVIEW OF HEATERLESS HOLLOW CATHODES

2.1 INTRODUCTION

This chapter critically reviews the research and development that has been conducted on heaterless hollow cathodes to date, as well as reviewing other relevant research sources for HHC ignition. The operation of heaterless ignition of a conventional hollow cathode is well known [32], where an order of magnitude higher propellant is used, potentially through a propellant bypass, with a high ignition voltage (>0.5kV) [27]. This method can be used as a redundancy operation in case of heater failure [33], and is known as *hard starting* the cathode. The issue with this operational procedure is the resultant high erosion due to the high energy breakdown, as well as a large amount of propellant usage, and hence why it is only used as a last redundancy option and not considered feasible for standard operation.

Some preliminary investigations have been carried out on hollow cathodes adapted specifically for heaterless ignition by NASA in the 1980s [30], and Russia in the 1990s [34], though the breakdown at high potentials and consequent erosion and melting meant that the heaterless ignition research was not continued. This has changed in the last two decades as the increasing demand for longer life high power cathodes, in addition to missions that require fast ignition HCs, has caused a significant renewed interest in heaterless ignition. The field is currently thriving and being researched by multiple research groups internationally, including SITAEL [35], Rafael [36],

and Harbin [37]. In response to this increased interest, a recent (2016) research summary of the international heaterless efforts has been presented by Lev [38].

A critical review is now carried out on the HHCs designs including discussion on the main differences to that of conventional HCs. Also, the performance characteristics and failure mechanisms of HHCs are reviewed. Finally, a summary is given of the current development status of HHCs and specific areas for future research are identified.

2.2 COMPARISON OF HEATERLESS HOLLOW CATHODE DESIGNS

2.2.1 DESIGN VARIANTS

In reviewing heaterless hollow cathode literature, it is seen that several different HHC designs have been developed and tested. These HHC designs vary from very simplistically rugged cathodes with no heater or low work function emitters [30], to more complex heaterless cathodes with multiple low work function emitter electrodes [34]. The overall configurations of the different HHCs are shown in Table 2.1, with the design features discussed.

Table 2.1: Comparison of heaterless hollow cathode designs

Design type	Diagram of main electrode characteristics	Authors	Comments
Conventional hollow cathode	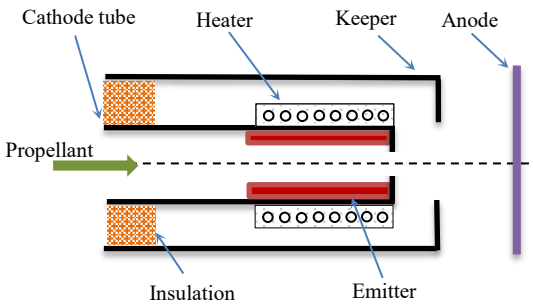	Goebel [39] †Schatz [27] †Albertoni [35]	This gives the generic overview of conventional hollow cathodes, as was also shown in Figure 1.1. This design is widely researched and commercially produced for spacecraft propulsion. This conventional design has been cold started by researchers, though requires a very high ignition potential and flow rates. †Heater not used
Heaterless with reduced keeper orifice	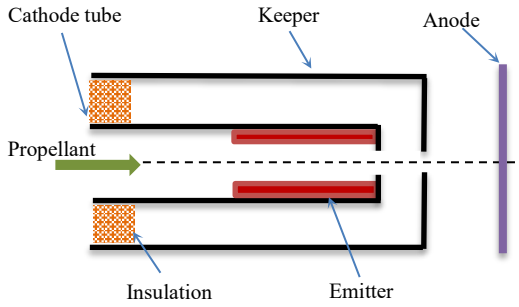	Ouyang [37]	This heaterless modification is very similar to that of the conventional HC, the main difference along with removal of the heater component, is a reduced keeper orifice to increase the pressure in the cathode-keeper region, thus increasing pd and lowering the operating voltage and flow rates required during ignition. This modification can potentially reduce electron extraction due to the reduced orifice, but this is the most common used feature of all the modifications for heaterless hollow cathodes tested.

Design type	Diagram of main electrode characteristics	Authors	Comments
Heaterless with reduced keeper orifice and open emitter	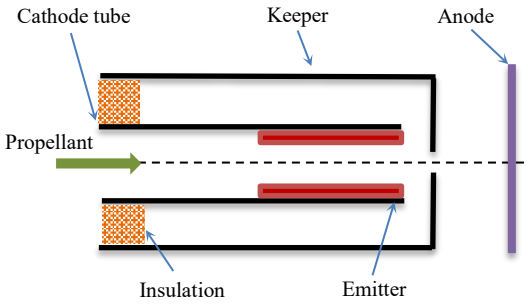	Lev [40] Loyan [41] †Fearn [42] ††Aston [30] ††Kaufman [43]	In this variant the cathode orifice is removed, such that the discharge occurs directly between the emitter/cathode and the keeper without an intermediary constrictive orifice, increasing the direct plasma heating of the emitter. This design has been found to suffer from high erosion and even melting, though that occurred when overpowered. This overall configuration appears most commonly in the literature, perhaps due to the simplicity of the design and the power supply requirements. Commonly cathode-keeper insulator failure is discussed with this design, feasibly due to conductive deposition. †Preheated emitter to > 600 °C, though below thermionic levels. †† No low work function emitter used, only a refractory metal tube
Semi-heaterless hollow cathode with internal electrode	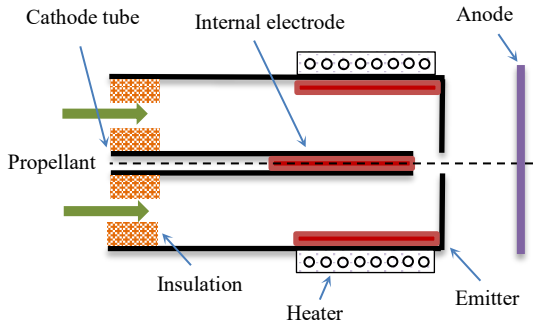	Fearn [42]	This design developed by Fearn, used an internal tungsten wire electrode and emitter preheated to > 600 °C with a heater. As such, Fearn's experiments were not heaterless, though it was well below the conventional starting temperature for a HC. As the emitter is formed of a wire, it makes the design very simple and robust, though the internal electrode suffered high erosion and it was found challenging to transfer the discharge to the anode.

Design type	Diagram of main electrode characteristics	Authors	Comments
Heaterless with reduced keeper orifice, open emitter and auxiliary electrode	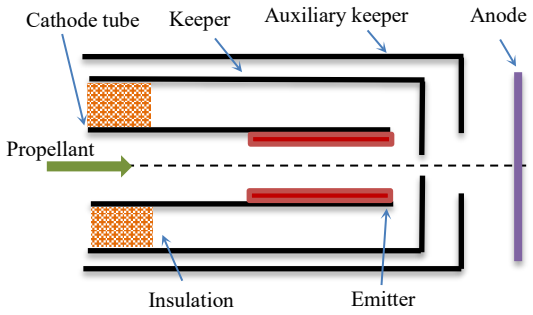	Schatz [27] †Arkhipov [34]	This design with an additional electrode has claimed to improve the ignition reliability. The Auxiliary electrode in effect provides the function of the keeper on a conventional HC, due to the orifice reduction of the keeper altering its conventional functionality. This design has the drawback of requiring an additional power supply, thus counteracting the benefit of heater supply removal. †The keeper orifice was made from porous tungsten saturated with activator salts of barium and potassium as with the cathode emitter, such that there were two low work function emitter electrodes.
Heaterless with reduced keeper orifice, covered emitter, and auxiliary electrode	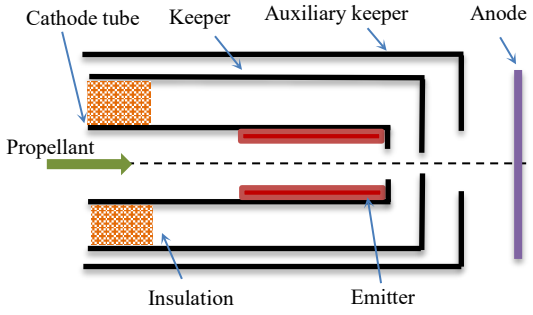	Schatz [27]	This is a similar variation to above, though Schatz's re-introduced the cathode orifice. This was not a flow restrictive orifice, instead the intention was to protect the emitter from the discharge initiation. This variation of Schatz's laboratory model ultimately proved futile in erosion reduction. Erosion still occurred along the emitter, resulting in the cathode orifice cracking and becoming fused to the emitter.

Note: (1) The electrode nomenclature in the literature is not consistent for multi-electrode designs, such that the inner most electrode is sometimes referred to as the 'internal electrode', followed by the cathode and keeper instead of the outer most electrode being referred to as the 'auxiliary electrode'. (2) The diagrams shown are simplified, not including the radiation shielding or supports, in order to clearly show the main electrode differences between models.

2.2.2 PROPELLANT MANAGEMENT

Conventional HCs have been tested for cold ignitions as a redundancy measure if the heater component fails. Such that no modifications to the design are pursued for the heaterless operation, and only changes in the ignition operation procedures are explored. The flow rates required to cold start conventional HCs are much higher, often over an order of magnitude higher than nominal operation, see Figure 2.1. As will be discussed in Section 3.2, the Paschen theory states that the breakdown is a function of the distance and pressure, thus to achieve breakdown on a conventional HC, higher flow rates are required if the distance remains the same. The relationship for increasing propellant to breakdown voltage is shown by Schatz in Figure 2.1 for a conventional cathode. Showing a very Paschen like curve, though with the Paschen minimum only being approached at over 50 sccm, which is an unacceptably high flow rate. Albertoni has recently developed a heaterless LaB_6 cathode [35], with a conventional design. This modern system was found to also require xenon flow rates up to 50 sccm during ignition and with breakdown voltages around 800V.

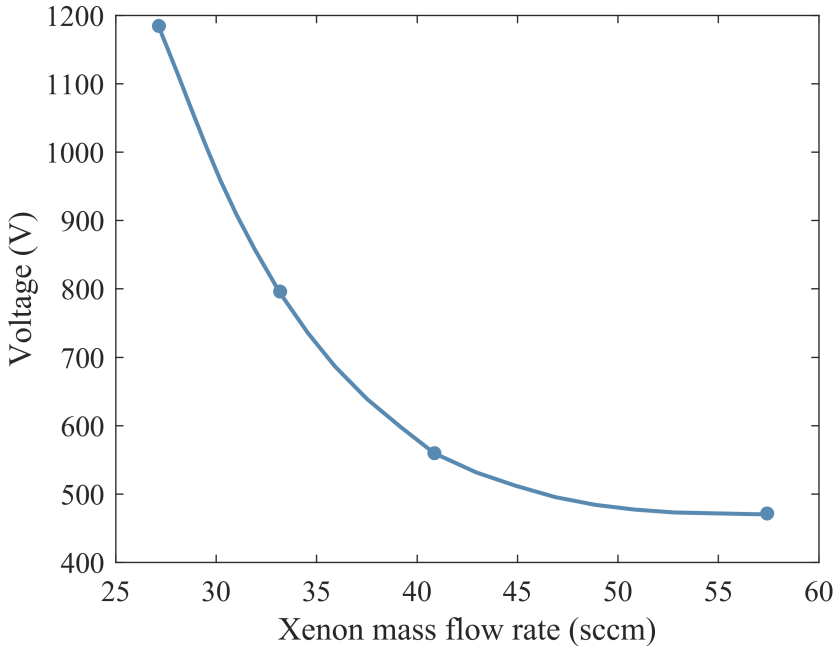

Figure 2.1: Breakdown against mass flow rate for a conventional HC [27]

To meet the pressure requirements through the operational parameters, either flow rate can be increased to a high steady state value [27] or the flow rate can be pulsed [34]. Both options require increased mass on the spacecraft, from the extra propellant and valves required. There are several options for propellant pulsing, such as; an unmeasured bypass valve which can be opened momentarily, a large mass flow rate controller, or through a standard mass flowrate controller

with an additional downstream valve, which closes to build up a propellant reservoir and then opens to flood the HC momentarily for ignition, as shown in Figure 2.2. All options come with an increased risk of system failure, which is due to requiring additional valves or mass flowrate controllers that can operate at magnitudes higher flow rates. These valves can potentially fail at max output, causing immensely high propellant loss. Valve failure is a concern in propulsion systems, with some EP systems opting for flow splitters between the thruster and cathodes, to minimise the number of valves, but as a result these systems do not have individual control over HC flow output. Due to these difficulties, most HHC researchers have opted for reduction in the keeper orifice to increase the pressure in the cathode-keeper gap, thus allowing breakdown at standard operating flow rates.

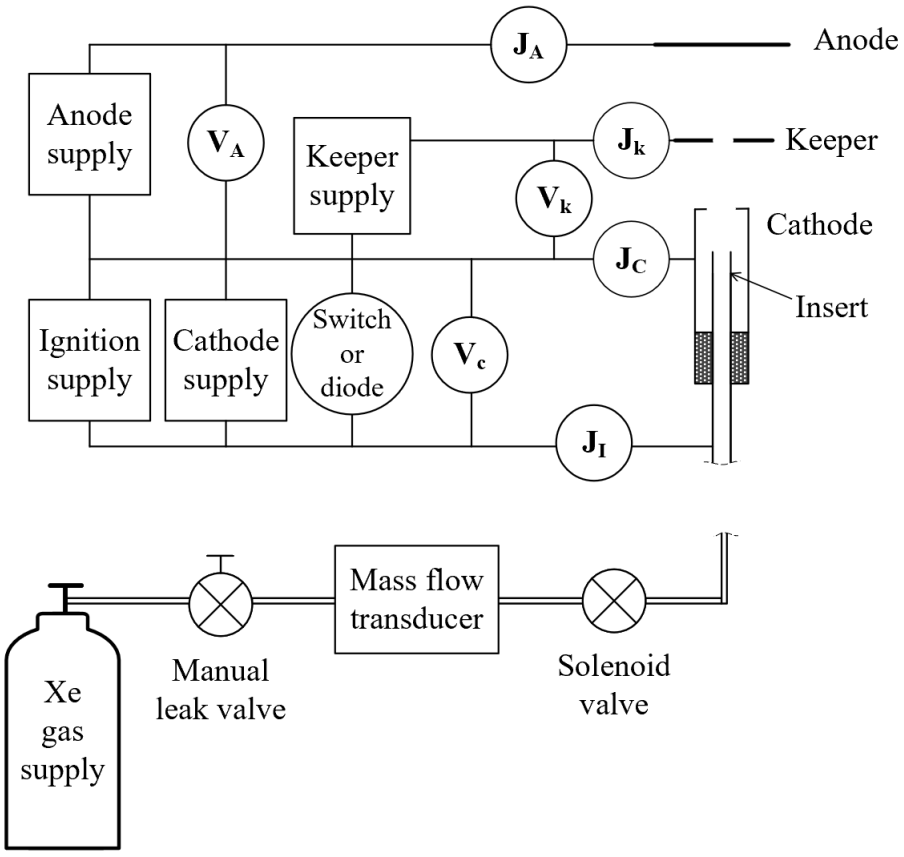

Figure 2.2: Schatz's HHC propellant and electrical set-up [27]

2.2.3 GEOMETRIC INFLUENCE ON THE INTERNAL PRESSURE

The geometry of the HHC influences both the pressure and electrostatic fields, which influence the ignition characteristics and thus it is a very important parameter in HHC designing. The cathode orifice determines the pressure within the emitter region; typically with conventional HCs the flow is choked at the cathode orifice, and during nominal operation the emitter can be heated

by orifice heating as well as by direct ion bombardment [44]. Whereas, as mentioned in the section before, with heaterless systems the flow is most often choked at the keeper orifice, to lower the breakdown voltage by raising pd toward $(pd)_{min}$ [27]. HHC operational pressures between the cathode and keeper with the reduced keeper orifices are reported to be between 0.1-50 mbar [30, 36], this large range is due to the difference in keeper orifice sizes tested. This is commonly significantly less in conventional cathodes, that operate with transitional to free molecular flow in that region [45]. Though this pressure is similar to that of inside the cathode tube of conventional hollow cathodes [46]. The reducing of the keeper orifice to essentially become the cathode orifice for most heaterless versions, may have a consequence of removing the keeper function of increased ignition stability, hence why some authors [47] have found improved stability from implementing auxiliary electrodes, as shown in Table 2.1. Though this approach can lead to further design and electrical complexities that takes away from the simplification benefit of heaterless ignition.

The size of the conventional cathode orifice determines the heating mechanism of the emitter in steady state operation due to the pressure and electrostatic profile [44]. If there is a large cathode orifice, heating is predominantly through direct ion bombardment while if it is a fairly constrictive orifice, heating occurs conductively through the orifice heating and by direct ion and electron bombardment, and finally, with a very small orifice, the heating occurs predominately through orifice heating [44]. As can be seen in Figure 2.3, the region of high plasma density across the emitter, is strongly influenced by the constrictive orifice size, with a smaller orifice causing contraction of the discharge attachment close to the orifice. This can have implications for heaterless ignition, as the keeper orifice is typically reduced which could lead to concentration of the plasma attachment toward the emitter tip. Though the influence of the plasma density on the orifice being separated and further downstream from the emitter in HHCs has not been investigated in the literature.

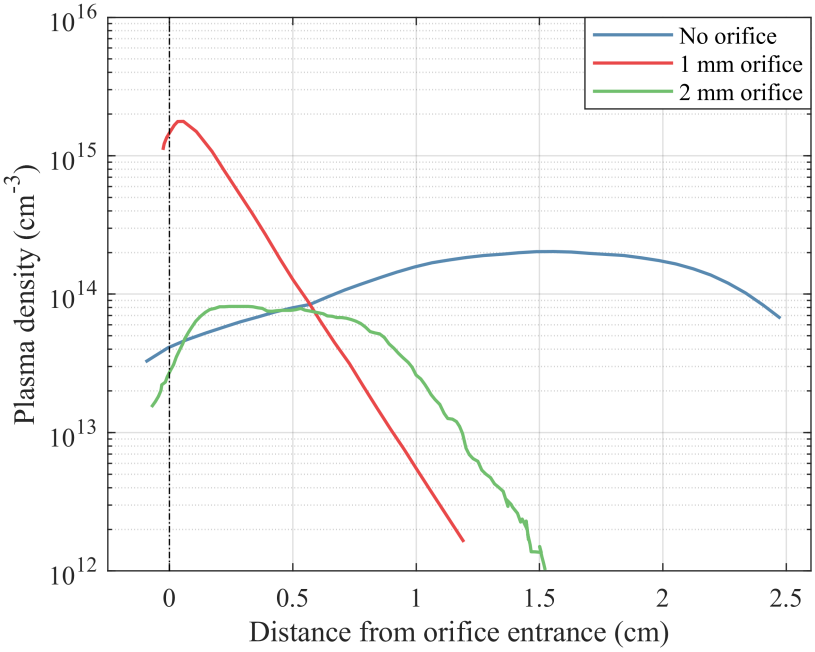

Figure 2.3: Plasma density profile along a 2.5 cm long emitter for a conventional HC with varying cathode orifice sizes [44]

A non-constrictive cathode orifice attached to the emitter end, which has the same ID as the emitter, can potentially aid in protecting the emitter from sputtering during and post ignition. Though for HHCs during the heating phase the emitter will be partially heated through this emitter cover indirectly. Thus, without an emitter cover the heating is done directly to the emitter with only the emitter top layer requiring heating to thermionic temperatures for thermionic emission to occur. This could allow transfer to the arc discharge rapidly. Though without the cover, this means the erosion occurs directly to the emitter. Schatz [27] found such covers empirically ineffective to stop the emitter degradation, with melting and fusing of the cover to the emitter occurring.

2.2.4 GEOMETRIC INFLUENCE ON THE ELECTROSTATICS

The geometry of the hollow cathode has influence in terms of the electrostatics, and has been extensively studied by David Fearn [42, 48-51] for conventional cathodes. The main function of the keeper electrode is to initiate and help maintain a cathode discharge, as well as protecting the cathode from sputtering. It has been found that the keeper-cathode separation is influential to the ignition potentials in conventional HCs [48], due to the Paschen breakdown. This has additionally been tested for HHCs [27], where the Paschen law more accurately applies due to the lack of thermionic emission at breakdown. Empirical studies on HHCs have been conducted by NASA [27, 30] into the breakdown voltage influence by a range of geometric parameters such as cathode-keeper separation and keeper ID which have indicated that the pressure is the main influencing

parameter rather than the electrostatic changes caused. In general, increasing the keeper-cathode separation reduces the flow rate at which the minimum breakdown voltage occurs due to the pd product increasing, if operating on the left of the Paschen curve and with the converse occurring if operating to the right of the Paschen curve. Though it must be considered that increasing the keeper-cathode separation reduces the electron extraction efficiency, in terms of discharge current extracted to discharge power used, due to the increased electron wall losses.

Auxiliary electrodes have been installed to aid the ignition process of HHCs, both internally [49] and externally [34]. Fearn showed that the internal electrodes benefit from the high internal pressure inside the cathode tube, though once the discharge is initiated, transferring to a keeper discharge is challenging due to the keeper potential opposed by that of the positive internal electrode. Applying a negative voltage to the internal electrode allowed for rapid transfer, though required higher potentials and suffered severe erosion of the internal electrode - construction of a durable internal electrode is challenging due to the small dimensions and harsh operational environment. Arkhipov reported that external electrodes have improved start-up reliability of the HHC [34], by aiding in maintaining the discharge once the arc discharge is formed. As mentioned, the disadvantage is the additional power supplies, size increase and design complexity. In Arkhipov's HHC design [34] the keeper was constructed from porous tungsten saturated with activator salts of barium and potassium, as with the cathode emitter, although the details of the reasoning is not given, the intention is presumably for the keeper to provide some thermionic emission to the anode, suggestive of relatively higher keeper temperatures than with conventional cathodes. Typically, keeper electrode material selection is based on sputter yields, due to the ion bombardment erosion that is inflicted upon the keeper in operation and can be a life limiting factor [23].

2.2.5 POWER MANAGEMENT

The electrical set-up of a heaterless hollow cathode does not require a heater supply, as can be seen in Schatz's electrical circuit, shown in Figure 2.2. An HHC can be *hard started* or alternately *soft started* from room temperature to thermionic emission conditions. Hard starts can be defined as a heaterless ignition in which there is no additional current or discharge control in respect to that of conventional cathodes. Whereas a soft start utilises additional current and/or discharge control during the heaterless ignition to attempt to soften the start process and reduce erosion.

As mentioned it can be relatively simplistic to hard start a HHC when sustained high voltages are applied with adequate pressures, though this results in high erosion [27]. A soft start with systematic current control requires more sophisticated electrical design but can reduce the erosion through ignition. Both types of heaterless starts entail attempting to produce a nominal thermionic

discharge, though a hard start does not require control of the power applied through the ignition process. A soft start can control the power consumption through the ignition process to reduce the erosion caused through the formation of the discharge. The breakdown and glow discharge stages are considered to have the highest erosion rates due to the higher potentials involved, thus attempts have been made to reduce the breakdown voltage and to limit the time spent in glow discharge [27]. This has even led authors to transfer directly to an arc discharge from breakdown [40], though this can cause discharge contraction. Throughout the ignition, high current density cathode spots tend to form [41] but current control has been found to help mitigate this issue [36]. So due to these issues the way in which the soft start is conducted is of great importance. Unfortunately there is not a significant amount of detail in the literature on the current controls attempted, with some authors merely referring to the use of an *ignition box* [36], though several soft start attempts have proven unsuccessful [27, 52], with melting still occurring.

The breakdown stage has been reported to occur within the micro to millisecond timeframe, with the glow discharge, if occurring, reported in the centisecond [36] to the tens second [30, 34] timeframe, and the arc discharge is the nominal operation and thus lasts effectively continually. In order to control the power supplied within such timeframes brings its own challenges to the keeper-cathode supplies; multiple power supplies can be used, as shown in Figure 2.2, or ballast resistors (100-300 Ω) to stabilise the momentary current peaks in breakdown [27, 37, 53]. A 100 Ω ballast resistor has even been implemented by Lev for current control of the anode discharge post ignition [52]. The challenge is that introducing ballast resistance, which appears the most successful control applied, causes large power losses for the system. For smaller HHCs this may be acceptable, but for larger, high current cathodes, power management is crucial.

Overall in the literature it appears most heaterless failures from melting and high erosion are linked to the energy supplied through the ignition process not being sufficiently controlled. As such energy control through ignition is of crucial importance for reliable HHC operation. Schatz [27] states the stability of the discharge is dependent on the circuit such that:

$$R - R_p > 0 \tag{2.1}$$

where R_p is the plasma impedance and R is the circuit impedance at the intersection points of the load line (see Figure 3.3 – Section 3.3.1). Thus, proper characterisation of the plasma impedance should be conducted in order to ensure adequate circuit impedance to stabilise the discharge. Though due to the issues of ballast resistance causing unacceptable power losses for high current HHC ignition, alternative stabilisation methods should be investigated that provide adequate

impedance for the breakdown and heating phases while passively minimising power consumption through ignition.

2.3 COMPARISON OF HHC SYSTEM PERFORMANCES

2.3.1 PERFORMANCE CHARACTERISTICS

The first in-space hollow cathode designed for dedicated heaterless ignition was by Aston in 1984 [30]. Aston's simplified HHC did not use a low work function emitter, but instead used a simple refractory tantalum tube. A potential difference was applied between this tube and a molybdenum keeper, producing a glow discharge that rapidly transitioned to an arc discharge. The whole process for start-up occurs within ~1 second. The devise operated stably at ~100 watts once started, with breakdown voltages below 500 V achieved, at flows rates from 6-14 sccm with emission current up to 35 amps attempted. This research demonstrated the initial start-up characteristics, as well as impressive production of high current densities, estimated up to 25 A/cm^2. However, the design suffered from strong erosion, due to localised overheating, possibly caused by discharge contraction with the rapid transfer to arc discharge, within ~1 second, thus not sufficiently heating the whole tantalum tube. After several hours of operation, both tantalum tubes tested were completely crystallised as well as partially melted, thus localised temperatures over 3000 °C were reached. Additionally, the cathode orifice plate underwent noticeable scalloping. Hwang-Jin [54] in 1989 attempted further testing of Aston's design, though also found the system performance too erratic conditions for electron emission purposes and again the system failed due to overheating and arcing damage.

Aston's design was further developed by Schatz [27], utilising a sintered porous tungsten low function emitter, which required a lower temperature to provide a given thermionic current than Aston's tantalum tube. In addition, a tantalum cover was placed over the emitter to minimise erosion through ignition, however it was found to become fused with the emitter with cracking at the weld joints after a mere 10 hours of operation. Despite the erosion and damage problems faced by this heaterless cathode design it successfully ignited 96.6% of the time, with over 3500 ignition cycles. Schatz found that breakdown did not always transition into a glow discharge or with a further transition into arc discharge. Half the failed starts were thought to be due to the low keeper potentials through glow discharge, thus the thermionic temperatures required were not met. This shows the importance of the power supply load line in relation to the discharge profile, to provide adequate input power and stabilisation to transition fully and stably to a thermionic discharge, and thus should be investigated.

Work has been conducted at EDB “Fakel” by Arkhipov in 1990’s, in which 6 HHC laboratory models have been developed [34, 47], with operation ranging from 1.5-6 A, with initiation voltages of 400-500 V. Similar to NASA [27], the design utilises an auxiliary keeper, although as previously mentioned, with both the cathode and keeper manufactured from low work function material. Ignition was achieved within one second and flow rates were tested from ~0.1-10 sccm. To determine erosion, the mass of the electrodes was measured systematically, demonstrating high erosion rates with flow rates below 4 sccm, and a levelling off erosion rate when increasing above 5 sccm, with a reduction in erosion seen between 4-5 sccm. Issues arose from the emitter-keeper insulation that caused the electrodes to short and thus result in re-ignition failure. It was found that the insulation resistance reduced during successive start-ups from the re-heating, as well as from deposition of a conductive material on the insulator connecting the emitter-keeper electrodes.

National Aerospace University "KhAI" led by Loyan have designed a range of HHC’s [55] and conducted several studies [41, 56-58]. A range of low power devices from 0.2 A [59, 60] have been tested, with erosion rates estimated through spectroscopic tests in which erosion is taken to be proportional to the emission intensity. This work indicated that there is an optimum mid-pressure point to achieve minimum barium erosion, in line with the Fakel findings [34]. In the HHC tests a backfilled bell jar set-up is utilised to simulate similar conditions to that of nominal operation. The group has also claimed to have produced high powered (15-55 A) BaO-W HHCs [61, 62] which ignite at voltages of ~700 V, and operate at ~9 sccm (Xe). Though there is insufficient information provided on the performance to critically assess these systems, and the group’s research into HHC systems has appeared to have ceased in the last decade.

More recent work has been conducted in Israel [36, 52, 63], led by Lev, developing a low power (0.5-1.5 A) HHC, with ignition voltages of <500 V and controlled management of the power input through ignition. Lev’s first HHC system [52] achieved 100 hours of operation, though the design was thermally unstable and the emitter end melted to the point of sealing the cathode tube. An updated model has demonstrated over 1500 hours of operation [40], although during the test an apparent experimental accident in which an inrush of air into the system ‘plugged’ the keeper orifice, leading to a keeper failure and its replacement. Due to the reduction in the keeper orifice size, it could be susceptible to higher erosion, from increased plasma bombardment, though Lev reports that no change in the keeper’s dimensions could be seen after the 1500 hour test. Figure 2.4 and Figure 2.5 shows the discharge performance characteristics for this low power HHC. The keeper floating voltage decreases, and stability increases with increased discharge current and increasing flow rate. The anode voltage can be seen to be 50 V at 0.3 mg/s (Xe), which is more than double that of conventional hollow cathodes, which is around 20 V for a cathode of that size.

It is possible that this is due to the reduced size of the keeper orifice blocking the electron trajectory to the anode, such that a higher voltage is required to overcome the increased wall losses. Additionally Lev implements a 100 Ω ballast resistor for anode stability [52].

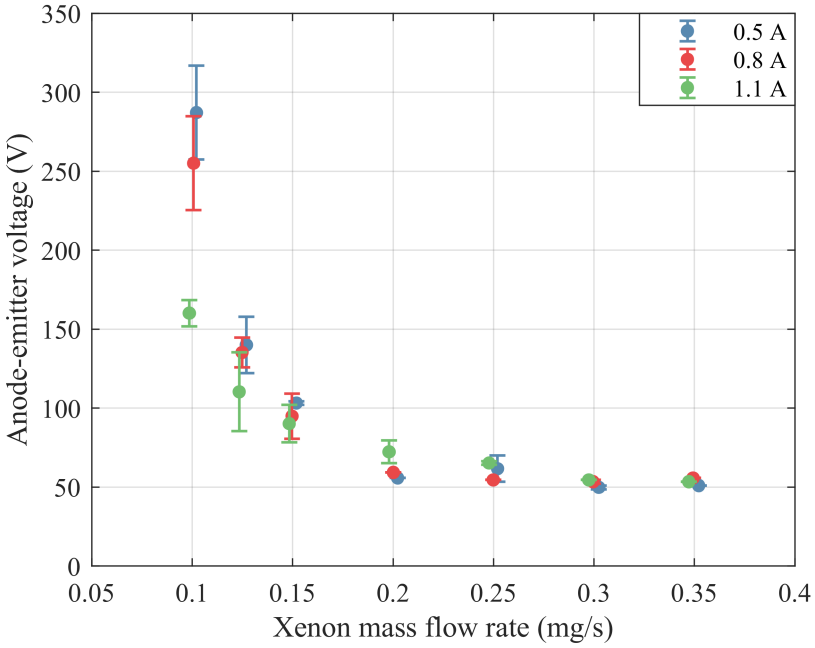

Figure 2.4: Anode-emitter voltage in respect to mass flow rate, for Lev's low power HHC at various discharge currents [40]

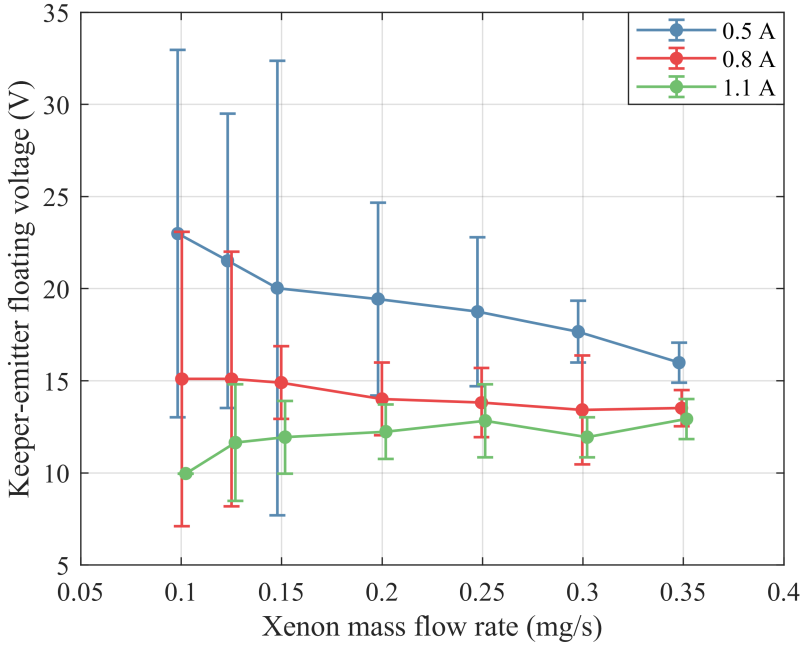

Figure 2.5: Keeper-emitter floating voltage in respect to mass flow rate, for Lev's low power HHC at various discharge currents [40]

SITAEL (formerly ALTA) have also recently designed a low power (0.5 - 3 A) and mid power (15 A) LaB_6 HHC [35, 64], with 100 hours of operation and 100 heaterless starts on the mid power variant and 50 of each on the low power variant. Most testing focused on nominal power operation. The power requirements were found to be higher than anticipated. At 2 A operation with a ~6 sccm xenon flow rate, power consumption is 30 W, which requires from ~10-25 % of the power of the intended application, a 100-300 W HET, though the larger cathode faired more favourably for its power class. Due to the conventional nature of their designs, extremely high flow rates were required for ignition, up to 50 sccm, with 800 V. Visual erosion analysis found deposition of graphite on both the emitter and orifice plate, though the emitting region of the emitter was relatively graphite free. Once ignited the performance of the larger HHC was reasonably comparable to conventional hollow cathodes, with ~20 V to the anode at a 15 A discharge current. This again is expected due to the conventional design, such that after the cold ignition, operation and design of this cathode is the same as conventional HCs.

2.3.2 HHC DEVELOPMENT

It is clear from the HHC performances achieved that further development on the design reliability is needed prior to space qualification, although Lev's low power HHC is currently the most space ready, with a lifetime operation of >1500 hours demonstrated. In comparison, conventional deep space cathodes such as the NASA NSTAR and NEXT cathodes, have undergone lifetime testing of over 30,000 and 50,000 hours respectively [65, 66]. The NEXT test was voluntarily terminated after nearly 6-years, thus with longer operation potentially possible. Though the lifetime and cycling required is dependent on the mission, with deep space missions typically setting the highest lifetime requirements.

The fact that melting often occurs [27, 52] with the HHCs shows that the energy input is not sufficiently controlled and/or discharge contraction is not being prevented. Thus, for the HHCs to be fit for purpose, further development of controlling the discharge attachment and power input through ignition is required. Also, the high anode voltage required from some of the smaller HHCs may be caused by poor electron extraction efficiency which appears to be a result of the keeper orifice reduction. As such the keeper orifice influence and current extraction should be investigated. Finally, it would be prudent for the overall research development efforts to be re-focused onto ignition cycling, rather than nominal duration testing, as most HHC modifications in respect to conventional HCs are for influencing the ignition. Hence testing should first determine the reliability and failure modes of sustained HHC re-ignitions.

Table 2.2: Comparison of heaterless hollow cathode performances

Author Year References	Breakdown voltage (V)	Heating stage power (W)	Discharge current (A)	Ignition time (s)	Lifetime (hrs) and number of cycles	Emitter type	Emitter diameter (mm)	Cathode keeper separation (mm)	Operational flow rate and pressure	Comments
Fearn, 1973 [49]	300	60	2	10	-	Niobium/ tantalum	0.2-3.5	2	0.5-6 sccm (Hg vapor)	Semi-heaterless testing as emitter is initially heated to >600 °C. Additional internal electrodes were used.
Aston, 1984 [30]	~350	550*	5-35	2	45 hours	Tantalum	2.8 & 3.6	-	2-15 sccm (Xe, Ar, N2, He) 0.1-6 mbar	These tests did not use a low work function emitter. Post-ignition power was 100 W.
Schatz, 1985 [27]	~350-500	50-210	1-15	5-10	3430 cycles	Impregnated tungsten	1.19-3.81	0.76-6.35	1-60 sccm (Xe)	This cathode was originally designed for 1 A operation but was tested to 15 A. V_b of 500 V is for 60 sccm with the conventional HC design, and V_b of ~300 V is for the dedicated HHC design with 3 sccm used.

Author Year References	Breakdown voltage (V)	Heating stage power (W)	Discharge current (A)	Ignition time (s)	Lifetime (hrs) and number of cycles	Emitter type	Emitter diameter (mm)	Cathode keeper separation (mm)	Operational flow rate and pressure	Comments
Arkhipov, 1994 [67]	400-500	35.1	1.5-6	0.2	1980 hot and 20 cold cycles	Barium and potassium impregnated tungsten	-	-	0-8.14 sccm (Xe) 20-25 mbar	
Loyan, 2000-13[41, 55, 59]	350-550	24	0.2-5	<1	500 hours	Impregnated tungsten	-	-	0.3-0.9 sccm (Xe)	
Kaufman 2015 [43]	-	-	1-5	-	1726 hours	Tantalum	2	-	1 sccm (Xe)	These tests did not use a low work function emitter and were tested with and without a heat shield.
Albertoni 2013 [35]	-	-	0.5-3	-	50 hours and 100 cycles	Lanthanum hexaboride	3	2	0.8-50 sccm (Xe)	The mass flow rate was at 50 sccm for ignition, then reduced to 0.8 sccm within 3 minutes.
Pedrini 2015 [64]	800	-	5-18	<120	300 hours and 100 cycles	Lanthanum hexaboride	3.6	2	10-50 sccm (Xe)	The mass flow rate was at 50 sccm for ignition, then reduced to 10 sccm within 2 minutes.
Ouyang 2015 [37]	300-600	25	1-5	150-220	-	Lanthanum hexaboride	-	-	1-9 sccm (Xe)	
Lev 2015-16 [40, 52]	400-1000	6-13	0.5-1.1	-	1500 hours	Barium impregnated tungsten	-	-	1-3.5 sccm (Xe)	

2.4 SUMMARY OF LITERATURE REVIEW

The heaterless hollow cathode ignition research field is still in its infancy: although the first prototypes were tested in the 1980's, in the following decades international research was conducted relatively independently and sporadically. However, this situation has recently seen change, particularly during the last 10 years. Currently, the research field is thriving and enjoying its highest level of activity ever with multiple research groups recently entering the field, including SITAEL, Rafael, Harbin and UoS. Successful prototypes have been developed, with 1500 hours of operation achieved [40]. This development is starting to establish the viability of the technology. Predominantly work has been focused on the development of prototype HHCs with few studies on developing the understanding of the ignition process, and erosion mechanisms. The key gaps in the knowledge identified from this literature review and addressed in this research are outlined below:

- Several adaptions to the flow system have been made to temporarily use very high flow rates to enable heaterless ignition of conventional HCs, though such an approach adds greater system complexity as well as mission risk. Thus, heaterless ignition should focus on utilising propellant systems in common with conventional HCs as the negative impacts of high flow rate ignition are too severe for the intended application.
- HHC designs that increase the cathode-keeper pressure by keeper orifice reduction allow for reasonable breakdown voltages (<0.5 kV) and mass flow rates (<20 sccm). However, it is imperative that further investigation is conducted on the negative side-effects of this design change, namely the impact on the electron extraction efficiency and keeper lifetime.
- Auxiliary electrodes may improve ignition reliability, though the design has a key drawback of requiring an additional power supply and adding greater complexity, thus counteracting the benefits of heater supply removal.
- Heaterless hollow cathodes commonly suffer high erosion and even melting due to the high voltage cold start. Thus, HHCs require higher current limiting control than that of conventional cathodes, this is due to the lack of thermionic emission with heaterless ignition. Additionally, effort should be focused on controlling the current attachment through ignition so that the emitter is uniformly heated, due to the localised melting often reported [27, 52].
- Development should focus on a simple HHC electrical design, that minimises waste power, as currently multiple supplies and/or ballast resistance have been used for attempted soft starts, which is not suitable for space applications.

- Finally, emphasis should be placed on developing the understanding of the HHC design influences on the ignition process, as well as the electrical design influences.

CHAPTER 3

HEATERLESS IGNITION PHYSICS

3.1 INTRODUCTION

Heaterless hollow cathode ignition comprises of three main phases: breakdown, glow discharge, and arc discharge, although the glow discharge phase can be directly surpassed depending on the HHC electrical setup. Each phase has separate discharge mechanisms that govern the characteristics of that phase. As such, this chapter reviews the applicable background theory for each ignition phase.

First, it is worth mentioning that the fundamental theory of classical gaseous discharge ignition has been well established for decades [28, 32, 68-70], and additionally there are multiple studies that have developed the understanding of conventional hollow cathode ignition [46, 49, 51, 54, 71]. Nevertheless, as discussed in the literature review there is scant research on the understanding of the fundamental heaterless hollow cathode ignition theory. This is due to HHC ignition theory residing in between the two knowledge pools of classical gaseous discharge ignition and conventional in-space HC ignition. This is since the HHC combines, the unconventional materials and relatively complex geometries that define a modern in-space hollow cathode with the heaterless ignition process. As such, HHCs ignition mechanisms are distinctively different to that of conventional HC ignition, and there is minimal literature investigating the actual ignition process, with the main referenced electric propulsion textbook [46] not specifically discussing the topic. While the overall HHC ignition *V-I* profile has been characterised for a given low power HHC [36], deeper understanding of the influences relating to the heaterless ignition phases is critical for increasing the reliability and stability of the heaterless ignitions. Such understanding can support the development of the technology to a mature flight ready state.

Thus, this chapter aims to cover the theoretical considerations of HHC ignition. Due to the gaps in the knowledge discussed, this is achieved through careful consideration of the applicability of established classical theories to the relatively complex geometries and exotic materials that make up modern in-space HHCs.

This chapter follows the HHC ignition sequence, beginning with the gas breakdown theory followed by the glow discharge and arc discharge theory. In addition, this chapter covers two key plasma physics phenomena occurring in the ignition discharges: cathodic spots and the secondary electron emission. The theory in each section most closely follows that of Lieberman [28], Raizer [68] and Jensen [13], with additional relevant sources referenced in the text as appropriate.

3.2 BREAKDOWN THEORY

3.2.1 TOWNSEND AVALANCHE

Electrical breakdown is the transformation of a nonconductive medium into a conductive medium via ionisation due to the onset of a potential difference between electrodes. The breakdown process starts with seed electrons, which form coincidentally, by for instance photoionization or other means. These seed electrons are then accelerated due to an electric field, gaining energy in the process. The electrons collide with the neutral atoms or molecules, and if the energy of the striking electron is greater than that of the ionization energy, then an electron is removed from the atom, most commonly the valence electron which is the most loosely bonded electron [28]. This newly freed electron and the original seed electron gain kinetic energy in the electric field, eventually enough for both electrons to cause further ionization incidents, this process repeats, multiplying the number of electrons, such that there is a cascading ionization avalanche. This was first described by Townsend in 1910 [28, 29] and hence referred to as a *Townsend avalanche*.

Electrical breakdown will occur only when the electric field strength reaches a critical value, which is referred to as the breakdown voltage - this is a function of the dielectric medium and electrode conditions. When this breakdown voltage is reached there is a sudden rise in ionisation incidents and hence current flow increases. The sensitivity of this tipping point or breakdown voltage is due to the cascading ionization effect mentioned. Prior to achieving that threshold, the electron energy losses in the system encumbers the electrons from achieving the ionisation energy required, which for instance is 12.13 eV for the xenon single-ionization energy [72]. The main electron losses are from excitation of atoms and molecules, molecular rotation/vibration, and to collisions with the walls. Recombination events are very unlikely in the early formation of an avalanche, as electron-neutral collisions are far more probable than that of ion-electron collisions due to the high proportion of neutrals initially, thus recombination has an insignificant influence

on the breakdown voltage. However, as the avalanche progresses, numerous electrons are formed, and as recombination is proportional to the electron density squared, the proportion of the overall electron energy losses from recombination increases dramatically. Thus recombination can influence the final level of ionisation in the breakdown [68].

3.2.2 PASCHEN'S LAW

Prior to that of Townsend's theory, in the 1880s Paschen [28, 73] conducted a series of breakdown experiments, applying a potential between two parallel plate electrodes with varying electrode separations, gas species, and electrode material. He discovered that breakdown voltage, V_b, was dependent on the cathode secondary emission coefficient, γ_{se}, gas properties, A_g and B_g, and most importantly the product of pressure, p, and electrode separation, d. The breakdown voltage can be expressed as [28, 68]:

$$V_B = \frac{B_g pd}{ln(A_g pd) - ln\left[ln\left(1 + \frac{1}{\gamma_{se}}\right)\right]} \tag{3.1}$$

where A_g and B_g are gas properties determined experimentally with units $cm^{-1}Torr^{-1}$ and $Vcm^{-1}Torr^{-1}$ respectively, which are constants over a reasonable range of the electric field/pressure, E/p. This equation reveals the clear relationship of the breakdown voltage to the product of the pressure and electrode separation, such that $V_B = f(pd)$. When plotting Equation 3.1 with V_B against pd, a curve is produced with the minimum breakdown voltage V_{min} at some intermediary value $pd = (pd)_{min}$, this is referred to as a *Paschen curve*. The limiting value of pd below which breakdown is not theoretically possible is given by $pd = A_g^{-1} ln\left(1 + \frac{1}{\gamma_{se}}\right)$. There is rapid increase in V_B below the $(pd)_{min}$, which is influenced by the gas and cathode properties, and at higher values of pd, beyond $(pd)_{min}$ increases almost linearly with pd.

Experimentally determined Paschen curves for various gas species are shown in Figure 3.1. The Paschen curve minimum can be seen to be typically in the region of 1 Torr $*$ cm, though dependent on the gas species.

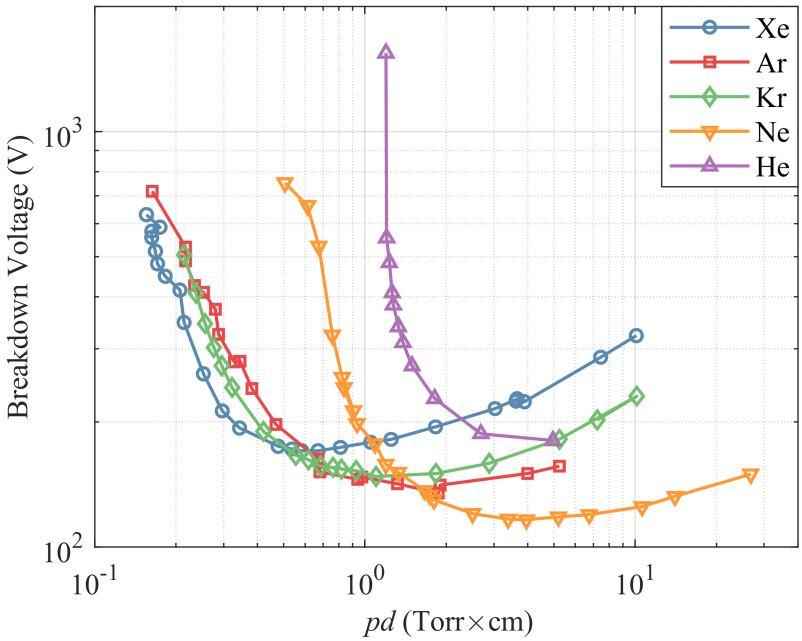

Figure 3.1: Paschen curves for parallel electrodes with various gases at 20 °C [74]

The Paschen curve characteristics of steep voltage increase on the left of $(pd)_{min}$, and gradual increases on the right of $(pd)_{min}$, are due to the previously mentioned Townsend avalanche mechanisms. First, let us assess the left of the Paschen minimum. For a reasonable electrode distance at very low pressures, the free mean path (λ), which is inversely proportional to the pressure is very large, such that the distance between ionisation incidents is relatively long in comparison to the electrode separation. Therefore, even though the electrons accelerate to the ionisation energies required, there is insufficient number of successive ionisation incidents to form an avalanche necessary to electrically breakdown the gap, thus voltage rises to ensure the successive ionisation incidents are sufficient to form the avalanche. Similarly, for very short electrode distances with reasonable pressure, the distance is too short for sufficient cascading ionisations to take place to breakdown the gap, hence the voltage rises left of the Paschen curve. With extreme decreases in pd to the point where little to no avalanche takes place, the Paschen breakdown cannot occur. Though breakdown is possible at very high potentials, in these conditions field emission mechanisms better represent the physical process, and can be predicted by the Fowler-Nordheim equation, the interested reader can refer to [28] and [68] for a full description of that process.

Now to assess the right of the Paschen minimum. If there is high pressure for a reasonable distance, the mean free path is small, and the distance between collisions can become too small for the electrons to gain the ionisation energy required due to the losses from inelastic collisions. Hence forming an avalanche is difficult, and so voltage must be increased. For a large distance

with reasonable pressure, the voltage must increase to maintain the electric field strength at a given point in the gap to again achieve the ionisation energies. Hence the voltage increases right of the curve, though this validity stops at high pressures, roughly at or above atmospheric with large gaps (>1 cm). Such conditions are represented by spark discharge mechanisms, due to the space charge effects influencing the avalanche. The interested reader may again refer to [28] and [68] for a detailed description of this process. From the descriptive arguments of the Paschen breakdown, it is clear that there is an optimum product of the distance $pd = (pd)_{min}$, where $V_B = V_{B_{min}}$ is an intermediary value between the previously mentioned Paschen limits.

It is worth evaluating the influence of the gas and electrode properties on the breakdown voltage. Each gas species has a given molecular diameter, which determines the mean free path of the collisions. The Paschen curve moves to the left for a larger atom diameter, due to the mean free path decreasing. In addition, each gas species has an ionisation energy, this parameter has a large effect on determining the breakdown voltage, as a higher ionisation energy requires the electrons to gain higher energy to achieve ionisation. The secondary electron coefficient, γ_{se}, is the mean number of electrons emitted per ion collision with the surface of the cathode. The greater the number of electrons emitted, the easier the avalanche formation becomes. Thus, a material with a high secondary electron coefficient reduces the $V_{B_{min}}$. However, γ_{se} is also strongly dependent on the surface conditions, so gathering this information accurately for materials can be challenging.

3.2.3 PASCHEN'S APPLICABILITY

Paschen's theory provides a reasonable description of the breakdown behaviour between parallel plates for gas discharges. However, when applying Paschen's law to that of heaterless ignition, the assumptions associated with the law have to be considered. Electron production is considered to be primarily caused through ionisation for Paschen breakdown and this can be reasonably assumed for HHC ignition as there is no thermionic emission prior to the discharge formation. However, neither the static pressure or parallel-plate geometry assumptions of Paschen's law are met with hollow cathodes, as there are non-uniform electric and pressure fields. The effect of the hollow cathode geometric influence on breakdown can be seen in Figure 3.2, with large reductions in the breakdown voltage in the centre and left of the Paschen curve, and moderate reductions on the right. This demonstrates that the Paschen curve characteristics still remain applicable for the hollow cathode geometry, unlike that of more extreme geometric changes such as needle-plate cathode anode discharges [75].

There are a few mechanisms that give rise to the hollow cathode effect [20, 76], including: increased secondary emission from the additional bombardment of photons, and metastable

enhancement of ionisation caused by stepwise ionization and the electron pendulum motion in which electrons bounce between the internal cathode surfaces further increasing ionisation incidents. Studies [76-79] have concluded that the high-energy electron pendulum motion is the most significant mechanism that gives rise to the hollow cathode effect.

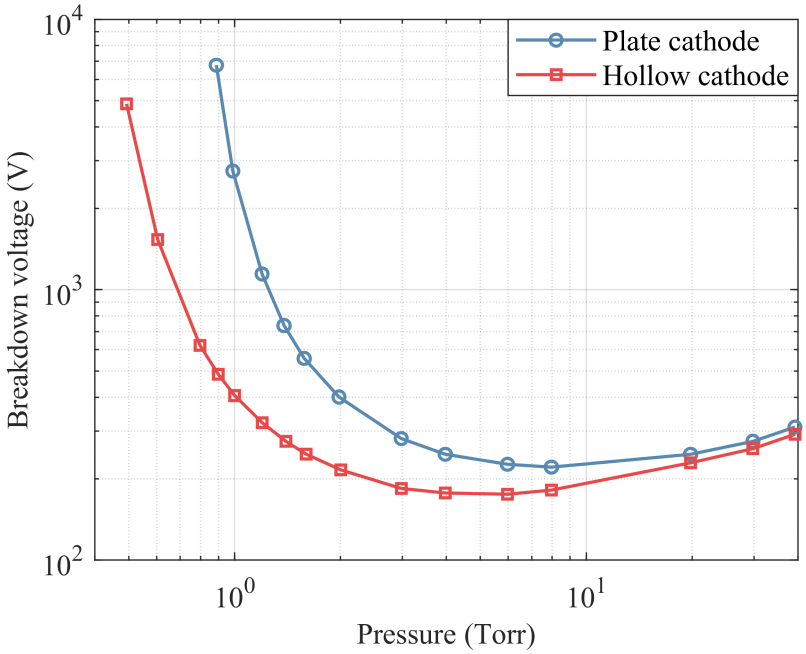

Figure 3.2: Comparison of Paschen breakdown for parallel plates and hollow cathodes, in helium with a 10 mm gap. [76]

3.3 GLOW DISCHARGE THEORY

3.3.1 TRANSFERRING TO GLOW DISCHARGE

The characteristic voltage-current profile of electrical low-pressure gaseous discharges between parallel plates is shown in Figure 3.3. This figure depicts the *V-I* curve measured between the parallel plate anode and cathode with a variable circuit resistance, R, which is decreased in order to increase the current limit. As such, this displays the discharge characteristics of the dark, glow and arc discharge phases.

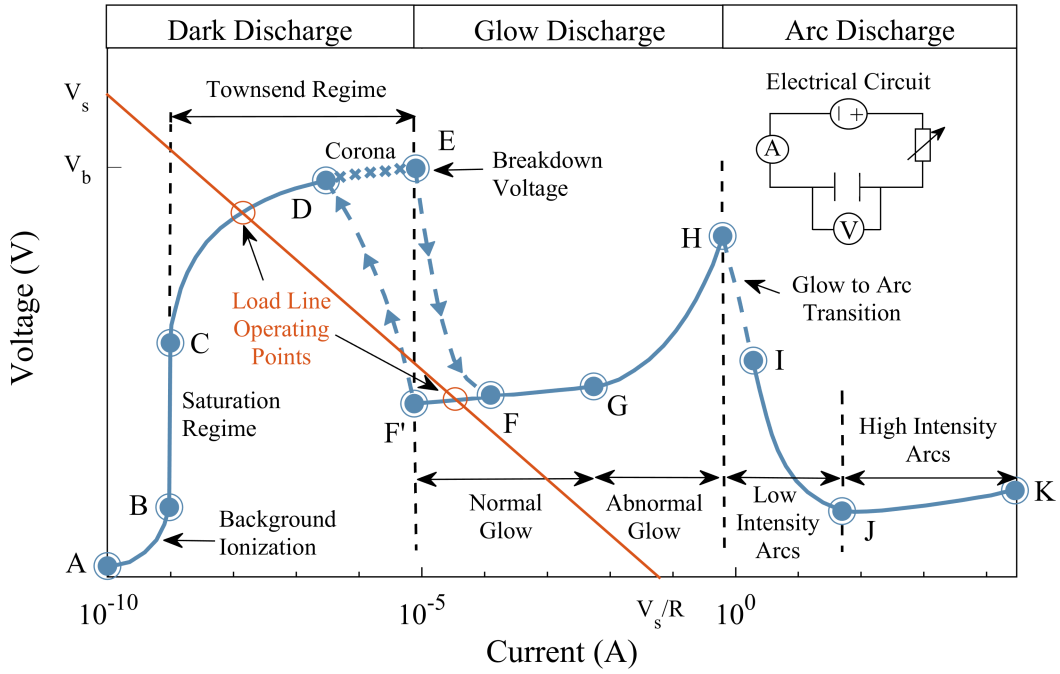

Figure 3.3: Voltage-current characteristics of an electrical gaseous discharge with superimposed load line [80]

The stage **A-B** is a non-sustained discharge such as from cosmic radiation, in the order of $10^{-10} - 10^{-9}$ A. **B-C** is the saturation regime, as increased voltage does not increase electron generation, until point **C**, where the Townsend regime begins, with cascading ionisation. This regime is in the order of $10^{-9} - 10^{-5}$ A. At **D-E** Corona discharge can form, with partial conduction of the gaseous discharge. With further increase in voltage, point **E** is reached and the breakdown voltage is met. At which point the discharge can transfer to a normal glow discharge, point **F**, which is in the order of $10^{-5} - 10^{-2}$ A. Hysteresis can occur on return to the dark discharge, shown from points **F-F'-D. G-H** is the abnormal glow discharge in the order of $10^{-2} - 10^{0}$ A, and **H-I** is the glow to arc transition occurring in the order of $10^{0} - 10^{1}$ A. Finally, **I-K** is the arc discharge in which currents are typically $> 10^{1}$ A.

The actual voltage and current magnitudes for each stage are dependent on numerous operational parameters, such as, the electrode geometry, electric field, gas pressure, gas properties, and electrode material properties. Hence the current ranges shown are just typical experimental values recorded, with operation possible outside the boundaries indicated. For instance Takaki [81] has demonstrated very high current glow discharges, with a normal glow discharge with current >3 A and an abnormal glow discharge achieved with current higher than 100 A. That said, the qualitative characteristics are still considered to be widely applicable, and thus important to understand.

The load line shown superimposed in Figure 3.3 is given by the equation of a closed circuit:

$$V_s = V_p + RI \tag{3.2}$$

where V_s is the supply voltage, V_p is the plasma voltage, I is the current, and R is the circuit resistance. The load line and plasma *V-I* intercept point(s) are the operational point(s). The x-axis intercept is given by $\frac{V_s}{\mathrm{R}}$ and V_s is the y-axis intercept. Increasing the circuit resistance increases the gradient of the load line. The load line may intercept the plasma *V-I* plot at more than one point, as shown, and in such cases the history of the discharge dictates the beginning start condition, though the discharge tends to a minimum power operation.

With very high circuit resistance, and low enough supply voltage, the current will remain small, and the stable discharge formed is referred to as a *dark discharge*. At higher currents, by lowering R or increasing V_s, ionisation increases to the point where the positive space charge accumulates, distorting the electric field and thus forming what is known as a *glow discharge*, where the voltage across the gap drops below the breakdown voltage.

3.3.2 GLOW DISCHARGE CHARACTERISTICS

Glow discharge characteristics can be examined by means of a simple system, such as a long glass cylinder with a negative cathode on the left, and a positive anode on the right, seen in Figure 3.4. Although this is not the same geometry as with a hollow cathode, the symmetry of this model allows for a concise understanding of the space charge influences that result in the classical glow discharge characteristics. In addition, this setup has been well-studied such that there is comprehensive understanding of the phenomenon [28, 68, 82].

From Figure 3.4, the highest potential drop can be seen to be near the cathode surface, referred to as the *cathode fall*. In the cathode fall the energetic ions bombard the cathode surface producing secondary electrons. These secondary electrons accelerate forming a cascading ionisation avalanche within the cathode fall. This causes the electron density to grow rapidly from the cathode surface. This is due to the strong electric field within the cathode fall caused by the high charge density and resulting space charge [70]. This is contrary to the behaviour during breakdown, in which the ionising avalanche is across the entire region between the cathode and anode, with reduced secondary electron emission. Thus, this explains why higher voltages are required during breakdown.

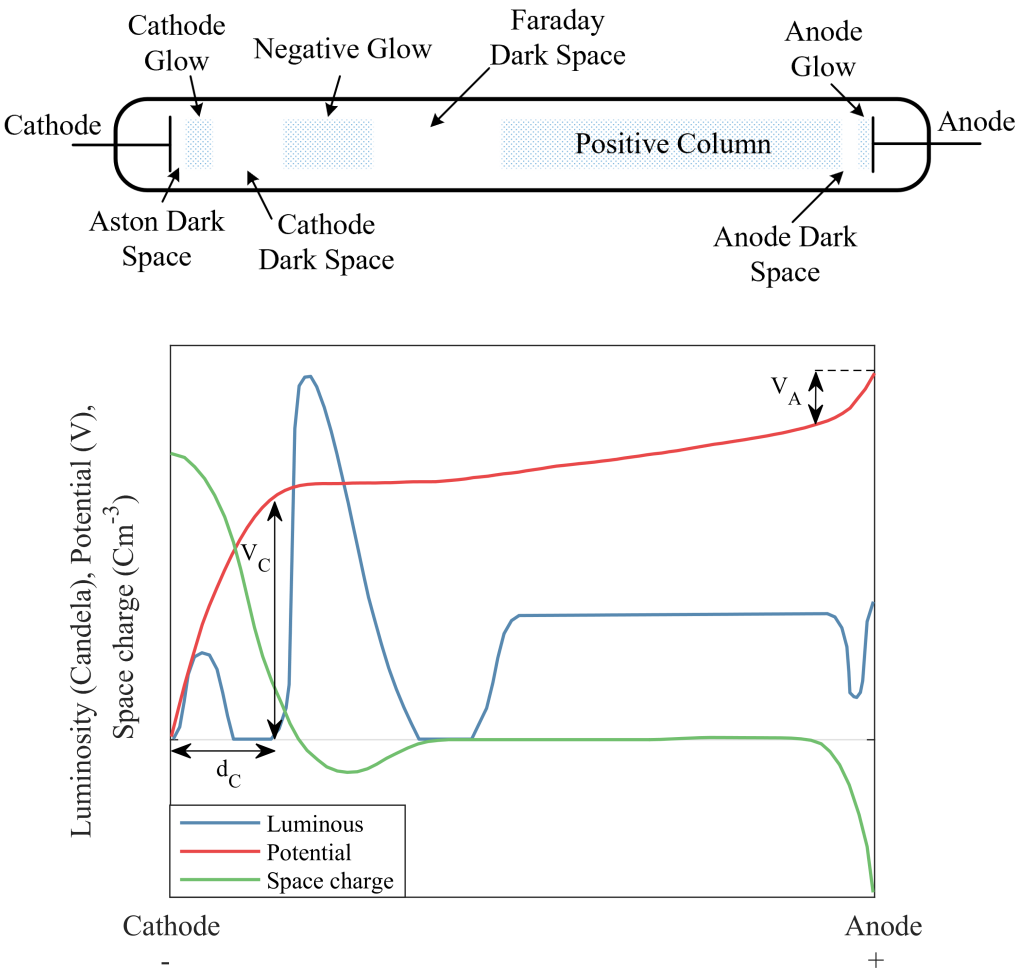

Figure 3.4: Qualitative characteristic of a dc glow discharge [82]

Figure 3.4 shows the characteristic layers of the glow discharge sectioned by the luminance variance, though the cathode fall is defined due to the large potential drop in which the majority of electron production occurs. The *Aston dark space* is where the electrons have been ejected from the cathode at low potentials (<1 eV), beyond which the electric field accelerates the electrons to sufficiently cause excitation - this region is referred to as the *cathode glow*. After, the electrons are accelerated further, beyond the excitation function maxima, this layer is referred to as the *cathode dark space* where electrons excite significantly less and the majority of the electron multiplication in the discharge occurs. Near the cathode, the current is predominantly transferred by ions, as they move significantly slower than the electrons, hence accumulating a positive space charge. Most electrons are generated at the end of the cathode fall due to the ionisation avalanche process; hence, the electron flux becomes large, with energies reducing to the excitation function maxima near the end of the cathode fall with the weakening electric field, causing the creation of the *negative glow* with intense excitation. After this, the energy drops further below the excitation function maxima due to the excitation losses, and thus the *Faraday dark space* is formed. Here

some high energy electrons remain that have had few interactions since being freed, which results in higher electron density prior to the positive column. The longitudinal field then increases to that of the *positive column*, where the plasma is weakly ionised and in non-equilibrium, with electrons in the energy range of 1-2 eV [82]. Though the remainder of the high energy electrons do excite, thus giving the positive column luminescence. A weak field compensates for recombination and other losses in this region. Finally, in the *anode fall*, which comprises of the *anode dark space* and *anode glow*, the anode repels ions and attracts electrons from the column, thus forming a negative space charge, with a higher field accelerating the electrons to the anode.

3.3.3 GLOW DISCHARGE RELATIONS

A key region within the glow discharge process is the cathode fall, as most of the potential drop is across that region. The cathode fall thickness, d_C, is inversely proportional to the pressure, p, and with increasing electrode distance the positive column extends proportionally, with negligible change to the cathode fall thickness. When the electrode separation shortens, the positive column reduces until the feature no longer exists. With further reduction in the electrode separation the Faraday dark space disappears and so on, until only the cathode fall layer is left. If the electrode separation becomes less than d_C, then the glow discharge extinguishes and cannot be ignited. In the normal glow discharge, the discharge current is increased by either, changes in V_s or R, but the current density at the cathode does not change, instead the discharge attachment area increases until there is full attachment of the cathode. At such a point, for further increases in the discharge current the current density at the cathode increases, though this is with increasing voltage, and the discharge has then entered an abnormal glow discharge, as shown in Figure 3.3.

The glow discharge current density at the cathode, J_C, is given by [68]:

$$J_C = \frac{4\epsilon_0 \mu_i V_c^2 (1 + \gamma_{se})}{d^3} \tag{3.3}$$

where μ_i is the ion mobility and V_c is the cathode fall voltage (see Figure 3.4). The cathode fall is in the order of ~80-90% of the total potential drop, the remaining voltage drop is over the anode fall, V_A, which is dependent on pd, gas properties and electrode material. The positive column only requires a little potential to overcome the electron losses, and thus has a small potential drop. The anode fall portion of the total voltage drop is ~10-20% of the total drop [68]. At the anode, the positive ions cannot reach the anode as they are repelled by it, and a negative space charge forms due to the electron current density. Ionic generation at the anode is due to a very small number of ionisation incidents, this ionic production is three orders of magnitude smaller than that of the electron production in the cathode fall, hence $V_A \ll V_C$.

3.3.4 DISCHARGE STABILITY

The discharge can become increasingly unstable by small perturbations in the discharge growing to deactivating levels if the discharge is in an unstable mode. The discharge can enter a stable or unstable state when transitioning from breakdown to a glow discharge, which depends on the *V-I* profile and load line, such that if the load line intersects two points on the *V-I* curve then the stability can be susceptible to current fluctuations. Figure 3.5 shows a simplified section of the plasma *V-I* profile with a load line intersecting two points. Point **A** is unstable, and thus cannot be realised. As when a small perturbation causes an increase in current, $\delta I > 0$, a lower voltage is required to maintain the discharge than provided by the load line. Thus, ionisation is more than the electron losses, so discharge resistance drops and current increases causing the operating point to move to point **B**. If at point **A** and a $\delta I < 0$ occurs, a higher voltage is required to maintain the discharge than the load line as set can provide, hence electron losses increase, until the discharge fully extinguishes. At point **B**, if a $\delta I > 0$ occurs, the load line does not provide sufficient voltage, such that it returns to the original state. Also, if at point **B,** and a $\delta I < 0$ were to occur, such that the operating point moves back toward **A**, the voltage can be maintained, thus not extinguishing, and the operating point will inevitably revert forward to **B**, as it would be in a temporarily unstable state.

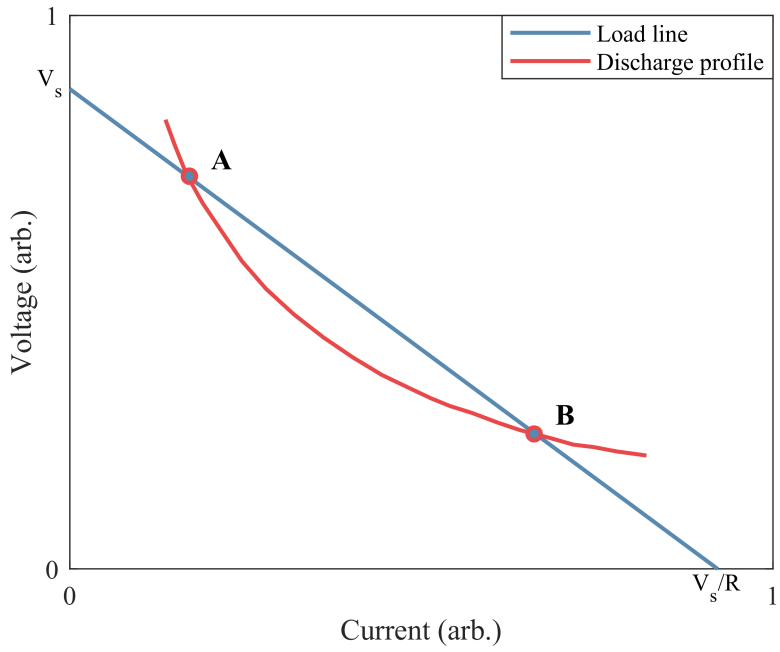

Figure 3.5: Discharge stability modes [68]

Discharge instability is not just due to the load-line and plasma profile intersections as other plasma factors influence the discharge. Gas heating can be a destabilizing factor due to thermal

run away. This is due to the electron temperature, T_e, being proportional to the electric field divided by the gas density, E/N, which is proportional to gas temperature, T_g. As a result, when there is gas heating, there is enhanced ionisation, and an increased local current density. Due to this, Joule heat is released, heating the gas further, thus potentially causing a thermal runaway. This often occurs at higher currents of the glow discharge stage. Though, it can require gas temperature increases of 10-20% to overcome the gas cooling effects and trigger the instability [68].

Another main discharge instability is Maxwellization, where electrons lose large amounts of energy through collisions with atoms exciting or ionising them, which results in a depletion of the energy ranges of the electron population that are sufficient for ionization [83]. If the electron concentrations are high enough, then electrons increasingly collide with one another, redistributing the energy ranges of the electron population. This causes the electron energy spectrum to tend towards a Maxwellian form, in which the fraction of the high energy electrons are larger than when electrons collide only with atoms and do not gain any energy [68]. As this continues the number of electrons with ionisation potential increases, thus increasing ionisation which further increases the population of the electrons. This instability can occur at higher currents where the electron number density is sufficiently large.

These instabilities can lead to discharge contraction or striation formation. Discharge contraction or arcing, is where the discharge attachment localises. This can result in intensive heating due to high-density ion bombardment, which can melt or vaporise small attachment areas on the cathode. This is a very erosive process, which alters the surface topography and in turn the local electric field. Whereas striations is where the discharge separates into discharge segments that can be moving from the anode to the cathode at velocities in the order of 100 m/s or alternatively can be fixed [84]. Striations of a glow discharge can be seen in Figure 3.6.

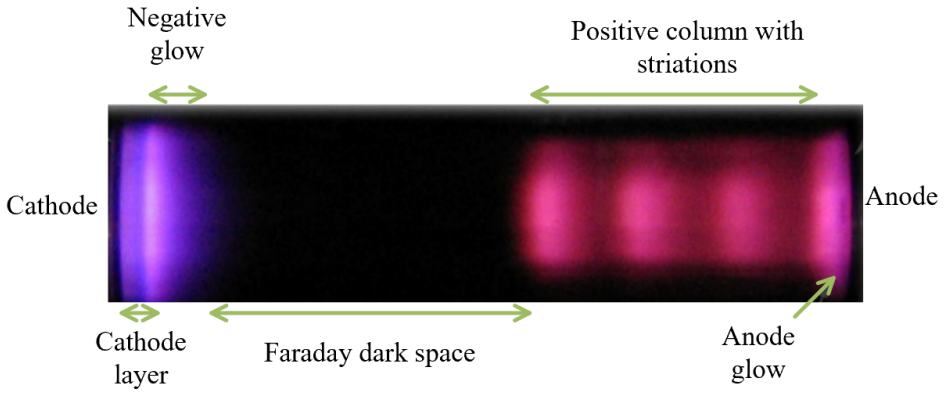

Figure 3.6: Photo of glow discharge striations [68]

3.3.5 GLOW DISCHARGE APPLICABILITY

The ion bombardment of the cathode surface that occurs during the glow discharge transfers energy to the surface of the cathode thus heating the electrode. For HHCs this can be utilised, such that the discharge plasma heats the surface to the required thermionic temperature to transition to the nominal arc discharge operation. Though, it should be noted that energetic ion bombardment of the cathode surface throughout the glow discharge duration can also cause sputtering of the cathode surface, thus eroding the cathode.

Conventional in-space hollow cathodes do not utilise the glow discharge, as they are pre-heated to directly breakdown to a diffusive arc discharge, and thus glow theory is not covered or typically investigated for in-space cathodes. That said, a study [85] has shown that for a micro hollow cathode of 400 μm diameter and at low currents <15 mA the normal and abnormal glow phases are realised, as shown in Figure 3.7.

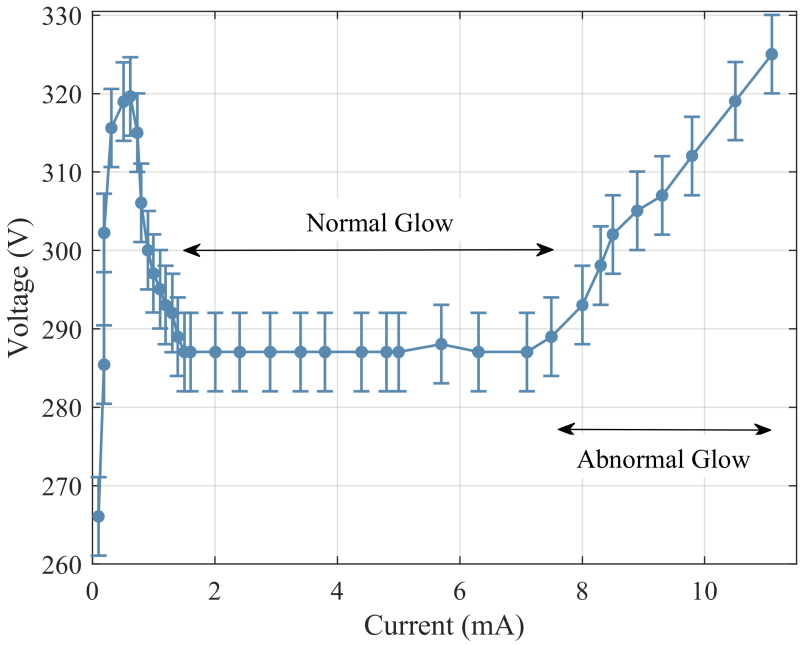

Figure 3.7: *V-I* characteristics for a micro hollow cathode, 400 μm diameter at 40 Torr with Ar [85].

Furthermore, a hollow cathode with comparable geometry to that of a modern in-space cathode, with a Mn cathode that is 15 mm long with a 3 mm inner diameter has been tested with neon backfilled at 3.5 Torr with a discharge current of 3 µA to 4.7 mA to a 7 mm diameter ring anode [86]. These tests investigated the varying transient characteristics from breakdown to glow discharge formation, with breakdown occurring at 268 V, and a 150 V voltage drop occurring in ~100 μs with the glow discharge formation. These results are again similar to the profile that is shown in Figure 3.3. Also, in Schatz's HHC attempts [27], post breakdown a relatively high

voltage discharge formed, of around 300 V, characteristic of glow discharges. However, Schatz's HHC suffered challenging transitions to the thermionic low voltage arcs (<50 V), due to localised melting of the system occurring. This is likely caused by a lack of sufficient emitter heating pre-transition.

These studies indicate that the classical theory is applicable to that of the more complex geometries in HHC ignition, at least for the characteristic *V-I* profile trends. Though further quantitative assessment of the influences of this phase in HHCs is required, in particular to allow a controlled glow discharge phase with sufficient heating power to uniformly raise the emitter temperature, without premature arc transitions that can induce localised melting [27].

3.4 ARC DISCHARGE THEORY

3.4.1 TRANSITION TO ARC DISCHARGE

Arc discharges are a relatively low voltage (<100 V), high current (>1 A) discharge that are primarily sustained through thermionic emission, in contrast to that of glow discharges, in which secondary emission is the primary mechanism sustaining the discharge, thus requiring higher voltages (>150 V). In an arc discharge, the surface of the cathode reaches thermionic temperatures through ion bombardment heating or alternatively by the cathode being externally heated. The thermionic discharge can be attached diffusely across the whole cathode or to localised spots on the cathode, the latter is referred to as *arcing*. Once thermionic emission occurs there is a transition to an arc discharge from the glow discharge, due to the additional thermionically emitted electrons that require low potentials to sustain the discharge. Classically this transition from glow to arc has been achieved by lowering the circuit resistance, R, and thus moving the load line to increase the operating current. This causes the normal glow to transition to the abnormal glow and then to an arc discharge, characterized by a lower voltage, higher current discharge mode, as shown in Figure 3.3. Conventional in-space hollow cathodes do not require this process, as the emitter is pre-heated, typically by an ohmic heater. Thus, the discharge can breakdown and directly form an arc discharge, as the emitter is already thermionically emitting. Heaterless ignition can also breakdown into an arc discharge [87], this is dependent on the load line, and the *V-I* profile, though this approach can lead to discharge localisation as the emitter is not at a uniform thermionic temperature.

3.4.2 ARC DISCHARGE CHARACTERISTICS

The arc discharge is capable of operating at substantially higher currents than the glow discharge. As when a glow discharge operates at higher currents, the ion bombardment heating naturally

transforms the glow discharge to an arc discharge due to the lower power operation of thermionic emission. The potential drop profile of the arc discharge is similar to that of the glow discharge, with a sharp drop near the cathode, and another drop near the anode, and a positive column in between - this can be seen in Figure 3.8. However, there is a higher proportion of the total potential drop at the anode fall, this is due to the large difference in the ion and electron currents at the cathode fall compared with the glow discharge [68]. This disparity is caused by the reduced ionic current as the majority of the current is carried from the electrons, which are generated thermionically. The lower potentials reduce the severity of impact energies of the ion bombardment on the cathode in comparison to that of the glow discharge, though there is higher ion current density to maintain the thermal energy transfer required.

The arc discharge has a lower operating potential, due to the ion bombardment of the cathode resulting in thermionically emitted electrons, rather than the secondary emission in the glow discharge. Hence, the arc discharge is more economical in energy usage for a given current than the glow discharge. The thermionic emission is typically in the range of 70-90% of the total current generated [28, 68]. Additional generation of electrons through ionisation occur, though are significantly less than in the glow discharge for a given current. Therefore, the cathode fall potential in the arc discharge is in the order of the ionisation energy or less, and an order of magnitude less than the glow discharge. In the positive column, the ionic current is small to negligible; this is then increased in the cathode fall to around 10-30% at the cathode surface [68]. These ions in the cathode sheath increase their kinetic energy, some of which is transferred to the cathode surface in the form of heating. The strong electric field at the cathode surface lowers the work function due to the Schottky effect [88]. The anode fall reflects the formation of a negative space charge, as the anode repels the positive ions towards the cathode, again this is in the order of the ionisation potential.

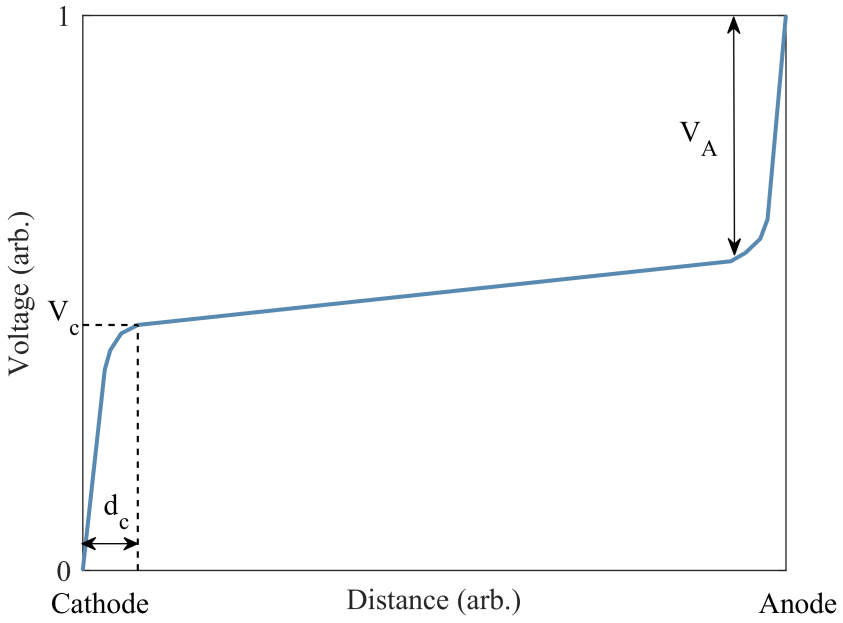

Figure 3.8: Typical distribution of the potential drop in an arc discharge [69]

3.4.3 APPLICATION OF ARC THEORY

As stated prior, the conventional in-space cathodes operate nominally with an arc discharge. Significant effort over the years has gone into development of plasma models [44, 45, 89-91] and plasma diagnostics [92] to examine the plasma properties, such as electron temperature and density, inside the relatively complex HC geometry and flow conditions. When the HHC is operating in a diffusive arc discharge, the discharge mechanisms are expected to be similar to those of conventional hollow cathodes, as the geometry and operating conditions are similar. The main mechanism-based difference for HHCs in comparison to conventional HCs is in the way that the transition to the arc discharge phase occurs. Therefore, determining the operating conditions required to transition to a diffusive arc discharge repeatedly is of more importance than characterising the final HHC arc discharge. That said, if significant geometric or electrical setup changes are made to an HHC in comparison to a HC, this could influence operation in the nominal phase and thus does require consideration.

3.5 SECONDARY ELECTRON EMISSION

Secondary electron emission is where an electron is released from the material surface by the impact of a primary particle. The most important secondary emission mechanism for gas discharges is the ion-electron secondary electron emission. The number of secondary electrons emitted per primary incident is called the secondary emission yield, γ_{se}. This is the main electron

emission mechanism that sustains the glow discharge, and influences both the breakdown and thermionic phases of HHC ignition. With a high γ_{se}, fewer ions are required to reach the surface, so the discharge can be sustained at a lower voltage. However, this is a trade-off involving parameters such as the material sputter yield, which is the number of atoms released from the surface per ion bombardment incident.

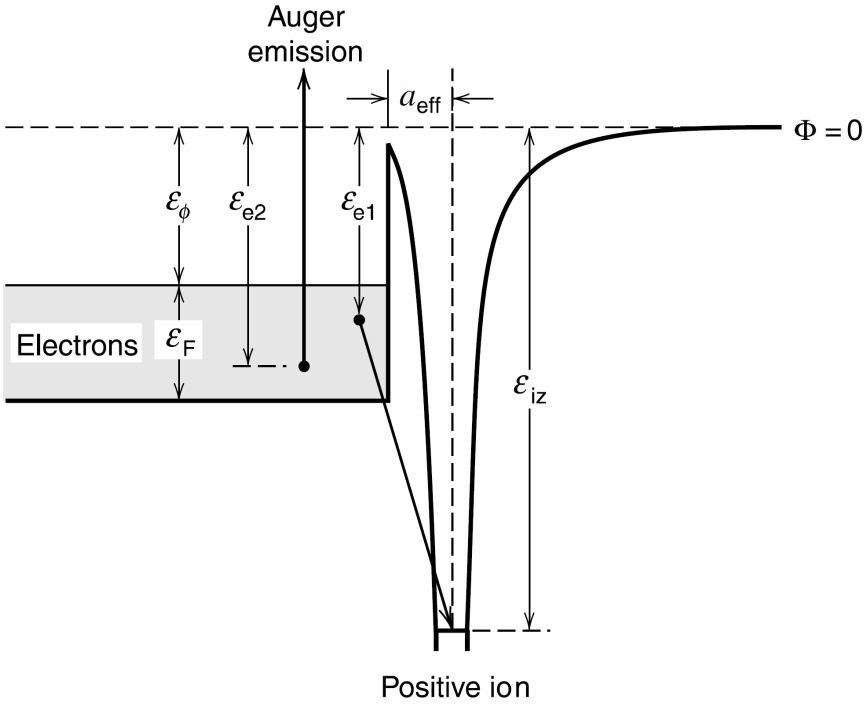

Figure 3.9: Illustration of Auger emission due to electron tunnelling [28]

Essentially all positive ions at the cathode surface in the range 10-1000 V are immediately neutralized for typical plasma processes [28]. Ions in plasma discharges have relatively small kinetic energies which are insufficient to directly, through kinetic collision, transfer sufficient energy to release an electron. The neutralization process is achieved through electron tunnelling. When a positive ion approaches the atomic radius, a_{eff}, of the cathode surface, this creates a deep potential well near the surface, as seen in Figure 3.9, where ε_F is the Fermi energy. There is then a small potential barrier of width $\sim a_{eff}$, such that an electron from the conduction band with energy ε_e, can tunnel through the barrier to neutralize the ion. This electron can enter an excited state and if this is not metastable then it radiates and transitions to ground state or to another metastable state. If the electron when neutralising, enters the ground state of the atom, a second electron from the conduction band absorbs the excess energy of the neutralization. The energy lost by the electron while moving to the ground state is $\Delta\varepsilon = \varepsilon_{iz} - \varepsilon_{e1}$, where ε_{iz} is the potential drop resultant of the positive ion. If $\Delta\varepsilon > \varepsilon_{e2}$, then the second electron is released from the solid

surface. This process is called Auger emission and is the main secondary emission mechanism for typical plasma processes.

A simplified empirical expression for the secondary emission yield, γ_{se}, is given by Raizer [68]

$$\gamma_{se} \approx 0.016(\varepsilon_{\mathrm{iz}} - 2\varepsilon_{\Phi}) \tag{3.4}$$

where $\varepsilon_{\mathrm{iz}}$ is the ionization potential of the primary ion, and ε_{Φ} is the surface work function. To determine accurate information for the secondary electron emission coefficient of a material is challenging due to it being a function of the primary ion energy and mass. For materials such as lanthanum hexaboride, which are in use in hollow cathodes, there is no reliable empirical data on the secondary emission yield available in the literature to the author's knowledge. Data on the secondary emission yield for common materials is shown in Table 3.1.

Table 3.1: Secondary electron emission yield for common materials [93]

Solid	Work Function (V)	Ion	Energy (V)	Υ_{se}
Si (100)	4.90	He^+	100	0.168
		Ar^+	10	0.024
			100	0.027
Ni (111)	4.5	He^+	100	0.170
		Ar^+	10	0.034
			100	0.036
Mo	4.3	He^+	100	0.274
		Ar^+	100	0.115
		N_2^+	100	0.032
		O_2^+	100	0.026
W	4.54	He^+	100	0.263
		Ar^+	10	0.096
			100	0.095
		H_2^+	100	0.029
		N_2^+	100	0.025
		O_2^+	100	0.015

3.6 DIFFUSIVE AND SPOT ATTACHMENT

3.6.1 TRANSITION FROM DIFFUSIVE TO SPOT ATTACHMENT

Cathodic spots are the localisation of the discharge attachment from the whole or most of the available cathodic surface, to a significantly smaller section(s) of the surface, which is typically circular in shape and submillimetre in size [94]. These cathodic spots, which are also referred to as *arcing,* can occure in both the glow and arc discharge phase. They have great importance in determining the erosion characteristics of the heaterless ignition, as any spots that form have high erosion, potentially as high as 10^{-4} g/C [95], which is far higher than uniformly attaching glow or arc discharges. Conventional cathodes can suffer from arcing also [26], but as the cathode is pre-heated the discharge forms on a emitter with relatively uniform temperature, therefor arcing is less likely and less intense than that of HHCs. Moreover, the damage to the surface from the spot discharge (see Figure 3.10) encourages more non-uniform attachment due to the change in the electrical field distribution. Hence, surface conditioning and current control must be conducted to minimise the occurrence of cathodic spot formation, and thus limit the damage caused in heaterless ignition.

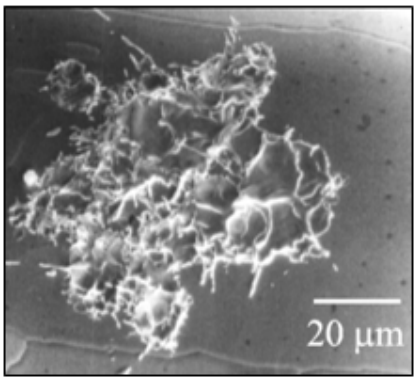

Figure 3.10: SEM of a cathodic spot on a tungsten cathode, with a current of 23 A and burning time of just 1.3 µs [94]

Cathodic spots can occur on hot electrodes, as within arc discharges and on cold electrodes, as within glow discharges. These spots can be in single or multiple locations. On hot electrodes the spot radii are in the 0.5-2 mm range, whereas with cold cathodes, where the discharge cannot be sustained thermionically, the spot radii are <1 mm [94]. This extreme contraction causes a huge local energy transfer, which evaporates the cathode material, as shown in Figure 3.10.

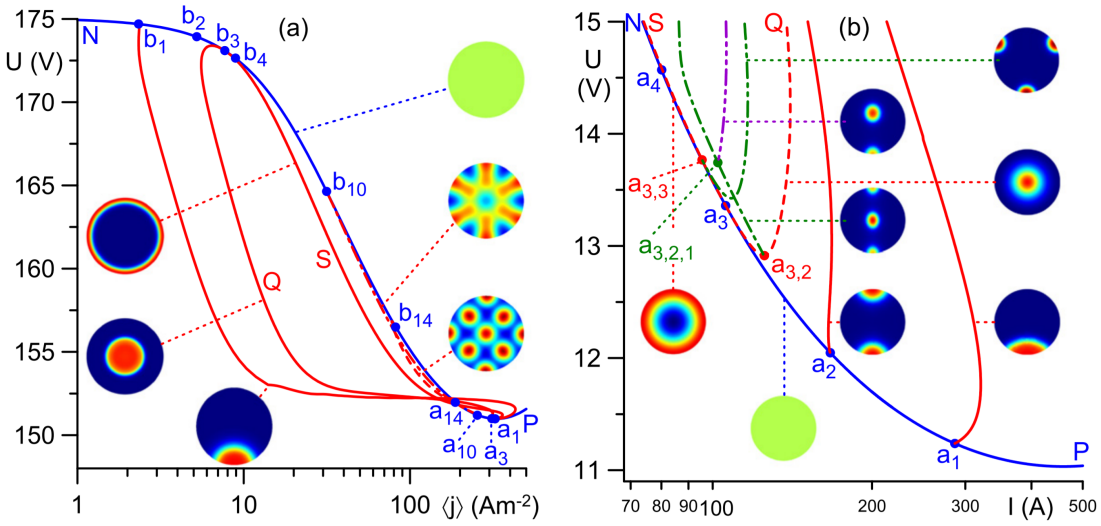

Figure 3.11: Simulation of the V-j characteristics of glow discharge (left) with Xe at 30 Torr and *V-I* characteristics of arc discharge, with Ar at 760 torr (right), both showing diffusive and spot attachment [96]

Figure 3.11 shows the *V-I* difference from a diffusive discharge attachment to single or multiple spot attachments for both glow and arc discharge. For the glow discharge, the spot attachments reduce the voltage, whereas for the arc discharge the voltage increases. The difficulty in determining whether the discharge is in spot or diffuse mode practically is due to the *V-I* characteristics being relatively dependent on cathode material, geometry and operating conditions as discussed. Accordingly, Figure 3.11 is for rod electrodes and for the arc discharge at atmospheric pressure, and hence does not quantitatively represent that of HHCs which operate in the 0.5-50 mbar range. Thus, determination of the operational mode for an HHC based purely on *V-I* characteristics is challenging, especially as can be seen, some of the multiple spot scenarios have very similar *V-I* profiles to that of the diffusive mode. Furthermore, visual inspection of HHCs to determine the discharge attachment mode is challenging due to the dimension sizes, typically with cathode emitters with an ID <5 mm for in-space cathodes, and with the view being additionally obstructed by the keeper electrode.

3.6.2 CATHODIC SPOT PHYSICAL PROCESS

In cathodic spots a dense microplasma is formed from the vapour, which is non-stationary. This vapour-sustained plasma is capable of very high currents at relatively low voltages <50 V. Moreover, process of vaporizing the cathode material can occur without heating the cathode. This is due to the highly localised plasma attachment in the range of 10-100 µm, and very stochastic non-stationary behaviour, moving at speeds of up to 100 m/s [95]. This behaviour makes investigations into this phenomenon extremely difficult. Regardless, a significant amount of work has been conducted, mostly from the 1990s to date [94, 97-99], which has revealed details of the process within these cathodic spots.

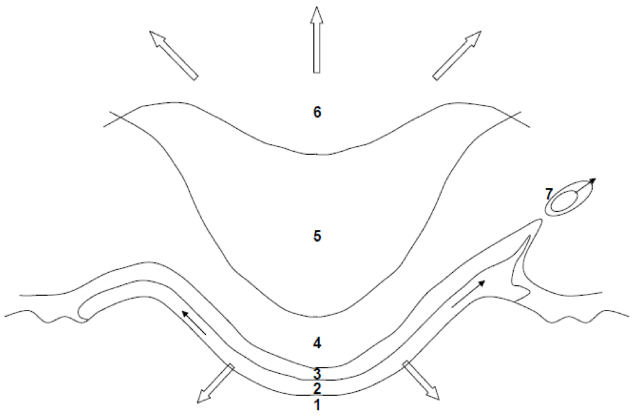

Figure 3.12: Schematic section of a typical developed cathode spot on a clean surface [97]

Figure 3.12 depicts a typical cathode spot, with the following sections: 1) solid surface below the spot (arrows indicate current and heat flow), 2) molten layer, 3) space charge layer, 4) ionization and thermalisation layer of the spot plasma, 5) dense central spot plasma, 6) plasma expansion region (arrows indicate plasma flow), 7) ejection of molten droplets.

The energy to the surface is from Joule heat and impinging ion bombardment as well as energetic electrons - the resultant evaporated cathode material forms the medium for the plasma. Around the cathodic spot, in the direction of the anode, the sheath voltage can be in the order of 15-20 V [94]. The sheath forms the emitted electrons into an energetic beam, while ion bombardment of the surface occurs, thus heating the surface. There is minimal ion-electron interaction in this sheath region. The evaporated atoms have an un-directional velocity distribution from the surface of the cathodic spot, though this changes to a Maxwellian distribution beyond the ballistic region, which is the spot crater. After this region, towards the anode, the electron relaxation region ends - this is where the emitted electrons are thermalized by collisions. Subsequently, a region begins where the vapour is ionised forming a dense plasma [94]. The plasma then expands up to some millimetres depending on the gas pressure [100]. Beilis, in Figure 3.13 [98], has given an example of the electron density and spot radius for time ranges of 50 ns to 1 ms. Over the same time ranges, the temperature decreases from 4600 K to 4000 K and the electric field from $4 * 10^9$ to $1.3 * 10^9$ V/m [98].

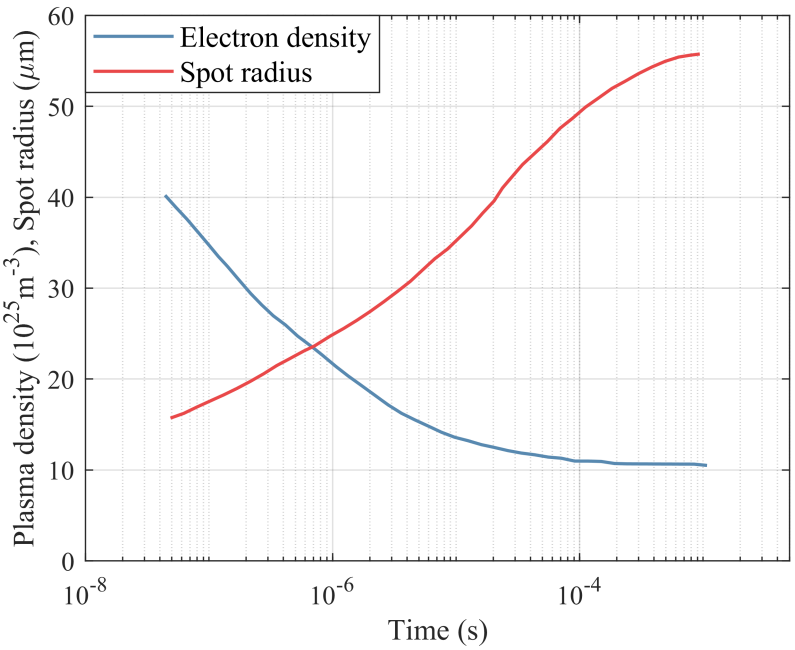

Figure 3.13: Plasma electron density and the spot radius propagation from 50 ns to 1 ms, for a Cu cathode with a cathode fall of 15 V, current of 40 A, and erosion rate of 30 μg/C [98]

3.7 SUMMARY OF THE BACKGROUND THEORY

The classical theory for breakdown of gaseous discharges has been seen to be characteristically applicable to that of hollow cathodes, though there is indication that there may be quantitative drops in V_b when below the pd_{min} with hollow cathode geometry [76], which would be beneficial to HHCs. In addition, Ledernez has determined that with argon discharges, V_b is not only a function of pd, but also a function of d, giving $V_b = f(pd, d)$ [101]. While the heaterless ignition breakdown phase is relatively well captured overall by the classical Paschen law, quantitative differences with the full HHC setup will arise. This is due to the complex electric fields caused by having a hollow-anode to hollow-cathode breakdown with flow, and thus requires characterisation to determine if operation at the Paschen minimum is practically feasible.

The glow discharge theory available is predominantly applied to parallel plates, though has been seen applied for hollow cathodes at very low current (μA), which is difficult to interpret quantifiably for in-space HHCs which operate at several orders of magnitude higher current. Though the classical glow characteristics are seen to be realised for various geometries, at least in terms of the *V-I* profiles, thus indicating it will be a well-suited theory to begin analysis of the HHC heating operation. With the normal glow there is a constant voltage and increasing current until the discharge attachment covers the entire cathode surface, at which point the discharge

transitions to the abnormal glow with an increasing voltage to increase the current density. So, the HHC design must adapt to these new plasma characteristics and testing should determine when the HHC is operating in the normal or abnormal glow discharge.

During glow and the arc discharge phase, spot attachment can occur, where the current density is very high ($10^4 - 10^7$ A/cm^2) [68], melting and even vaporising the cathode material, although the cathode as a whole remains relatively cold. These discharges are unwanted as they are destructive to the cathode surface, and are unstable, moving rapidly and stochastically on the cathode surface; further, they affect the localised electric field and material properties due to the super heating effect. As discussed in Chapter 2 this discharge localisation has resulted in the melting and damage of multiple HHCs [27, 52]. Thus, determining the practical conditions to maintain a diffusive discharge through the ignition phases with the HHC setup is crucial.

When the HHC is in the nominal arc discharge, where electron production is from thermionic emission, the operation is in common with that of conventional hollow cathodes nominal operation. As such the operational characteristics should be similar. Though if there are significant changes to the HHC design in comparison to that of conventional HCs, this can result in changes to the nominal operational characteristics, although the discharge mechanism of thermionic emission should remain. As such, testing should provide comparison of the operational characteristics of the HHC to that of conventional HCs to determine if the design changes have influenced the nominal operation.

CHAPTER 4

EXPERIMENTAL APPARATUS

4.1 INTRODUCTION

The experimental facilities and equipment utilised for the HHC operational characterisation and proof of concept demonstration are described in this chapter. First the electrical scheme employed throughout the main HHC tests is detailed and discussed. Followed by the description of the TDHVL-VC1 vacuum facility utilised, which is a high throughput vacuum chamber system that allows for conventional flow operation of the HHC with an anode discharge. The additional vacuum facility utilised, TDHVL-VC3, enables backfilled testing as well as conventional flow experiments. As such, the latter was used for both enclosed and open keeper discharge experimentation. The open keeper tests allow greater access for instrumentation and parameter changes then the conventional enclosed flow setup. Furthermore, the various diagnostic instrumentation used and integrated into the HHC for characterisation are detailed, these include the pyrometer, thermocouple and spectrographic discharge measurements. Finally, the ignition and conditioning procedures developed for the HHC are outlined.

4.2 ELECTRICAL APPARATUS

An overview of the electrical scheme developed for the high current heaterless hollow cathode system can be seen in Figure 4.1. An EA-PS 9750-12, 750V-12A power supply, applies a potential to the keeper, through the Ignition Control System (ICS), that stabilises the current rise during ignition. The ICS consists of three main components; firstly a BYX42 diode rated for a reverse voltage up to 1200 V and a steady state current of 12 A, secondly, a 150 mH inductor bank

containing 3 Type C30 50 mH inductors with a accuracy of 10% and a steady state current rating of up to 8 A, and thirdly, a 800 Ω thermistor bank containing 80 EPCOS NTC 10 Ω thermistors with a accuracy of ± 20%, and a steady state current rating of up to 8 A.

The keeper-cathode voltage and current is measured by a Pico Technology TA042 differential voltage probe, that measures up to 1400 V with an accuracy of ±2%, and a LEM Model PR1030 current probe, which can measure up to 1000 A with an accuracy of ±1% read value plus 500 mA. Both probes are connected to a Tektronix DPO3034, 300MHz, 2.5 Gsps Digital Oscilloscope which displays and records the data. An EA-PS 9200-70, 200V-70A power supply applies the potential to the anode, for igniting and maintaining an anode discharge. The probes, scope, and power supplies are manufacture calibrated. Both the keeper and anode supply negatives are connected to a star ground point. With heaterless ignition, a separate power supply for the heating stage is not required due to the plasma heating the emitter from cold.

The thermocouple instrumentation is connected to a manufacture calibrated Pico Tech TC-08 logger, which along with the power supplies, oscilloscope, MFCs, and pressure gauges are connected to a PC and logged by a LabView program. The LabView interface allows for both direct operational control and 4 Hz logging of all the applicable equipment. The electrical discharges can cause interference to the PC control system, so all interfaces between the control system and test apparatus are isolated via inline USB/RS232 optocouplers. The electrical system used is the same for the vacuum facilities described in the following sections, except for the anode power supply, which is not used with the keeper discharge facility, as no anode is present in those tests.

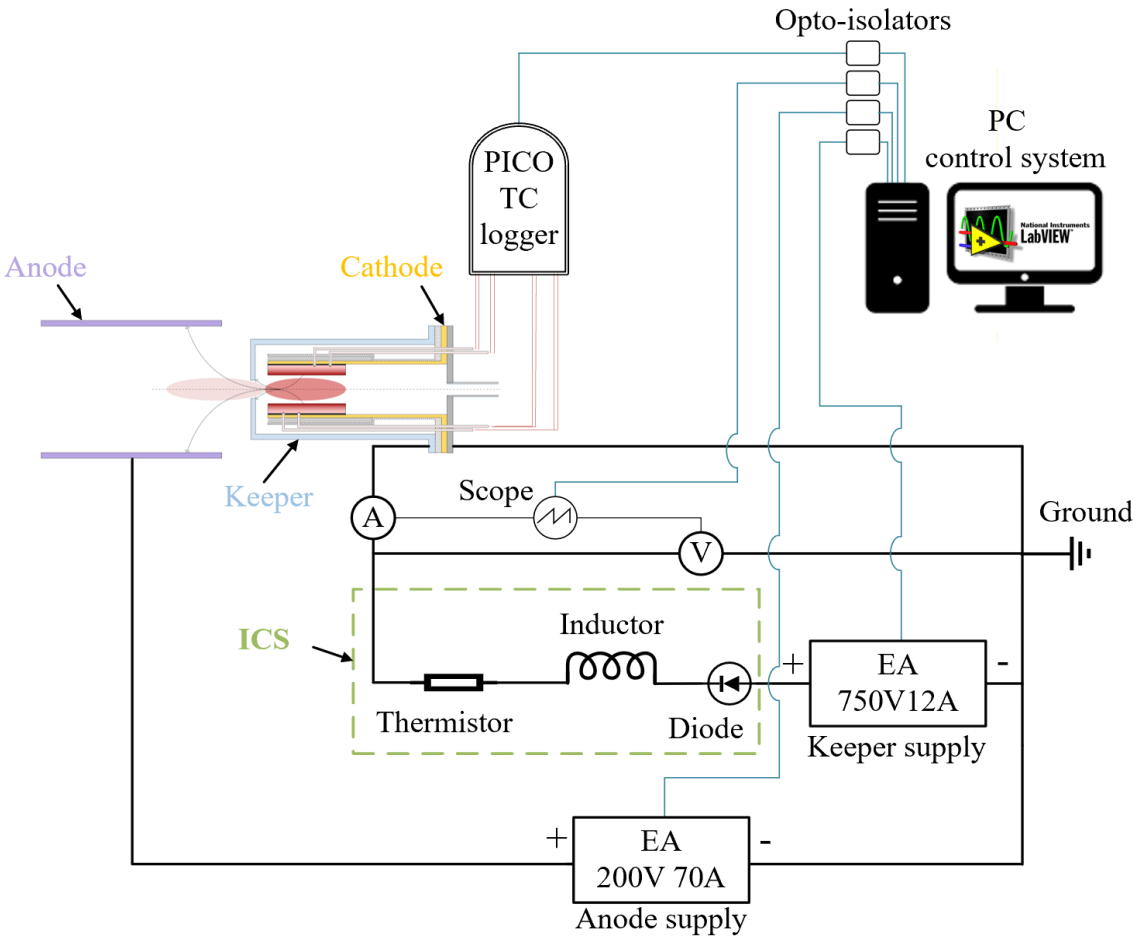

Figure 4.1: Heaterless hollow cathode electrical scheme.

4.3 ANODE DISCHARGE TESTING FACILITY

To test the HHC with gas flow and an anode discharge, TDHVL-VC1 is utilised (see Figure 4.2). The chamber is 1.2 m long and 0.6 m in diameter with a hinged door for quick access, and a 0.1 m diameter view port at the far end for optical access. The chamber system is roughed and backed by an Edwards E2M80 pump with two ultra-high throughput Edwards STP-iXA4506C turbomolecular maglev pumps giving a combined 8600 L/s (N_2) pumping speed. The system reaches a base pressure of $<1*10^{-8}$ mbar and maintains a pressure $<5*10^{-5}$ mbar during all the flow tests conducted on the HHC. The low vacuum pressure is measured with an Applied Vacuum calibrated Edwards APG-M Active Pirani Gauge, with an Edwards active gauge controller. The high vacuum pressure is measured with a manufacture calibrated Kurt J. Lesker 354 Series Ion Gauge, with pre-configured correction factors for the gasses used.

The VC1 door has a mounting plate on the inside which the HHC attaches to. Also, there are four NW40CF as well as one NW16CF ports on the door for various electrical and gas feedthroughs. The cathode is electrically connected to the mounting plate, which is grounded, the mounting plate in turn is connected to the door via support rail. The anode was also mounted to the support rail system, with slots in the rail system allowing the separation between anode and cathode to be varied (d_{k-a}), this is nominally set to 20 mm. Both the cathode mounting plate and anode were supported with Macor stand-offs from the support rail to provide electrical and thermal insulation.

Around 1.5 m upstream from the HHC a manufacture calibrated Applied Vacuum Barometric 0.5-25 mbar dial gauge measures the propellant line pressure, with an accuracy of ± 0.25 mbar. Upstream from the dial gauge a manufacture calibrated Bronkhorst EL-FLOW mass flow controller (MFC) sets the HHC flow rate, with a 0-20 sccm range and an accuracy of ±0.5% read value plus ±0.1% full scale value, such that the maximum error (at 20 sccm) is ±0.12 sccm. The MFC is connected to the regulator of the corresponding noble gas cylinder used for the experiment. The following gases and corresponding purities were utilised for the HHC testing: Ar (N5), $ArH_2$1% (N5), Kr (N5), $KrH_2$1% (N5), and Xe (N4.8), where N5 is 99.999% and N4.8 is 99.998% pure. This purity is sufficient given that the emitter employed is LaB_6 and not BaO-W (see Section 5.2.2). 1/4 and 1/8 inch Swagelok fittings are use throughout the propellant line system and are leak tested prior to operation.

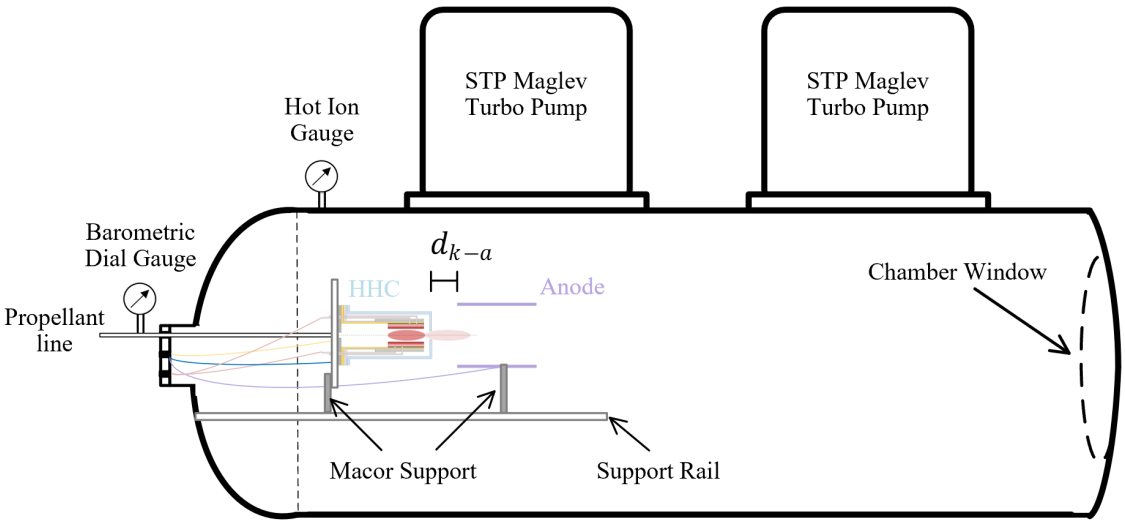

Figure 4.2: TDHVL - VC1 vacuum facility, with the HHC anode discharge configuration.

4.4 KEEPER DISCHARGE TESTING FACILITY

TDHVL - VC3 vacuum facility (see Figure 4.3) was utilized for testing due to the backfilling capability. The facility consists of a 35 cm diameter spherical stainless-steel vacuum chamber, with numerous CF16, CF40 & CF100 flanges, allowing for easy instrumentation access and mounting. An Edwards RV5 vacuum pump reduces the chamber base pressure to ~ $9*10^{-3}$ mbar at which point an Edwards Next 400D turbo pump controlled via the PC interface, lowers and maintains a base pressure of < $1*10^{-6}$ mbar prior to operation. A gate valve is connected between the turbo pump and the vacuum chamber to allow isolation of the turbo pump, so that backfilling is possible. The chamber pressure was measured by a Pfeiffer Balzers IKR-020 Penning gauge and a TPR 010 Pirani gauge, displayed on a TPG-300 vacuum gauge controller, correction factors are implemented for the operating gas, though the inaccuracy beyond 0.5 mbar for noble gases is too great to measure the backfilled pressures, > 0.5 mbar. Thus, the Barometric 0.5-25 mbar dial gauge was utilised to determine the backfilled pressure as well as the propellant line pressure when flow is used.

The system backfilling is conducted by reducing the pressure to < $5*10^{-8}$ mbar, to remove gas impurities from the system. Then the chamber isolation valve is closed, and the pressure is rapidly raised by utilising a bypass valve, such that within ~5 seconds the whole chamber reaches close to the required pressure (typically 2-10 mbar) and further fine pressure adjustment is conducted by the prior discussed MFC propellant system.

The VC3 HHC backfilled configuration is shown in Figure 4.3, where the keeper from the HHC (see Figure 5.1) is removed, and an open keeper is placed downstream of the cathode, with the system backfilled as described. The chamber window allows for direct pyrometer measurements of the HHC emitter and analysis of optical emission from the cathode-keeper discharge, through a fibre mounted on the window. Additionally, keeper discharge flow tests are conducted in VC3 (see Figure 4.4), in such tests the HHC is tested with the original enclosed keeper attached with the flow injected through the cathode propellant line and the system is not backfilled. In both these VC3 configurations, no anode is utilised.

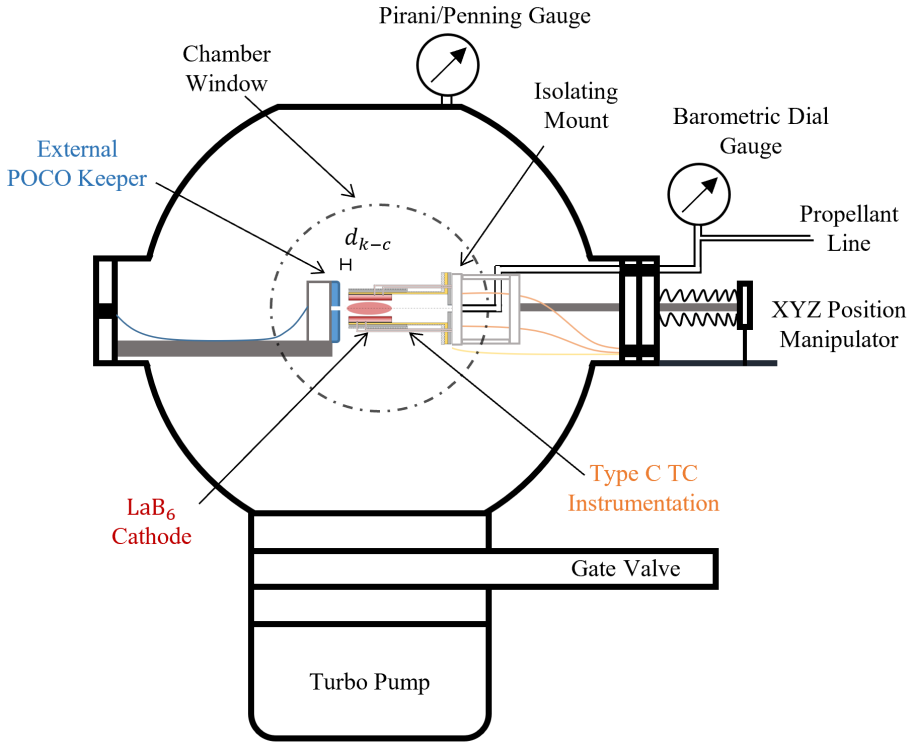

Figure 4.3: TDHVL - VC3 vacuum facility, with the backfilled open keeper HHC configuration.

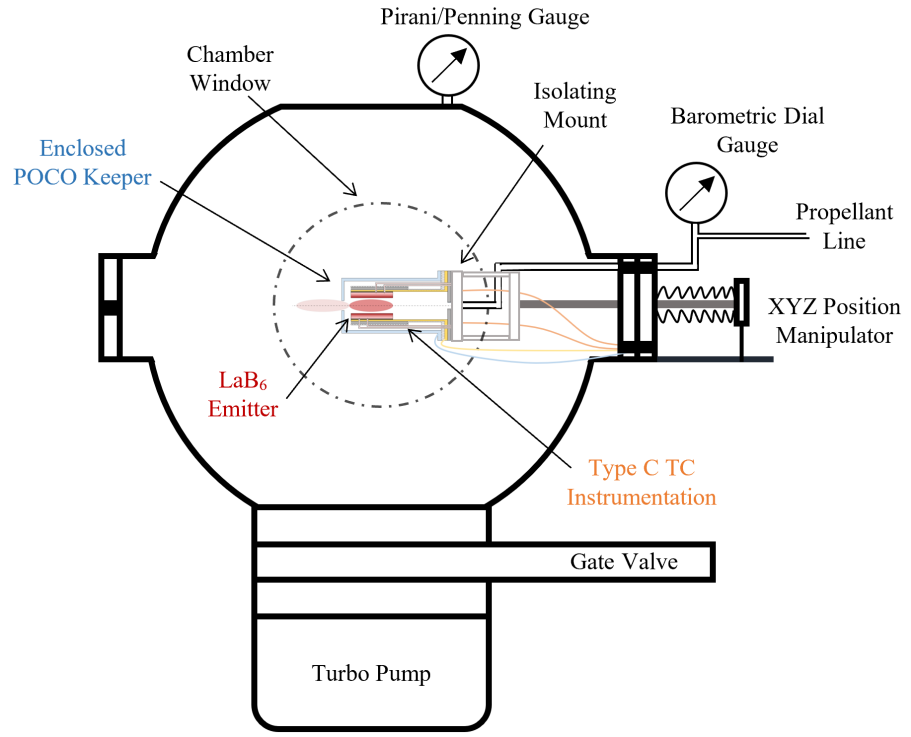

Figure 4.4: TDHVL - VC3 vacuum facility, with the flow enclosed keeper HHC configuration.

4.5 DIAGNOSTIC INSTRUMENTATION

4.5.1 PYROMETER MEASUREMENTS

The backfilled open keeper configuration allows direct optical access of the emitter surface, thus allowing optical thermal measurements of the emitter (see Figure 5.1 & Figure 4.5). Optical access is viable with a keeper-emitter separation ≥2 mm, with the emitter downstream annular surface and central hole edge being visible. The upstream view of the inner-hollow emitter surface was very limited by the viewing angle and keeper obstruction. Measurements are taken on the annular surface, to avoid interference from the plasma radiation, which is strongest in the central hollow emitter region, though typically the measurement difference across the whole viewed emitter surface was less than 50 °C.

These measurements are conducted with a manufacturer calibrated Spectrodyne Inc. DFP 2000 portable disappearing filament optical pyrometer. This pyrometer operates at a wavelength, λ, of 0.65 μm, and has a total range of 760 °C to 4200 °C. The pyrometer range operated in these experiments maintained an accuracy of 0.3% of the measurement reading $\pm$1 °C. For accurate pyrometer measurements corrections are required for the emissivity, ε, of the target at the measured wavelength. In addition, adjustment to the emissivity is required to take account of the chamber window optical transmittance, ζ, at λ, such that the effective emissivity $\varepsilon_{\lambda_{e,\zeta}} = \varepsilon_\lambda \, \zeta_\lambda$ [102]. For the borosilicate glass window of the chamber the optical transmittance is taken to be $\zeta_\lambda = 0.91$ and the LaB_6 emissivity [103] is:

$$\varepsilon_\lambda = 1.2144 - 2.467 * 10^{-4} T_i \tag{3.1}$$

So to correct from the indicated temperature, T_i, in K, measured by the pyrometer at $\lambda = 650$ μm to the true surface temperature T_t in K [104]:

$$T_t = \frac{1}{\left(\frac{1}{T_i}\right) + \left(\frac{log\, \varepsilon_{\lambda_{e,\zeta}}}{9613}\right)} \tag{3.2}$$

4.5.2 THERMOCOUPLE MEASUREMENTS

To assess the emitter heating profile during ignition, the emitter has integrated thermocouple instrumentation. Due to the high operating temperatures of LaB_6 HCs, standard Type K thermocouples that can withstand ~1100 °C are incapable of this operation. Thus, Type C thermocouples, that consist of W5%Re95% and W26%Re74%, which operate up to 2325 °C in

steady state and up to 2760 °C in short-term exposure [105] were utilised. Though such ultra-high temperature operation is not required as this application should reach a maximum of 1700 °C. The accuracy of the thermocouple is ±4.5 °C up to 450 °C beyond which it is ±1% reading.

As there are possible issues with boron diffusion and the thermocouples [106], the thermocouple tips had a high temperature carbon paste sheath, mechanically isolating the thermocouples from the emitter, while aiding the thermal contact. The thermocouples are sheathed in dual bore alumina tubing. The alumina tubing network, which can withstand up to 1900 °C, insulates the thermocouple wires throughout the cathode as can be seen in Figure 5.1.

To minimize the thermal impact, as the thermocouple is an intrusive instrument, the two-bore alumina tube is as small as reasonably possible, with an outer diameter of 1.3 mm, and each bore inner diameter being 0.3 mm, with the thermocouple wire diameter of 0.127 mm. There are four thermocouple measurement locations to determine the emitter thermal profile throughout operation, see Figure 4.5. The thermocouples are inserted perpendicular to the cylindrical cathode surface, through the thermal shielding, cathode tube, emitter sleeve and partially through the emitter. The thermocouples are oriented at equal azimuthal and radial increments along the emitter, such that each thermocouple is at 45° azimuthal increments. The respective axial distances as a ratio of the total emitter length, l, from the emitter tip is: $l/5$, $2l/5$, $3l/5$ and $4l/5$.

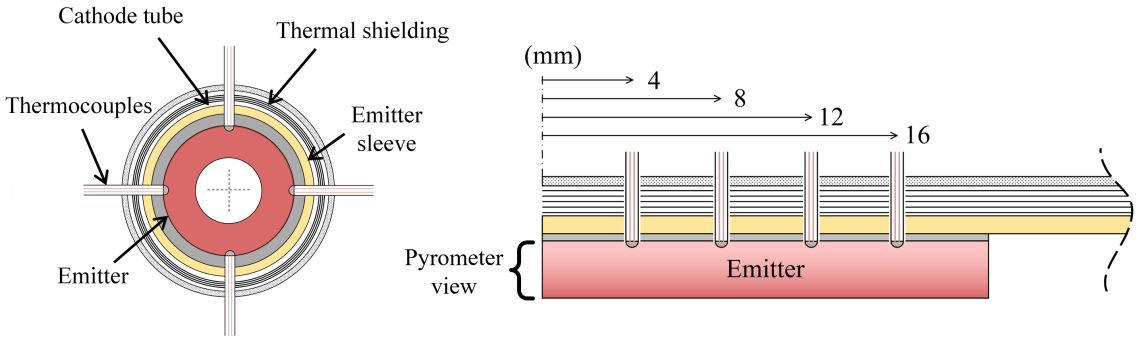

Figure 4.5: Thermal instrumentation measurement locations, front view (left), side view (right).

A good thermal contact between the thermocouples and emitter is highly challenging for hollow cathodes, given the size of the emitter, and multiple concentric parts. One of the largest in-space LaB_6 cathodes [106], has employed Type C thermocouples axially through the emitter, in a spring mounted system to ensure good thermal contact. However, the HHC emitter here is significantly smaller, such that the thermocouples are too large for such an approach. Thus, instead the HHC has radially embedded thermocouples, though this is more challenging for maintaining contact pressure. Numerous attempts were made to ensure good thermal contact with the emitter. The

most successful option was to apply mechanical pressure on the thermocouple in the direction of the emitter and set them in place with zirconia ceramic paste [107].

This process was found to reliably electrically connect the thermocouple to the emitter, though this was still insufficient for proper thermal contact. The thermocouple measurements were found to have large discrepancies with the theoretical emitter temperature values, hence extensive investigations and modifications to the system were conducted to determine the cause. The pyrometer and thermocouple measurements are shown compared in Figure 4.6. The measurements are taken on the same target, a Mars Space ltd heater for a conventional cathode. Pyrometer measurements are taken of the heater surface and of the thermocouple tip which was in contact with the heater surface, as shown in Figure 4.7. This is compared with the thermocouple reading itself. The surface temperature reading by the pyrometer and thermocouple has a difference of around 80 °C at 80 W and grows to 110 °C difference at 152 W. However, the thermocouple reading compared with the pyrometer measurements of the thermocouple tip have very good agreement, with an average difference of 0.9% equating to 9 °C. This is very good considering the disappearing filament pyrometer is subject to operator perception. This cross validation indicates that the pyrometer measurements and that of the thermocouples are reasonably accurate, however the thermocouple measurement is not accurately determining the magnitude of the contact surface temperature. This can be visibly seen in the photo of the test operation in Figure 4.7, with a brightness reduction in the thermocouple compared with the heater surface.

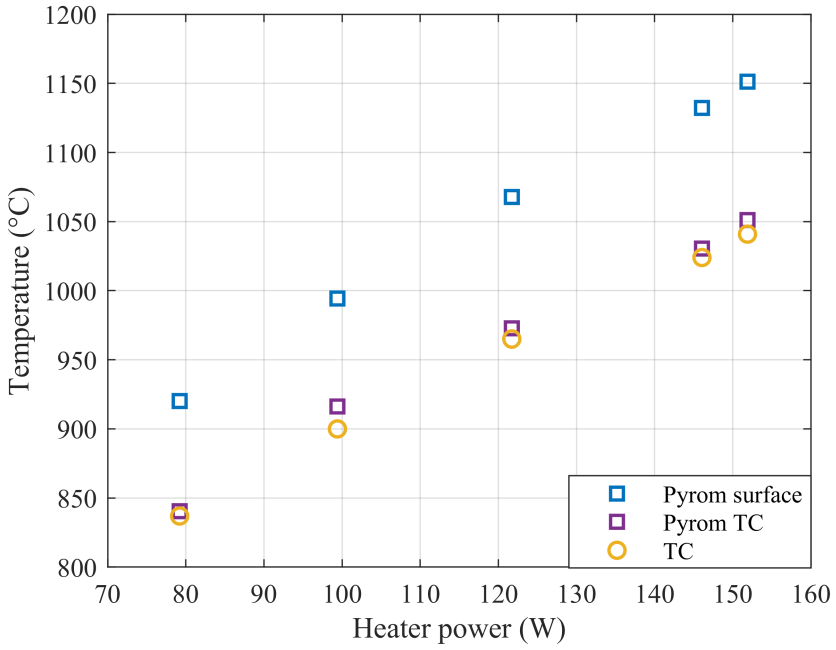

Figure 4.6: Pyrometer temperature measurements of the heater surface and thermocouple tip compared with the thermocouple readings, for varying heater power.

The contact area and pressure applied was too small to achieve sufficient thermal contact, which causes the temperature difference seen. Several attempts were made to experimentally rectify this on the HHC including carbon pasting the thermocouples to the emitter, however due to the size of this hollow cathode system and temperature the emitter reaches, it was challenging to acquire adequate thermal contact for accurate measurements of the temperature magnitude. Though the repeatability of the results indicated good reliability for the trend analysis of the emitter temperature profile from T_1 to T_4. As such the thermocouples allow for emitter thermal trend analysis, to identify the qualitative emitter temperature profile through ignition.

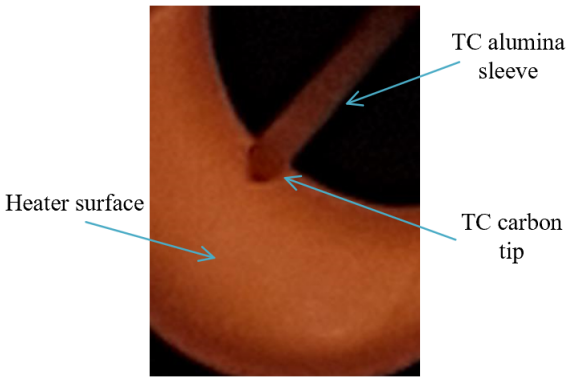

Figure 4.7: Thermocouple contact temperature difference with a conventional cathode heater

4.5.3 SPECTROGRAPHIC PLASMA ANALYSIS

Optical emission spectrographic analysis of the hollow cathode discharge is conducted to determine the plasma electron number density in the backfilled configuration (see Figure 5.2). The optical system consists of a FG200AEA, 200 um, 0.22 NA, optical fibre which is mounted to the chamber window. This fibre mounting gives a line of sight over the emitter-keeper discharge, such that the electron density measured is an average over the length and cross-section of the emitter-keeper discharge. During the plasma density measurements, the emitter-keeper separation was set to 4 mm, and the discharge cross-section is not contained due to the open keeper used in the backfilled configuration. The fibre connects to a Princeton Instruments SP-2750, 0.750 meter focal length, triple grating imaging spectrograph, with a PI-MAX 3 1024i ICCD camera. The highest resolution grating of 2400 gr/mm was used for these experiments. The system is wavelength and intensity calibrated by an Ocean Optics HG-1 mercury-argon source and an Ocean Optics DH-3P-CAL deuterium-tungsten source respectively. The spectrograph is

operated with PI WinSpec software. A gain of 100 was used for the data gathering combined with a gate width of 0.5 to 2 seconds. Each spectrum taken was a set of 10 accumulations, which increases signal to noise ratio, and each plasma density measurement is a mean of at least 4 spectra sets.

The plasma electron density is estimated via the H_2 Balmer series Stark broadening approach which is outlined by Konjević [108]. This links the broadening of the $\lambda_{H-\beta}$ line at 486.135 nm to the plasma electron density. These measurements are conducted utilising a processing script produced by the PATH consortium [1, 109]. To enable $\lambda_{H-\beta}$ broadening measurements the HHC was operated with 1% H_2 for argon and krypton, such that the gas mixtures used were $ArH_2$1% and $KrH_2$1%. The addition of 1-3% H_2 is typically employed for such measurements [108, 110] to attain a measurable intensity of the $\lambda_{H-\beta}$ line to enable calculation of the plasma density with minimal interference to the plasma properties, as non-negligible collisional quenching of Ar excited states and ions start at mixtures above 15% [111]. Attempts for plasma electron density measurements with Xe, with mixtures of 1-10% H_2, proved unsuccessful due to intense emissions concealing the H-β line. The H-β line broadening under plasma conditions such as those found within in-space cathodes with electron densities typically around $1*10^{19}$ - $1*10^{21}$ m^{-3} and electron temperatures around 1-3 eV are affected by the following broadening mechanisms:

- Stark broadening, in which the emitter's natural emission frequency is altered by the plasma's local electric field and is hence sensitive to changes in plasma density. This effect is characterized approximately by the Voigt profile at low plasma densities.
- Doppler broadening, from the thermal motion of the emitter changing the observed emission frequency, and as such is sensitive to the gas temperature. This effect is characterized by a Gaussian profile shape.
- Instrumental broadening related to the spectrometer optical system, which is characterized by a Gaussian profile shape.

The instrumental function of the spectrometer is a Gaussian profile with a wavelength dependent full width at half maximum (FWHM), $w_I(\lambda)$. Utilising the wavelength calibration source, for this optical system w_I, at a wavelength λ, in nm, was found to be

$$w_I(\lambda) = 0.0451 - 3.4168 \cdot \lambda \tag{4.1}$$

A Voigt profile fit is applied to the H-β experimental profile, which was found by Konjević to provide a suitable approximation. Though as seen in the data (see Figure 4.8), for this plasma a

single ionised lanthanum line at 486.091 nm overlays the H-β line at 486.135 nm. Thus, an additional Gaussian fit is required to be applied to the La II line, and then convoluted to the formed H-β fit to confirm the overall fit. The final convoluted fit can be seen to have good agreement with the experimental data, as shown in Figure 4.8. The formed H-β fit is correlated to the electron density, n_e, in m^3 by [108]

$$n_e = 10^{22} * (0.94666 * w_s)^{1.49} \tag{4.2}$$

where w_s in nm is the H-β FWHM given by

$$w_s = \left(w_V^{1.4} - w_{D,I}^{1.4}\right)^{1/14} \tag{4.3}$$

and where w_V is the Voigt profile FWHM, (see Figure 4.8), $w_{D,I}$ is the FWHM of the Gaussian resulting from convolution of doppler, w_D, and instrumental broadening, w_I, profiles and given by

$$w_{DI} = (w_D^2 + w_I^2)^{0.5} \tag{4.4}$$

Finally, the doppler broadening, w_D, is given by [112]

$$w_D = \lambda_{H-\beta} \left(8ln\,2 \frac{k_b T_g}{M_a c^2}\right)^{0.5} \tag{4.5}$$

where k_b is the Boltzmann constant in m^2 kg s^{-2} K^{-1}, M_a is the mass of the H-β emitter, $1.66 * 10^{-27}$ Kg, c is the speed of light and T_g is the gas temperature in K, taken to be from 2000-8000 K, as shown in Figure 4.9. It can be seen the gas temperature uncertainty has a relatively small influence on the electron density estimation, in addition there is good repeatability between measurement sets.

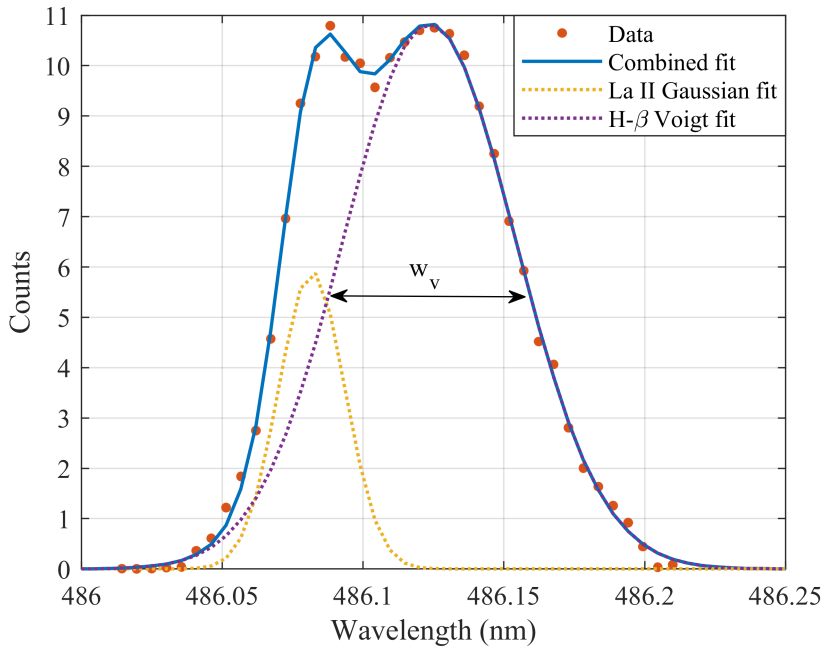

Figure 4.8: Spectra profile fitting, for the backfilled open keeper configuration with a 1 A, 5.5 mbar (Ar) discharge.

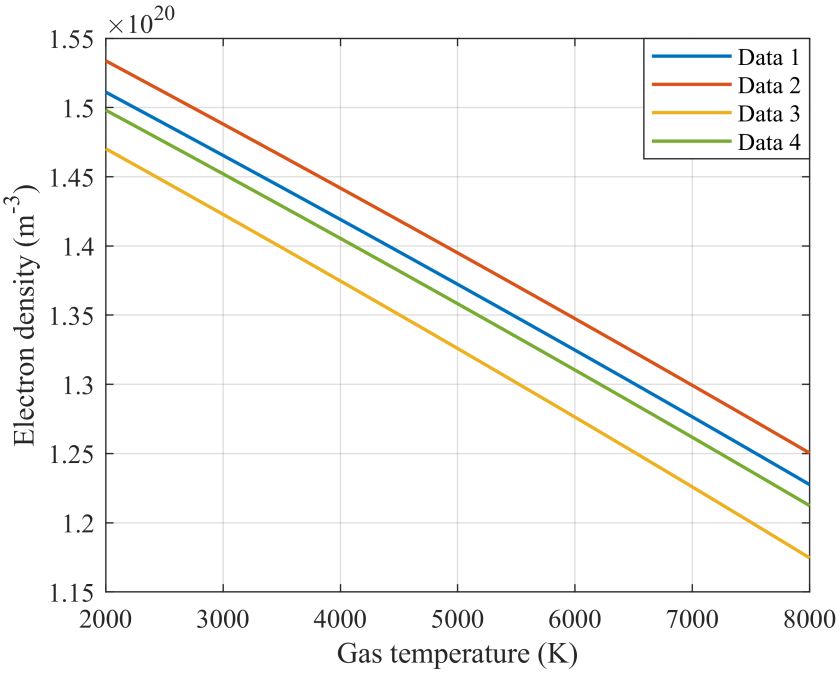

Figure 4.9: Electron density as a function of gas temperature, for the backfilled open keeper configuration with a 1 A, 5.5 mbar (Ar) discharge.

4.6 OPERATIONAL PROCEDURES

A different ignition procedure is required for the HHC compared with conventional HCs, due to the heating occurring through the discharge rather than requiring a dedicated heater component. Furthermore, HCs are routinely conditioned after being in atmosphere, this conditioning procedure entails the cathode's heater power being slowly increased in high vacuum to bake the cathode and all the internal components to remove excess impurities in the system and reduce the possibility for emitter poisoning. Thus, to achieve this with the heaterless system a separate conditioning process has been developed.

4.6.1 CONDITIONING PROCEDURE

The conditioning procedure developed for the HHC has an overview flow chart, see Figure 4.10 and follows the outlined procedure below.

1) **Post-manufacture cleansing**: For a newly manufactured HHC the pre-cleansing procedure is completed first as the physical parts of the hollow cathode will have impurities left over from fabrication which must be removed.
    a. All the HHC parts, including bolts, nuts and washers, are cleaned in an ultra-sonic bath for around 30 minutes, in acetone and then isopropanol.
    b. The emitter sleeve is baked at over 1000 °C in high vacuum ($<1*10^{-6}$ mbar), by utilising a conventional heater. This is a crucial step for the emitter sleeve (in the case of LaB_6 emitters) as these impurities can result in poisoning of the emitter. The emitter follows the same process, though is conducted independently to the sleeve, to ensure the impurities do not poison the emitter. In addition, when the emitter is vacuum baked, the temperature is slowly raised to remove any excess water vapour at low temperatures, to ensure it is not poisoned during this process. Goebel [113] has found that despite manufacturer guarantees of LaB_6 purity, the emitter baking reduced the emitter mass by 1.4% in 6 hours, with over 50% of that mass reduction occurring in the first 2 hours. Once the procedure is completed the system is reconstructed and ready for main commissioning and operation.

2) **Cold outgassing:** The HHC system is constructed and installed in the required experimental configuration. After the last stage, the HHC has been exposed to atmosphere and thus must undergo the main conditioning. This conditioning must be done each time the cathode is exposed to atmosphere or low vacuum. The cathode is put to high vacuum ($<1*10^{-7}$ mbar) to start cold outgassing. This occurs for a sustained period of time, >2 hour to allow the chamber

pressure to reduce below $1*10^{-6}$ mbar, though preferably overnight to reduce the partial pressures of oxygen and water vapour within the HHC.

3) **Initial heating:** After outgassing, gas is then injected into the cathode, as with conventional ignition. Though the current is limited by the keeper supply, to a very small current <50 mA. The potential is then applied between emitter and keeper, which results in the formation of the Townsend discharge. This discharge transitions into a secondary emission sustained discharge which heats the emitter predominantly through ion bombardment.

4) **Increasing heating:** The keeper discharge power is slowly levelled up, by increasing the current limit. This slowly heats the emitter and cathode. Optionally, in-between each power level the discharge is switched off and the gas flow stopped, such that the system outgasses in high vacuum, at the higher temperature. The discharge power is typically applied for one hour, re-baking the cathode, such that it is ready for main operation.

5) **Completion**: To stop the conditioning procedure, the keeper supply is turned off, and then the gas supply is stopped. Alternatively, the system can be fully ignited following the ignition procedure.

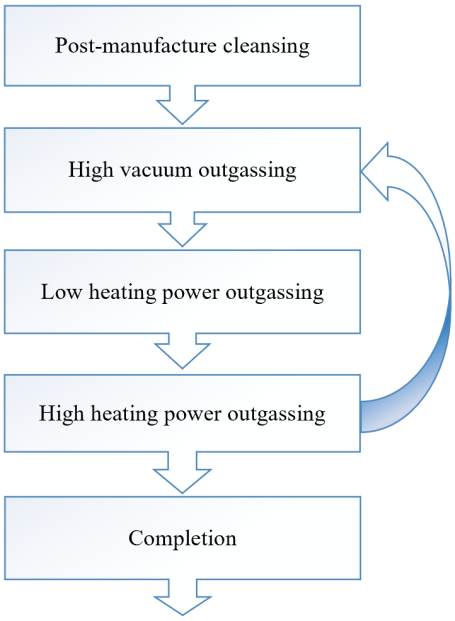

Figure 4.10: Overview of heaterless conditioning procedure.

The procedure set-out for commissioning of the HHC has been conducted various times, both in the nominal and backfilled configuration. Outgassing is dependent on both the pressure and temperature [114], and as HHCs require some pressure to begin self-baking, through ion bombardment, the outgassing rate is less than that of conventional HCs that bake in high vacuum, >1000 °C at $<1*10^{-6}$ mbar. With heating and quick evacuation of the HHC temperatures close to 500 °C at $<5*10^{-5}$ mbar have been reached, though the temperature reduces rapidly within minutes. Despite the clear disparity in the outgassing conditions for the HHC in comparison to conventional HCs, no issues of emitter poisoning were detected over the course of the operational tests, indicating the procedure is sufficient for purpose. This procedure has been successful for a LaB_6 emitter which is significantly more resistant to poisoning than BaO-W emitters, that can require propellant purities two orders of magnitude higher [39]. Such that if a BaO-W emitter were to be utilised further conditioning procedures may be required.

4.6.2 MAIN IGNITION PROCEDURE

Once the HHC has been conditioned in vacuum, or if the HHC has remained in vacuum since last operation, the following procedure is applied to fully ignite the cathode:

1. The gas flow is injected into the HHC at the required flow rate, or until sufficient pressure is reached if in the backfilled configuration. The gas commonly used is xenon, though tests are also conducted with alternative noble gases and mixtures, see Section 4.3.
2. After flow stabilisation occurs within ~30 seconds, the keeper power supply is set to a keeper potential, typically 500-700 V, and the nominal current required, typically 1-5 A. The supply output is then applied between the emitter and keeper. The following phases then occur with no user input:
    a. As initially there is no current flow, the keeper supply is in voltage control mode, and the voltage rises at the supply's maximum slew rate of 500 V/s, until the formation of the Townsend discharge occurs.
    b. After which a low current, ~50-300 mA discharge forms with a discharge voltage of ~250-400 V, sustained by secondary electron emission. The discharge heats the emitter predominantly through ion bombardment. During this stage the supply remains passively in voltage control as the remaining voltage drop is across the ignition control system.
    c. Once the emitter temperature reaches thermionic levels, the discharge transitions to a low voltage, ~30 V, higher current, $\geq$1 A discharge, which is now sustained via thermionically emitted electrons; this is the nominal discharge mechanism for the emitter. It was found that heating times were typically in the order of ~50 s

to raise the emitter temperature to the thermionic levels and start passively transitioning into this thermionic mode, though this is dependent on the keeper supply voltage limit and ICS resistance profile parameters. In this phase the HHC is in nominal keeper discharge operation, and the keeper supply has transitioned into current control mode, due to the discharge voltage drop and current rise to the supply's set limit.

3. If testing is conducted in the anode configuration, the anode supply is set to the maximum potential of 200 V and the current limit is set to the required value, typically >1 A, and the supply output is then applied, the voltage rises at the supply's maximum slew rate of 250 V/s, until the anode discharge forms, extracting a portion of the discharge current to the anode.
4. After a short period of stabilisation, ~1-3 minutes, the keeper discharge can be switched off, and the keeper potential is left floating. The HHC is now in nominal anode discharge operation.
5. Finally, to extinguish the HHC in either operational mode, the active power supply is turned off and then the gas flow is stopped. It is preferential to turn off the power supply prior to the gas flow, so that arcing does not occur as the pressure drops. The thermistors can require time to cool-down to regain their resistance before attempting re-ignition, this was found to be ~>15 minutes. In the nominal anode discharge, this thermistor cool-down can occur while the keeper discharge is off, such that there can be seamless re-ignition, as long as the anode discharge has been active for ~>15 minutes, with no keeper current.

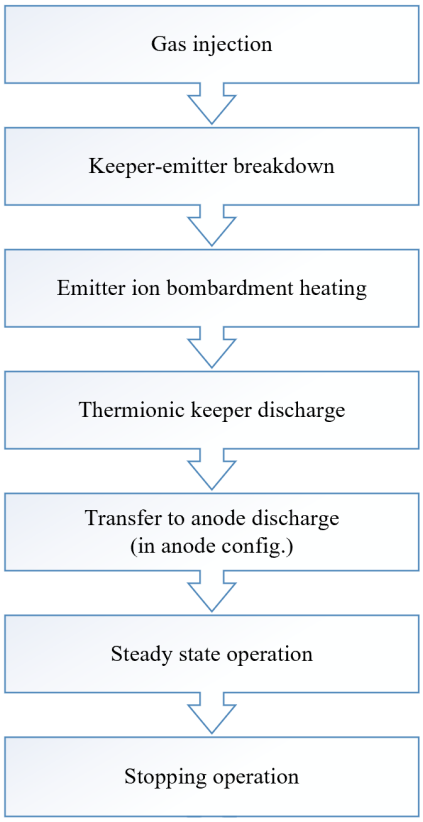

Figure 4.11: Overview of HHC ignition procedure.

CHAPTER 5

HEATERLESS HOLLOW CATHODE SYSTEM

5.1 INTRODUCTION

In order to investigate heaterless ignition, the construction of an HHC system was required to enable investigation into the electrical and mechanical sizing influence. As mentioned in the literature review (Chapter 2), there were several shortcomings with the current state-of-the-art HHCs, such as insufficient current and discharge attachment control, which would not allow reliable operation to high currents, in line with the research objectives (Section 1.5). Thus, a separate approach from that of the current HHC systems is taken, looking also at the more fundamental plasma breakdown-glow-arc transitions and characteristics (as described in Chapter 3) in order to achieve these overall heaterless ignition objectives. This approach was combined with the background of modern conventional HC designs in order to support favourable performances and lifetimes of the HHC in comparison to modern HCs. Furthermore, multiple prototype HHCs were constructed and tested to support understanding of the HHC physics prior to arriving at the main design methodology. This chapter is a detailed description of that design methodology of the novel UoS-HHC, which has a patent filed with application number 1807683.6 [2].

5.2 HEATERLESS HOLLOW CATHODE DESIGN

5.2.1 SYSTEM OVERVIEW

An overview of the UoS LaB_6 heaterless hollow cathode is shown in Figure 5.1. The heaterless hollow cathode consists of a stainless-steel mounting flange, which attaches to the vacuum

chamber mounts via mounting bolts that are electrically isolated with ceramic alumina corner washers. The cathode propellant line protrudes from the rear of the mounting flange, and connects to a 1/8-inch Swagelok fitting, with a ceramic isolator upstream, that connects to the main propellant line of the chamber. A molybdenum cathode tube 70 mm in length with a 4.9 mm inner diameter is secured to the mounting flange. The lanthanum hexaboride emitter with an inner diameter of 2 mm, outer diameter of 4.5 mm, and a length of 20 mm is inserted into the end of the molybdenum cathode tube. A fine graphite sleeve is used to electrically connect, yet mechanically separate the LaB_6 emitter from the refractory tube, due to the known issues of boron diffusion [23]. An insulating casing supports the multi-layered molybdenum thermal shield wrapped around the cathode tube, which reduces the radiative thermal losses of the HHC during operation.

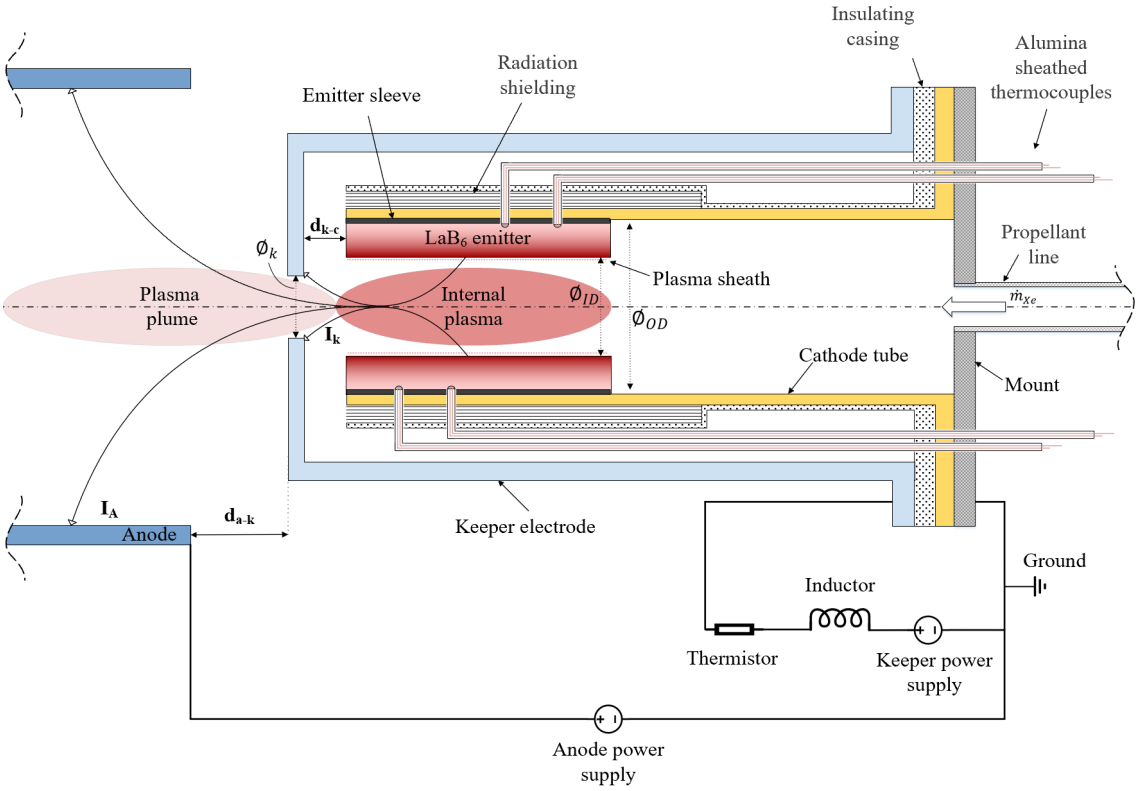

Figure 5.1: UoS LaB_6 heaterless hollow cathode, with thermocouple instrumentation and simplified electrical scheme.

The HHC utilises a reduced keeper orifice and open emitter, which is one of the most common heaterless attributes (see Table 2.1). This attribute is combined with two critical novel adaptations to allow repeatable ignition to high current operation, in a more power efficient and potentially less erosive manner. Firstly, dielectric barriers are placed over the non-emitting cathode tube exterior, so that the discharge power is directed to the emitter, reducing the power losses during ignition and increasing stability. Secondly, the electrical supplies have auxiliary current control

measures to stabilise and maintain a uniform diffusive heating discharge, as well as stopping a large inrush current during the ignition initiation that can be erosive. This current control minimises the waste power through ignition, by reducing its resistance passively while current rises and the discharge stabilises. The following sections discuss the design methodology and critically the parameter influences and final selections that arrived at this novel UoS-HHC system, covering both the mechanical and electrical design aspects. This also includes tests conducted on initial prototype HHCs that supported this design effort.

5.2.2 EMITTER SELECTION

The emitter material is a main design consideration of any thermionic in-space cathode, as such a careful trade-off must be conducted for the given propulsion system requirements, based on the emission current density, operating temperature, lifetime, handling, and heritage. The current density J, in $\mathrm{A/cm^2}$, produced from thermionic emission of a material is predicted by the Richardson–Laue–Dushman equation [13, 115]:

$$J = AT^2 e^{-\frac{e\emptyset_o}{k_b T}}, \tag{5.1}$$

where T is temperature in K, $\emptyset_o$ is the classical work function, e is electron charge, k_b is Boltzmann's constant, and A is the Richardson's constant, ideally $120 \frac{\mathrm{A}}{\mathrm{cm^2}}\ \mathrm{K^2}$. Though the Richardson's constant has been found to experimentally differ with material variation and temperature due to thermal expansion of the atom lattice. To take account of this, a simple material specific correction factor, B is implemented to form the corrected Richardson's constant [116],

$$D = BA \tag{5.2}$$

in addition, to take account of the temperature variations [116],

$$\emptyset = \emptyset_o + \alpha T \tag{5.3}$$

where $\emptyset$ is the temperature dependent work function, and α is an experimentally found constant. Thus, substituting Equation (5.2) & (5.3) into (5.1) gives:

$$J = Ae^{-\frac{e\alpha}{k_b}} T^2 e^{-\frac{e\emptyset_o}{k_b T}} = DT^2\, e^{-\frac{e\emptyset_0}{k_b T}} \tag{5.4}$$

Finally taking account of the Schottky effect [117, 118], where the electric field causes reduction to the cathode surface barrier, effectively decreasing the work function, gives:

$$J = DT^2 \exp\left(-\frac{e\emptyset_o}{k_b T}\right) \exp\left(\frac{e}{k_b T}\sqrt{\frac{eE}{4\pi\epsilon_0}}\right) \tag{5.5}$$

where ϵ_0 is the vacuum permittivity, and E is the electric field at the cathode surface.

For pure thermionic emission at high emission densities the Richardson equation does not correlate to the collected current. This is due to the space charge limit described by Child in 1911 [119]. Where electrons which are emitted from the cathode surface inherently create a space charge, with high enough emission this limits the subsequent emission of current. The Child-Langmuir law gives an empirical relation of the space charge influence, providing a more representative thermionic emission current in the space charge limited range. So space charge limited current density J_{Cl}, in A/cm^2 is given by [13, 119]:

$$J_{Cl} = \frac{4\epsilon_0}{9}\sqrt{\frac{2e}{M_e}}\frac{V_a^{3/2}}{d^2} \tag{5.6}$$

where M_e is the electron mass, V_a is the anode voltage, in V, and d is the cathode-anode separation, in cm. Due to this space charge limit, in-space HCs typically utilise neutral gas injection, which is ionised in the formed thermionic discharge. The generated ionic current allows the discharge to surpass the space charge limit, allowing high extraction currents, up to 300 A has been demonstrated [120].

A comparison of emission current densities for various material is shown in Figure 5.2. It can be seen that the recently developed 12CaO*7Al2O3 (C12A7:e^-) emitters which has an often quoted theoretical work function of 0.6 eV [53, 121], has the highest emission density for a given temperature. This 0.6 eV work function was first reported by Kim [122] in 2006, which was from a current density extraction of 12 $\mu A * cm^{-2}$. This reporting led to a significant research effort by multiple groups [53, 121, 123-126] into experimentally employing C12A7:e^- emitters within in-space HCs. Unfortunately, this tiny work function has never been realised for sizable current extraction, with Kim's own group reporting a 2.1 eV work function in the field enhanced regime at higher current densities [127]. Furthermore, there are additional issues with the use of C12A7:e^- emitters for >1 A operation, firstly, the internal resistance of the calcium aluminate is known to be high, though not well characterised, and this is coupled with the material's low melting temperature of ~1000 ℃. This inevitably resulted in multiple failed cathode tests in which the emitter melted [125, 128], due to the ohmic heating of the emitter. Potential use of C12A7:e^-

emitters in very low current (<100 mA) applications may be suitable, if reliable work function measurements demonstrate better performance than LaB_6 and BaO-W emitters for appreciable current densities, as researchers are currently working on [121]. For higher current operation to be feasible, fundamental material alterations to reduce the resistivity are required. Hence for applications such as high power HHCs it is not currently suitable. Also shown in Figure 5.2, is the BaO-Scandate emitter which has been produced with a work function of 1.5–1.7 eV [129], though use of such emitters is challenging due to lack of emission uniformity and poor stability [130].

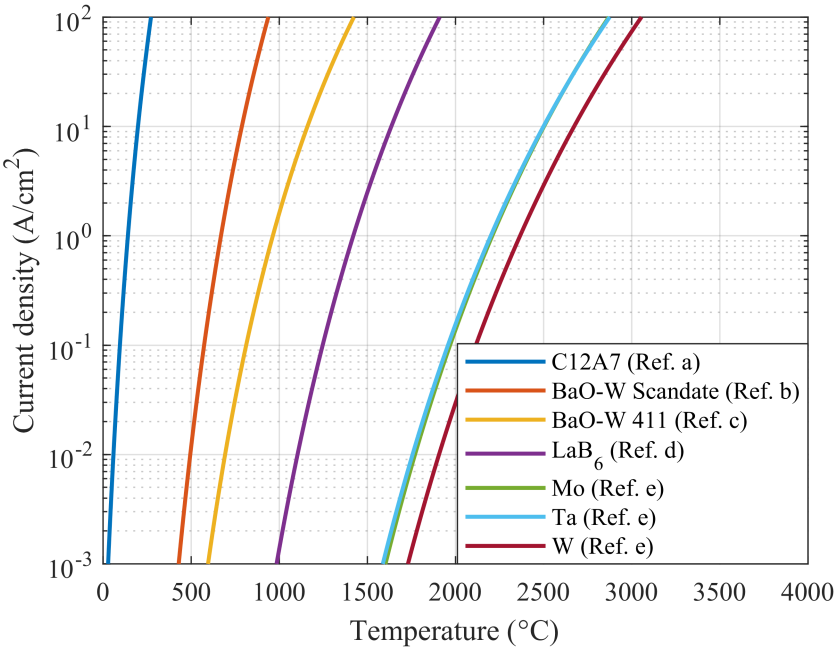

Figure 5.2: Thermionic current density emission for various materials, Ref. a [122, 125], Ref. b [131], Ref. c [118], Ref. d [132], Ref. e [133].

The refractory metals; Mo, Ta and W, all require high temperatures in excess of 2000 °C to produce reasonable emission current density's due to the high work functions, ~4.1-4.55 eV [116]. Lower work functions are possible with barium oxide layers deposited onto a porous tungsten matrix which can lower the work function of tungsten below 2 eV [118]. The material matrix is typically made up of a 4:1:1 mix thus referred to as BaO-W 411, though other mixtures have been used [92]. Lanthanum hexaboride (LaB_6), which is a refractory ceramic have relatively low work functions, reportedly between 2.6-2.9 eV [132, 134, 135], such that emissions greater than 10 A/cm^2 are possible at 1650 °C.

Thermionic cathodes for in-space propulsion typically employ LaB_6 or BaO-W emitters due to their relatively low work function, allowing thermionic emission with small input powers. This is coupled with both material's good stability, known material properties and flight heritage.

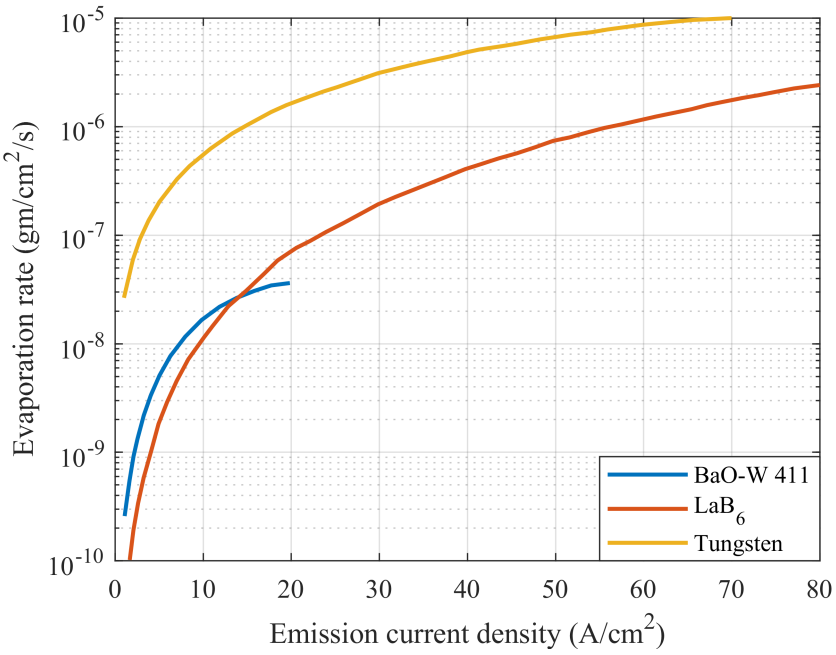

Figure 5.3: Evaporation rate as a function of emission current density [46]

The evaporation rate of the emitter material is critical in determining the cathode lifetime. Figure 5.3 shows the evaporation rate as a function of emission current density for a few materials. Tungsten can be seen to have a high evaporation rate, this is due to the higher temperature required to produce equivalent emission current densities, thus significantly limiting lifetime. LaB_6 evaporation rates are over an order of magnitude lower than that of tungsten, and lower than BaO-W for up to 15 A/cm^2. BaO-W typically can only operate up to 20 A/cm^2 due to excessive evaporation of barium. Whereas LaB_6 emits from the bulk material, hence LaB_6 lifetimes are higher for a given mass [46].

As well as the heater issues discussed before in Chapter 1, emitter poisoning is a cause of HC failure. Some emitters require careful handling, such as vacuum storage, to ensure poisoning does not occur. Poisoning especially arises with BaO layered emitters, as the addition of contaminants can cause reactions with the delicate surface chemistry increasing the work function. BaO-W emitters require xenon purities in excess of 99.9995% which adds costs to operation [46]. In contrast LaB_6 emitters are not reliant on their surface chemistry for their low work function, thus can be handled relatively easily, utilising propellant purities two orders of magnitude less [23]. Though there are emission reductions with carbon contamination, which can occur easily if

carbon is used within the HC system, vacuum baking can significantly restore the LaB_6 material properties if carbon contamination does occur [136].

Another consideration of emitter choice on ignition is that BaO-W when heated evaporates and redeposits on the outer orifice surface, essentially lowering the work function of the outer cathode orifice edges, this allows for conventional ignition with relatively small orifices. However, LaB_6 does not undergo this redepositing mechanism when heated, thus ignition is difficult with small orifices. For HHC ignition, independent of emitter material, there is no deposition on the orifice edges due to the emitter not being heated prior to the potentials applied. Though after a period of ignition cycles this might occur for BaO-W emitter HHCs.

The USA has predominantly operated BaO-W emitters in their modern cathodes, this is due to the lower heater requirements and interface simplicity in comparison to LaB_6 emitters. Though with the increasing demand for higher power HCs and the subsequent emission requirements, significant research has been conducted recently into LaB_6 [23, 39]. Russia had early adoption of LaB_6 emitters and is commonly used on their spacecraft since the 1970s [137]. A comparison of the widely used LaB_6 and BaO-W emitters is shown in Table 5.1.

Table 5.1: Trade-off overview for LaB_6 and BaO-W emitters

Attribute	LaB_6	BaO-W
Handling and poisoning	• Requires relatively low propellant purity (99.95% pure) • Emission from bulk material • Relatively resistant to handling and impurities • Cannot be in direct contact with refractory metals during operation	• Requires high propellant purity (99.9995% pure) • Emission reliant on surface chemistry • Heavily impacted by any impurities or contamination during handling
Emitter temperature for an emission density of $10\ A/cm^2$	$\sim 1650\ °C$	$\sim 1250\ °C$
Evaporation rates for an emission density of $10\ A/cm^2$	$\sim 1.1 * 10^{-8}$ gm/cm^2/s	$\sim 1.7 * 10^{-8}$ gm/cm^2/s
Lifetime for a 3.8 mm ID and 6 mm OD emitter with 10 A nominal emission.	~350 khrs [39]	~65 khrs [39]

This trade-off gives an insight into the main properties of the emitters, overall it can be seen that the power class of the cathode have a large bearing on the cathode material selection. With lower-mid power class (< ~20 A) the LaB_6 heater and operational power requirements are too demanding due to the higher work function than BaO-W. Whereas at higher currents (>~30 A) the LaB_6 handling and lifetime characteristics outweigh the increased thermal engineering requirements. Though specific mission or laboratory testing requirements can heavily sway this overview trade-off. For heaterless systems, a variety of emitters has been used (as was shown in Table 2.2), including tantalum [30], BaO-W [27] and LaB_6 [35]. Predominately BaO-W has been used, as most HHCs developed have been for low power designs so far.

The UoS-HHC investigation entails the cathode undergoing several parameter sweeps and diagnostic tests, such that an emitter which is robust and can be easily handled is preferred. In addition, the motivation for high power (≥30 A) HHCs will require high emission currents. Both these requirements strongly support the LaB_6 emitter option, despite the higher thermionic emission temperatures required.

5.2.3 EMITTER SIZING

Emitters have been sized to produce the operational current requirements with 0D models [138], though predominately this is just to support the numerous empirical studies [27, 30, 39, 49, 139]. The emitter surface area has a relatively small sensitivity on total emission compared with the temperature, as can be seen in Figure 5.2 for LaB_6 an approximate order of magnitude emission density increase per 150 ℃ from 1000 to 1600 ℃. Though the temperature is linked to lifetime [44], due to the evaporation of the material, it is beneficial to have a low temperature in that respect, but this must be countered against having a reasonably sized emitter which in turn sizes the cathode for use in the propulsion system.

The emitter requirements for the HHC emitter are to operate with a current density below 20 A/cm^2 in accordance with other authors [26, 39], due to the aforementioned lifetime issues and to operate up to 20 A emission with the aim of future scaling to >30A in line with the research motivation. As this is a proof of concept HHC, having flight level lifetimes (>10000 hrs) is not of concern yet, though the lifetime should be enough for adequate parametric testing and characterisation, with a reasonable margin, thus at least >1000 hrs.

To reach a current density below 20 A/cm^2 while producing a total emission of 20 A the emitter area must be ≥ 1 cm^2. Hence the HHC LaB_6 emitter has an inner diameter of 2 mm with an outer diameter of 4.5 mm, and a length of 15 mm, which are comparable dimensions to established cathodes with similar current operation, such as the T6 which has operated up to 30 A [33, 140]. The emitter ID and length determine the emitting surface area. Such that the HHC emitter, can

produce a 20 A nominal discharge, when operating at 1685 ℃, with a corresponding current density of 15.84 A/cm^2, if assumed to be uniform emission. The OD in relation to the other parameters determines the overall mass of the emitter, in this case this corresponds to a mass of 1.2 g.

The lifetime of the cathode is dependent on the emitter lifetime, which can be calculated [39, 132] by the evaporation of the emitter material which is influenced by the material temperature. The evaporation rate as a function of given current density, E_J, is shown in Figure 5.3, and for LaB_6 at 20 A/cm^2 this corresponds to $6.87{*}10^{-8}$ g/cm^2/s. Assuming uniform emission across the emitter, the emitter lifetime for a given emission current, I, can be estimated using the following method:

The emitter surface area, S_A, volume, S_V, and current density, J, are respectively,

$$S_A = \pi * S_{ID} * S_L, \qquad S_V = \pi * S_L * \left[\left(\frac{S_{OD}}{2}\right)^2 - \left(\frac{S_{ID}}{2}\right)^2\right], \qquad J = I/S_A \tag{5.7}$$

where S_{ID}, S_{OD} and S_L, are the emitter ID, OD and length respectively, in cm. The emitter evaporation rate, E_S, in g/s is given by

$$E_S = S_A * E_J \tag{5.8}$$

and the emitter mass, in g, is

$$m_e = \psi_e \, \rho_e * S_V \tag{5.9}$$

where ρ_e is the emitter density, for LaB_6 this is taken to be 4.72 g/cm^3, and ψ_e is the emitter relative density ratio taken to be 0.9. Hence the estimated emitter lifetime, L_e, in seconds is

$$L_e = m_e/E_S \tag{5.10}$$

The lifetime is taken to be until 90% of the emitter volume is evaporated and as the typical ion bombardment in the emitter region in cathodes is <20 V [39], sputtering can be neglected. Figure 5.4 shows the HHC lifetime as a function of emission current based on the emitter dimensions shown in Table 5.2. This model does not account for any temperature variations along the emitter

axis, which can reduce the lifetime, or for material redeposition along the surface that can increase lifetime. Thus, this model provides an order of magnitude estimate for the emitter lifetime to aid the emitter sizing.

The model iteratively calculates the lifetime, at 0.1% volume intervals, due to the S_{ID} increasing with evaporation over time, which increases S_A and thus reduces E_S, which therefore increases lifetime. This evaporation rate decrease through the operational lifetime for the HHC can be seen in Figure 5.5 for various operational currents. For higher current operation, the evaporation magnitude is higher, causing a quicker increase in S_A, such that there is faster reduction in the evaporation rate.

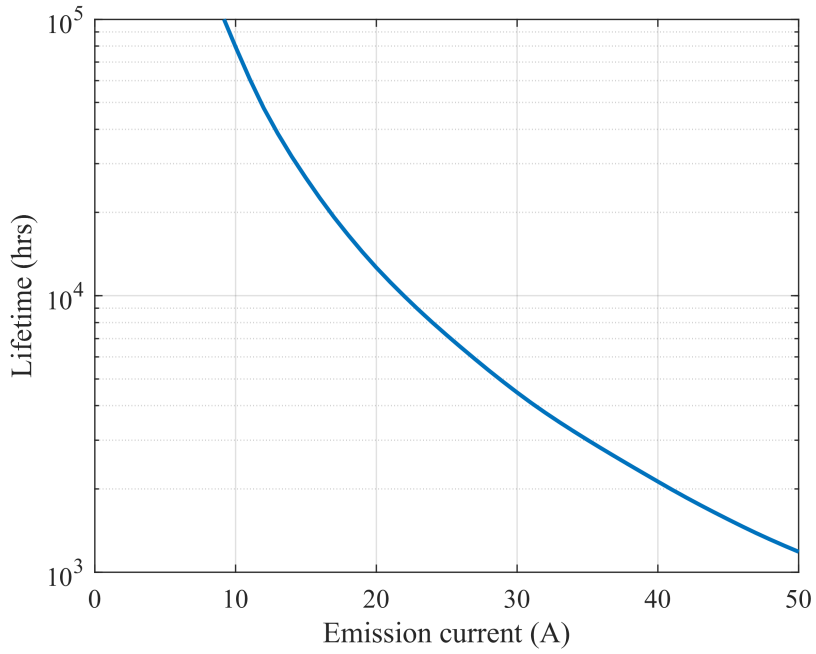

Figure 5.4: Lifetime estimate for the HHC as a function of emission current.

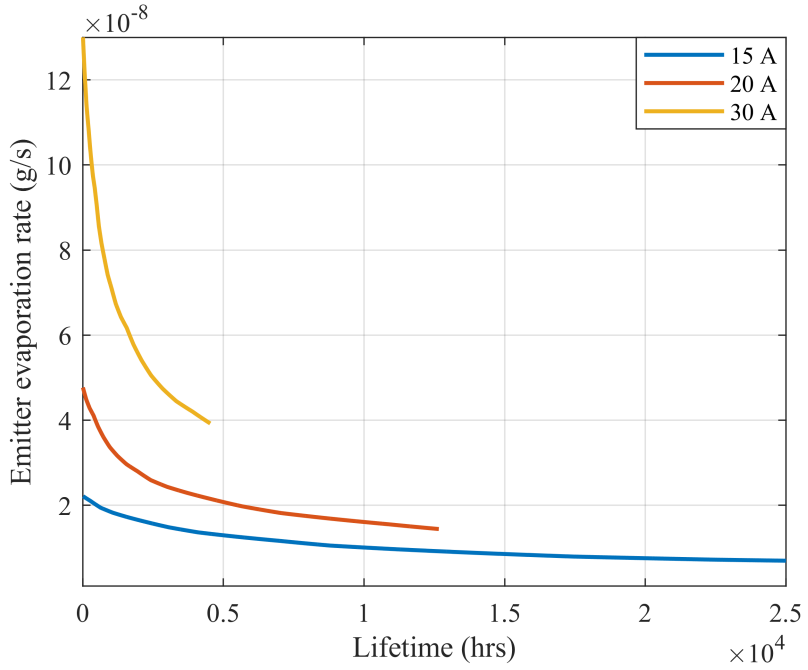

Figure 5.5: HHC emitter evaporation rate over lifetime for various emission currents.

Figure 5.4 shows that for the HHC nominal operation at 20 A the lifetime is over 12,000 hours, significantly surpassing any lifetime requirements for this proof of concept HHC. However, for flight models or for operation toward 50 A and higher, the emitter, and thus cathode, would require resizing, as it is estimated to have a life of just over 1000 hours at 50 A. The UoS-HHC emitter details are summarised in Figure 5.2.

Table 5.2: Summary of UoS-HHC emitter characteristics

Characteristic	Value
ID (cm)	0.2
OD (cm)	0.45
L (cm)	2
Nominal operating current (A)	20
Nominal emission density (A/cm^2)	15.84
Nominal operating temperature (°C)	1685
Lifetime under nominal conditions (hrs)	12640

5.2.4 EMITTER INTERFACE

Lanthanum hexaboride cannot be in direct contact with most refractory metals when heated due to boron diffusion. Lafferty in his original paper on the discovery of LaB_6 [132], described this process as the boron atoms diffusing into the refractory metal lattices, taking up positions in the interstices and forming interstitial boron alloys with them. The boron diffusion continues, with the boron frame work which holds the alkaline-earth or rare-earth atoms collapsing, permitting the latter to evaporate. This lasts until all the interstices of the base metal are filled with boron or until all the boron from the hexaboride is used up.

This has been shown on LaB_6 coated tungsten wires which operated with high emission for mere 48 hours before ceasing to emit, furthermore the wire became swollen and very brittle crumbling on inspection [132]. Hence most researchers have placed carbon [132, 141, 142], rhenium [143] or tantalum carbide [132] material interfaces between the refractory holder and LaB_6.

Due to the similar expansion coefficients of POCO carbon with LaB_6 and the successful employment of such carbon sleeves in conventional cathodes [23], it was employed for the HHC. The issue with the fine grain sleeve approach is that it requires a good concentric fit on the outer layer in contact with the tube and inner layer with the emitter, to provide good electrical and thermal contact through ignition.

To simplify this interface attempts were initially made with 0.1-0.5 mm Grafoil which was layered around the emitter, before inserting the emitter into the cathode tube. Although implementation of this method was achieved, the Grafoil would commonly tear, and non-uniformly cover the emitter when being inserted into the cathode tube. The main issue is the non-repeatability of such a method. Thus, the fine grain solid sleeve approach was implemented for the emitter interface. The sleeve is manufactured with the same ID and OD of the emitter OD and tube ID respectively, then sanded down to allow a contact fit. Carbon can have impurities that can poison the emitter, to counter this the sleeve must be high vacuum baked for >1 hour at >1500 °C at $<1*10^{-5}$ mbar to ensure these impurities are outgassed, before use in the HHC. The precise sensitivities of this conditioning procedure for the sleeve are not well published, though this approach has yielded satisfactory results empirically.

5.2.5 THERMAL CONSIDERATIONS

A critical aspect of the HHC system is the thermal design, as the core operation of these in-space cathodes is thermionic emission, good thermal design enables reduced power consumption. Furthermore, this can increase lifetime, as a smaller heat flux is required to sustain the emitter temperature, such that there is reduced ion bombardment and/or reduced energy of the

bombarding ions, thus decreasing the sputtering erosion. For HHCs this additionally can mean quicker transition to the thermionic discharge from the secondary emission sustained discharge.

To allow a suitable thermal design of the cathode a simplified thermal model was created, utilising commercially available Multiphysics software. The model has been used to investigate the influence of many parameters such as HHC length, cathode thickness, cathode material, number of radiation shield layers, and radiation shield length, which are discussed in the following sections within this chapter.

Typically, HC thermal models are validated using the known heating power from the internal heater, though as the HHC has an unknown heat flux, such validation is challenging. However, this model can still give clear insight into the sensitivity of design parameters. Additionally, this aids the material selection for the given components by understanding their required operational temperatures.

The model is a 2D axis-symmetric steady state thermal model, produced using COMSOL 5.4, which solves Fourier's law of heat conduction,

$$\vec{q} = -k\nabla T \tag{5.11}$$

where $\vec{q}$ is the local heat flux density, k is the thermal conductivity, and ∇T is the temperature gradient. The radiative heat loss is solved through the Stefan-Boltzmann equation,

$$j_s = \varepsilon\sigma T^4 \tag{5.12}$$

where j_s is the energy per time per area, ε is the material emissivity of the grey body, and σ is the Stefan–Boltzmann constant.

The model geometry is the same as that of the HHC, see Figure 5.6, with the HHC connected to the MACOR mounting supports of the VC3 vacuum chamber system, shown in Figure 4.4. Though as the model is 2D axis-symmetric, and the mounting supports are not axis-symmetric, they are modelled by reducing the diameter of the support, such that the model has the equivalent surface area contact and conduction. The mount surface area is far greater in the model, by ~10 times larger, such that the emissivity requires correcting,

$$\varepsilon_{eff} = \varepsilon \frac{S_{real}}{S_{mod}} \tag{5.13}$$

where ε_{eff} is the effective emissivity, S_{real} is the real surface area and S_{mod} is the model surface area. This correction helps the emissivity issue, though there is increased self-emission due to the axis-symmetry, which is a limitation of the model. Though in this HHC model this self-emission is quantitatively negligible given the temperature of the MACOR supports being under 500 °C in most cases.

The material contacts were assumed ideal and a thermal heat source boundary condition was placed on the emitter surface, assuming a uniform heating profile. At the far end of the MACOR supports to the chamber, a room temperature boundary condition is applied.

A separate meshing domain is used for the radiation shielding for which the geometry of each layer is 25 mm by 0.025 mm with 25 layers around the cathode tube. The layers are indented to reduce the thermal contact from one layer to another, and the small cross-sectional area reduces thermal conduction along the shield length. The model simplifies the coiled radiation shield to concentric layers which do not conductively connect, with equally spaced positioning along the casing to cathode tube gap. The shield area is meshed independently to the rest of the geometry due to the thin sheets.

As mentioned, although the model is not experimentally validated, such that the absolute values may be off ~200 $°C$, the model still allows for a sensitivity analysis of the HHC parameters, an example is shown in Figure 5.6, which clearly shows the increased conduction losses when decreasing the length to width aspect ratio of the HHC.

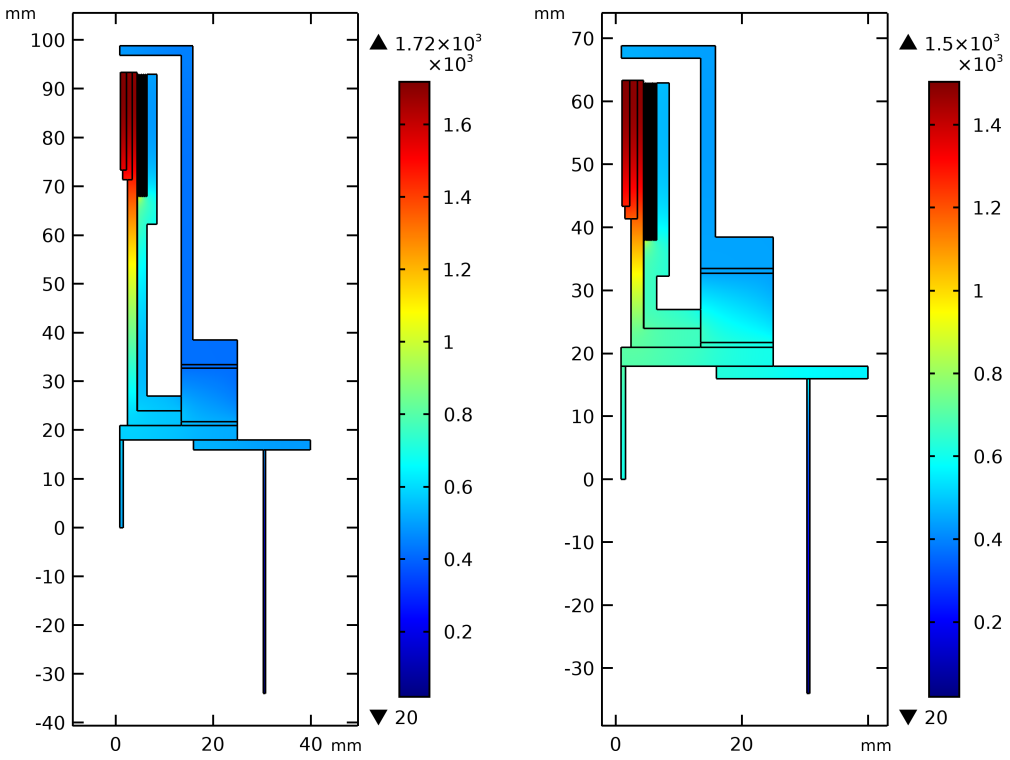

Figure 5.6: 2D axis-symmetric thermal simulation of the HHC with an emitter heating power of 150 W, nominal (left) and 30 mm shorter configuration (right), in °C.

5.2.6 CATHODE TUBE MATERIAL

The cathode tube mechanically supports the emitter, while also providing an electrical connection. The cathode material must have high mechanical strength to endure satellite launches, be conductive and must withstand the operating temperatures of the emitter (>1600 °C). Such material property requirements, limits the selection to that of the high temperature metals, commonly referred to as *refractory metals*. Additional to these core requirements, a key performance parameter of the cathode tube material is the thermal conductivity, as that influences the conductive losses through the tube. Thus, to assess these material selection implications on the thermal design, the thermal model discussed in Section 5.2.5 is utilised.

It can be seen in Figure 5.7 that there is significant practical influence on the emitter temperature with different cathode tube materials, with the emitter being 500 °C higher for MoRe45% cathode tube compared with W, for an emitter input power of 100 W.

The properties of typically used cathode materials can be seen in Table 5.3, Ta, Re and MoRe45% can be seen to have the lowest thermal conductivity of the refractory metals. Tantalum has heritage for use with BaO-W emitters in the QinetiQ T6 cathode [19], though the lowest thermal

conductivity is for Mo-Re, which also has good heritage in several NASA cathodes [144]. NASA has also attempted construction of a 1 mm thick POCO carbon cathode tube [39], to allow direct contact with a LaB_6 emitter, though soon reverted to a Mo-Re tube [23, 141], likely due to not being able to withstand the structural issues from launch shock/vibrations, in addition to the arcing issues with using a carbon cathode orifice.

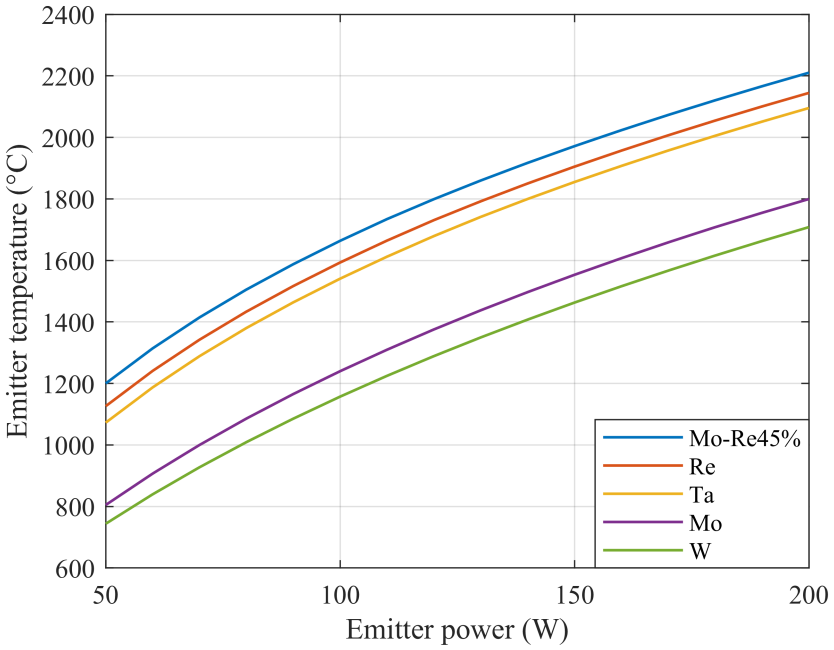

Figure 5.7: Thermal simulation of the cathode tube material influence on emitter temperature as a function of emitter heat flux power.

Another critical consideration is the cathode material's ability to be re-heated multiple times. MoRe has an increased recrystallization temperature and reduced grain size than pure Mo, as well as significantly greater tensile strength and a greater creep strength at high temperatures. Mo thermal conductivity decreases with increasing rhenium percentage up to 50 % while thermal expansion increases [145]. In addition, rhenium is more resilient to boron diffusion at high temperatures than other refractory metals [146], and Mo is more resistant than tantalum to oxidation [147, 148], indicating Re rich Mo will be more inert at high temperatures [145, 148-151].

Table 5.3: Material properties of refractory metals

Property	Ta	Mo	Re	W	MoRe47.5%
Thermal conductivity (W/ m K)	57.5	138	48.0	173	36.8
Density (kg/m3)	16690	10280	21020	19250	13500
Thermal expansion (µm/m K)	6.3	4.8	6.2	4.5	5.72 (500 °C) 6.45 (1000 °C)
Melting point (°C)	3017	2623	3186	3422	2450
Young's modulus, (GPa)	186	329	463	411	365
Shear modulus, (GPa)	69	126	178	161	132

MoRe45% can be clearly determined to have the best, thermal, structural and chemically inert properties combined with a strong heritage, which is very important given the general lack of depth in refractory material characterization for extended thermal cycling and operation beyond 1000 °C. These benefits come with an associated cost, with MoRe45% and pure Re being around 20 to 30 times the cost of pure Mo. The purpose of this UoS-HHC is to provide proof of concept of this novel system's operation, while allowing further investigation of heaterless ignition. Hence an appropriate substitute for MoRe45% and pure Re given the cost, is Mo, due to the better resilience to recrystallisation compared with Ta despite the thermal conductivity performance drop. Though for future HHC engineering and flight models MoRe45% would be the preferred choice.

5.2.7 CATHODE TUBE SIZING

The cathode tube sizing is important to minimize the thermal losses through the cathode, while yet insuring a sufficient mechanical and thermal connection. The model discussed in Section 5.2.5 is utilised to investigate this sizing influence on thermal performance. The tube ID is determined by the emitter, with additional clearance for the emitter sleeves. The OD is minimized to reduce thermal loss; this can result in a sub-millimetre tube thickness. Figure 5.8 displays the cathode thickness influence and as can be seen, sub-millimetre thickness decreases have increasing gains in power efficiency, due to the increased reduction in cross-sectional area. However, for this proof of concept model, a 2 mm thick tube is constructed to ensure structural integrity for the multiple parameter changes. Additionally, the tube is made with a high length to diameter aspect ratio, to

further reduce thermal losses, this effect is shown in Figure 5.9. There are high thermal losses when the tube length decreases below 70 mm, and thus the cathode flange to tip length is 70 mm long with an inner diameter of ~5 mm to support the emitter.

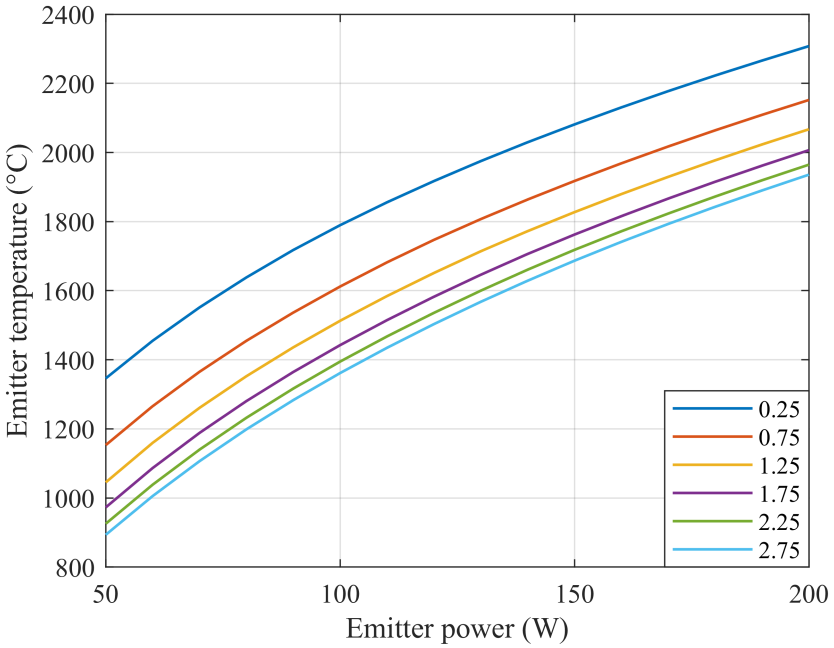

Figure 5.8: Thermal simulation of the cathode tube thickness (in mm) influence on emitter temperature as a function of emitter heat flux power.

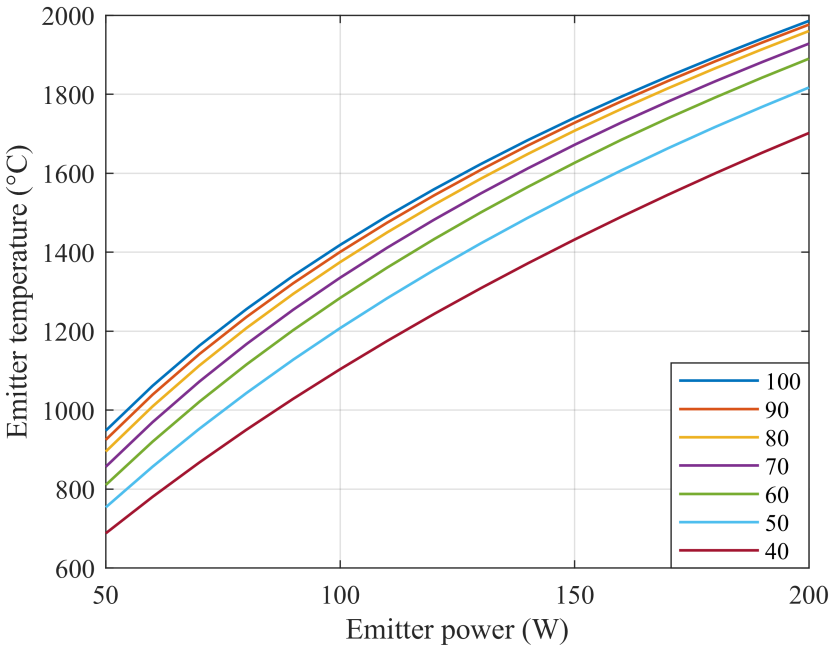

Figure 5.9: Thermal simulation of the cathode tube length (in mm) influence on emitter temperature as a function of emitter heat flux power.

5.2.8 ORIFICE MATERIAL

In conventional cathodes, the cathode orifice influences the internal pressure and protects the emitter from excess sputtering. Material choice of the cathode orifice is segregated from the cathode tube due to the sputtering yield requirement of the orifice. Molybdenum which is often used for cathode tubes, has a sputter yield over one order of magnitude higher than alternative materials at 30 eV ion energy, as shown in Figure 5.10. Molybdenum was initially used by developers for the orifice, as with the keeper, though are now moving to alternative orifice materials due to the high erosion experienced. It is often stated that the sputtering yield of carbon is superior to that of refractory metals [39], though the published sputter yield data (see Figure 5.10), appears to suggest that they are very comparable at 50 eV especially given the uncertainty in the data. At higher ion energies it may be lower, though these energies are not applicable to cathode operation. Tantalum appears to have the lowest sputter yield, with tungsten and POCO marginally higher at 50 eV, though due to the mentioned tantalum embrittlement and recrystallization issues from thermal cycling this material is not suitable for the orifice use with LaB_6. POCO has had reported arcing issues when utilized as the cathode orifice [152], and similar effects have been found in our initial testing when utilizing carbon orifices. Tungsten which also has a low sputtering yield compared with Mo has been found to operate well [31] and not to suffer from these recrystallization afflictions. As such tungsten is increasingly been utilised for orifice construction, in particular sintered tungsten has been found to give good performance.

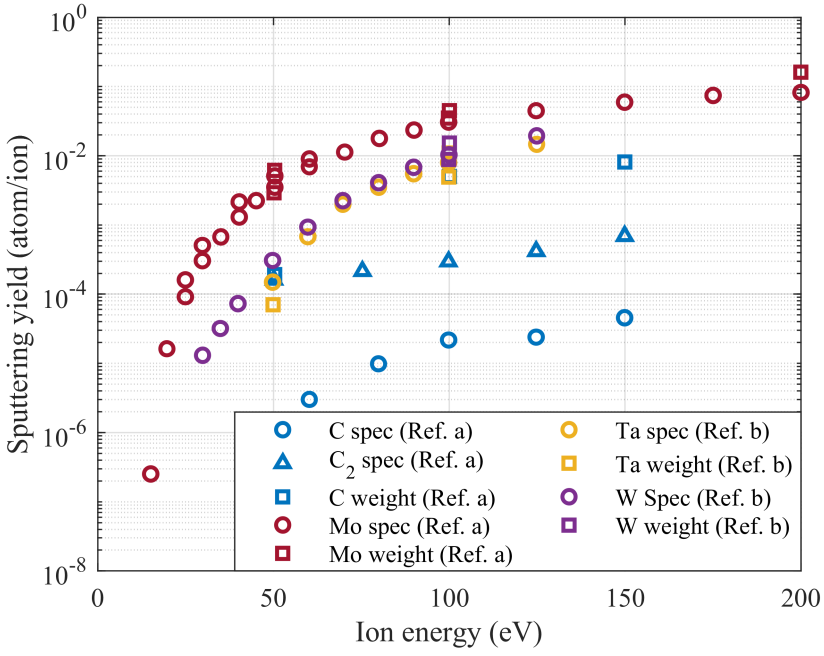

Figure 5.10: Sputtering yield as a function of xenon ion energy for various materials via spectrographic and weight loss measurements, Ref. a [153], Ref. b [154], uncertainties are typically ± 40%.

5.2.9 ORIFICE SIZING

For conventional cathodes the orifice sizing has been described in Section 2.2.3, showing the orifice ID influence on the internal pressure and plasma density. For HHCs commonly the pressure is determined by a constrictive keeper orifice, to allow higher cathode-keeper pressures in order to achieve a cold breakdown voltage <1 kV. Thus, the keeper orifice is of higher importance for HHCs. Furthermore, as discussed in Section 2.2.1, commonly HHC developers have opted for an uncovered emitter, such that there is no cathode orifice, this is to allow direct heating of the emitter during ignition.

Additionally, it is often reported that LaB_6 [141] has a low sputter rate compared with that of refractory metals, due to data presented [143] showing LaB_6 to sputter 2.5 times less then tungsten, though no information is relayed as to the experimental conditions, such as ion energy and ion type. Thus, it is challenging with the data available, to accurately determine the LaB_6 sputter yields in the conditions applicable to in-space cathodes.

Due to the heritage with HHC operation without a cathode orifice and the potentially low LaB_6 sputter yield, no orifice was adopted for this HHC. However, with testing it became apparent that the lack of a cathode orifice had undesired effects; the discharge visually appeared to attach to the emitter outer surface as well as the inner emitter surface. This attachment profile may cause a thermal shift toward the emitter front edge, caused by a higher electric field at the edges inducing higher bombardment, which can increase non-uniform emission. In addition, due to the discharge forming on the outer cathode surface edge, it does not utilise the HC effect which minimises erosion. It would therefore be beneficial in future models to utilise a non-constrictive tungsten orifice, so that there is a high work function downstream surface to the emitter to reduce discharge attachment in nominal operation, and thus help to reduce emitter sputtering and more uniformly wear the emitter.

5.2.10 KEEPER MATERIAL

Most recent keeper research [155-157] has focused on the erosion due to high energy ion bombardment of the keeper surface. The evidence of the severity of this erosion can be clearly seen in Figure 5.11, where after 30,352 hours of operation the molybdenum keeper end was completely eroded. This level of erosion was much more severe than originally predicted due to ion energies been measured significantly higher than that of the discharge voltages [158, 159].

A leading theory of the cause of these high energies is that it is a result of ion acoustic instabilities [160]. It has been measured that the erosion on the keeper is maximum almost halfway along the keeper [156, 161], with a wear rate of 70 um/khr for the NSTAR [155].

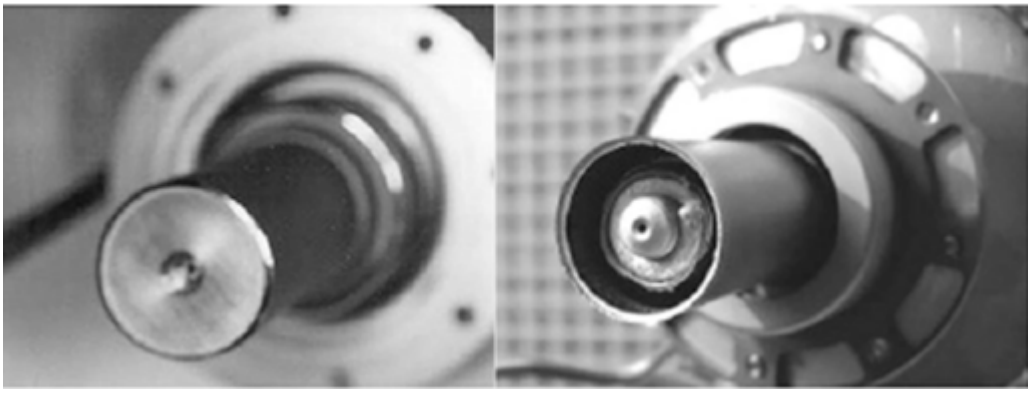

Figure 5.11: NSTAR keeper erosion, shown new (left) and after 30352 hours operation (right) [46].

Developers have undertaken several design changes due to this phenomenon, such as changing keeper material from molybdenum to graphite, due to the enhanced sputter yields (see Figure 5.10). In addition, for the ultra-high-power class cathodes (>100 A), additional gas injection external to the cathode tube has been used to mitigate the high erosion. Gallimore [161] first employed gas injection through the cathode-keeper gap, with the gas ejected from additional holes in the keeper to counter the high energy ion bombardment. To the same effect Goebel [162] introduced external gas injection outside the keeper and in the cathode-keeper gap. Goebel also found this approach minimised total propellant usage in such dual flow arrangements.

Even though graphite orifices were found to induce arcing, this has not been reported for the graphite keeper electrodes. Also as mentioned, the sputter data suggests that tantalum (see Figure 5.10), may be marginally better for a keeper material, but given the extensive heritage that graphite has received from the T6 and NEXT lifetime testing, means that the POCO graphite keeper is the tried and tested solution to the NSTAR erosion issue. Though it is critical to note that these studies are focused on solving conventional HC keeper issues, and for HHCs the keeper life limiting factors are not known, though it can be reasonable to assume that the material sputter yield will be a critical property of the HHC keeper electrode. Thus, for the HHC a fine grain EDM-3 POCO graphite keeper was chosen due to the conventional HC heritage and low sputter yield in comparison to molybdenum.

5.2.11 KEEPER SIZING

With the HHC system there is a reduced keeper orifice, such that the keeper forms the constrictive orifice choking flow, increasing the pressure between the emitter and the keeper. As discussed in Section 2.2.3, this allows for ignition with nominal flow rates (<15 sccm) throughout the ignition process, without requiring gas pulsing or bypass. Moreover it allows a significantly lower breakdown voltage from the kilovolts used in heaterless ignition of conventional cathodes [27], to around 300-350 V, due to igniting near the Paschen minimum. Though notably this is higher

than the ~80 volts used when igniting conventionally heated LaB_6 cathodes [163], due to the lack of thermionically emitted electrons when cold starting.

The cathode pressure is predominantly dependent on the constrictive orifice size and mass flow rate. As the keeper orifice is the most constrictive orifice in the flow stream in this HHC, Goebel's commonly used internal cathode pressure equations [23, 46, 120, 164], that implement the Poiseuille law [165, 166] modified for compressible flow [167], can be used to calculate the keeper entrance pressure:

$$P_1 = \left(P_2^2 + \frac{0.78\dot{m}\xi T_r l_\emptyset}{{d_\emptyset}^4}\right)^{0.5}, \xi = 2.3 * 10^{-4} T_r^{0.71+\frac{0.29}{T_r}} \tag{5.14}$$

where P_1 is the upstream pressure in Torr, P_2 is the pressure downstream of the orifice in Torr, $d_\emptyset$ is the orifice diameter in cm, $l_\emptyset$ is the orifice length in cm, $T_r = \frac{T}{289.7}$, where T is temperature in K and finally $\dot{m}$ is mass flow rate in sccm. Goebel has found this to be accurate to around 10-20% of the actual measured pressures [46], though as the author explains the equation is not strictly valid in some HC locations, especially in the case of short orifices. Thus, by assuming the flow is choked at the keeper orifice, the choked flow mass flow rate equation [168] can also be calculated to determine the pressure at the keeper orifice entrance for comparison:

$$\dot{m} = \frac{pA_\emptyset}{\sqrt{T}}\sqrt{\frac{\gamma_c}{R_s}\left(\frac{2}{\gamma_c+1}\right)^{\frac{\gamma_c+1}{(\gamma_c-1)}}} \tag{5.15}$$

when rearranged it gives,

$$p = \left(\frac{A_\emptyset}{\dot{m}\sqrt{T}}\sqrt{\frac{\gamma_c}{R_s}\left(\frac{2}{\gamma_c+1}\right)^{\frac{\gamma_c+1}{(\gamma_c-1)}}}\right)^{-1} \tag{5.16}$$

where, $\dot{m}$ is mass flow rate in kg/s, A is the orifice cross-sectional area in m^2, γ_c is the heat capacity ratio, for Xe at 300 K it is taken to be 1.66, $Rs = R/n$, R_g is the gas constant, n is molar mass for xenon taken to be 131.29 $kg{\cdot}mol^{-1}$, T is the temperature at the orifice in K, and p is the pressure in Pa.

Figure 5.12 shows both Eq. (5.14) and Eq. (5.16) plotted, for varying mass flow rates. It can be seen that both equations have reasonable agreement around 10-20 sccm, though at lower flow rates, the choking condition may not be satisfied, or the validity issues of the Eq. (5.14) could be

causing the divergence from the correct pressure profile. A cathode of the HHCs intended power class would typically operate from around 10-20 sccm [120, 169], where both equations are in reasonable agreement.

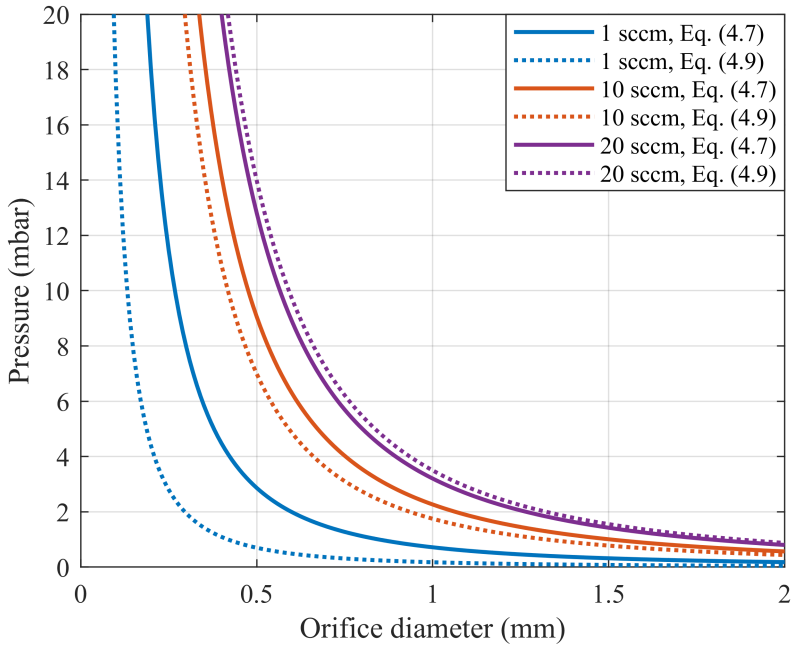

Figure 5.12: Keeper orifice size influence on pressure for varying $\dot{m}_{Xe}$, with T=300 K, l=1.5 mm,

As the keeper orifice diameter, $\emptyset_k$, is a critical consideration for the HHC design, it was experimentally investigated in the operational characterisation, and empirically found that a $\emptyset_k$ of 1.8 mm enabled current extraction of up to 30 A. This is interestingly comparable to that of the conventional BaO-W T6 cathode orifice diameter reported to be 1.6 mm with operation up to 30 A [50]. The thickness of the keeper orifice is set to 1.5 mm based on prior orifice thicknesses [89], though as this keeper acts effectively as both the cathode orifice and keeper orifice of a conventional cathode, the HHC keeper may encumber the combined erosion, and thus the thickness may require increasing for future engineering and flight models. The keeper tube ID is 26 mm, which is large enough to allow room for cathode instrumentation, with a thicker wall thickness than the orifice end, of 2.85 mm, this is to ensure structural integrity.

Another critical sizing parameter is the keeper-cathode separation, which influences the breakdown voltage and operational conditions, hence was also investigated in the operational characterisation, but is nominally set to 3.5 mm. This is slightly larger than conventional cathodes which for the T5, T6 and NSTAR are reported to range from 2.15-3 mm [33, 50, 89, 170], in order to increase pd, and thus aid the breakdown phase, the few HHCs that have reported this parameter have been from 0.76-6.35 mm (See Table 2.2).

5.2.12 RADIATION SHIELDING

To minimize thermal losses, and aid a quicker transition into the thermionic regime, multiple layers of thermal shielding are wrapped around the cathode tube (see Figure 5.1). Radiative shielding of cathodes, is a typical process [39]. Due to the high temperature nature of cathodes, typically used aluminium thermal shielding is not possible due to the relatively low melting temperature. Thus, for cathodes refractory tantalum or molybdenum foil shielding is utilised, due to their low emissivity of around 0.18 at 2000 K [171] and high melting temperatures. The HHC utilises molybdenum foil due to the cost, and the greater flexibility which allows easier wrapping than tantalum foil.

The effect of the number of thermal shield layers is assessed utilising the thermal model described in Section 5.2.5, and the results are shown in Figure 5.13. The first layer has the most significant power savings, with diminishing returns thereafter, which is due to the significantly lower emissivity of the Mo shielding compared with the casing, such that the first layer has the highest impact in insulating from radiative losses. After 15 to 25 layers, there can be seen to be very minimal performance gains, as the outer layers are relatively cold. The influence of the radiation shield length is seen in Figure 5.14. The longer the radiation shield the better the performance, though above 35 mm long, the shielding performance gains become increasingly marginal as the shielding is far from the heat source input.

Thus, to ensure good thermal insulation while accounting for material cost, 25 layers of 40 mm wide and 0.025 mm thick molybdenum foil was utilised for wrapping around the cathode tube. The foil was also dimpled to ensure layer to layer thermal contact was kept at a minimum.

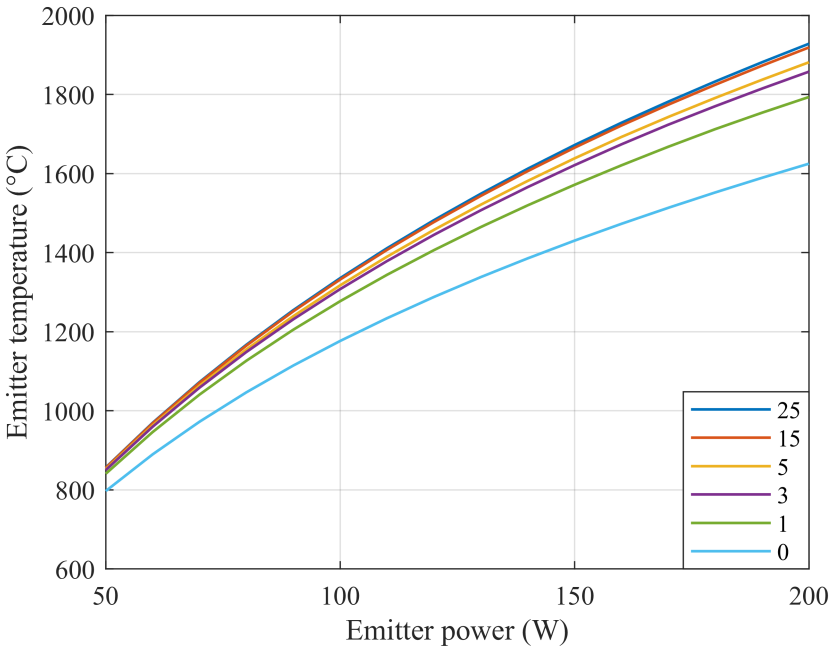

Figure 5.13: Thermal simulation of the radiation shield layering influence on emitter temperature as a function of emitter heat flux power.

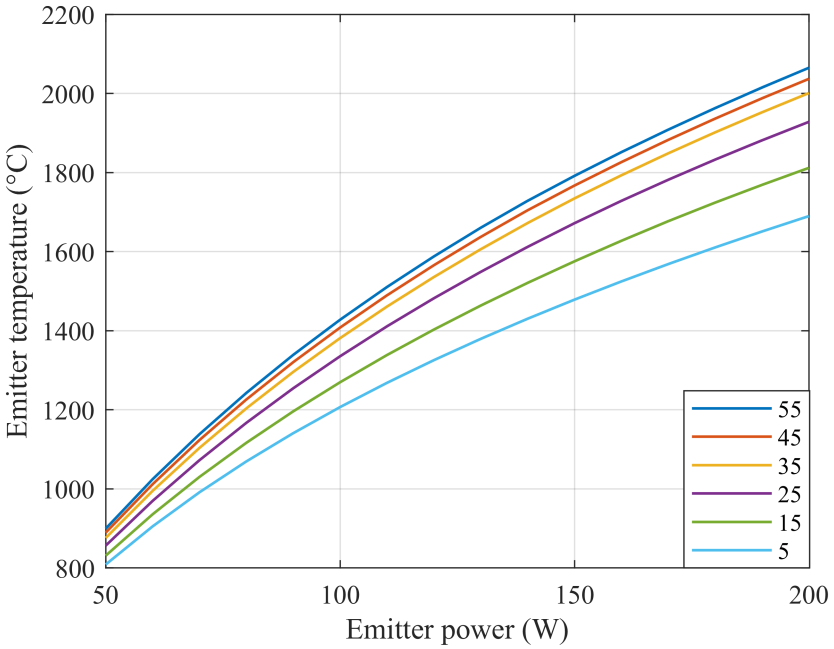

Figure 5.14: Thermal simulation of the radiation shield length (in mm) influence on emitter temperature as a function of emitter heat flux power.

5.2.13 INSULATING CASING

As discussed in Chapter 3, the heating phase in heaterless ignition is sustained via secondary electron emission, as the emitter temperature is below the temperatures required for sizable thermionic emission. Hence during this phase, the discharge is not naturally limited to the low work function emitter and can attach over most of the cathode, as has been mentioned in Section 3.3.3. With initial prototype HHC testing this effect became apparent. As the current increases the discharge would clearly attach to almost the entire conductive surface at cathode potential, in order to increase the secondary emission and thus sustain the increased current.

Figure 5.15 shows a heating stage secondary electron emission sustained discharge, in a 5 mbar Ar backfilled environment with a 100 mA keeper discharge limit. As can be seen, the discharge has spread across the whole cathode tube and mount. Discharge attachment spreading to the whole cathode tube and radiation shield results in reduced heating efficiency, as the heating power of the discharge spreads over a large surface area. In such cases the ignition can be challenging as parts of the HHC, such as the stainless-steel mount, can potentially melt prior to the emitter reaching thermionic temperatures for transition to the nominal arc discharge.

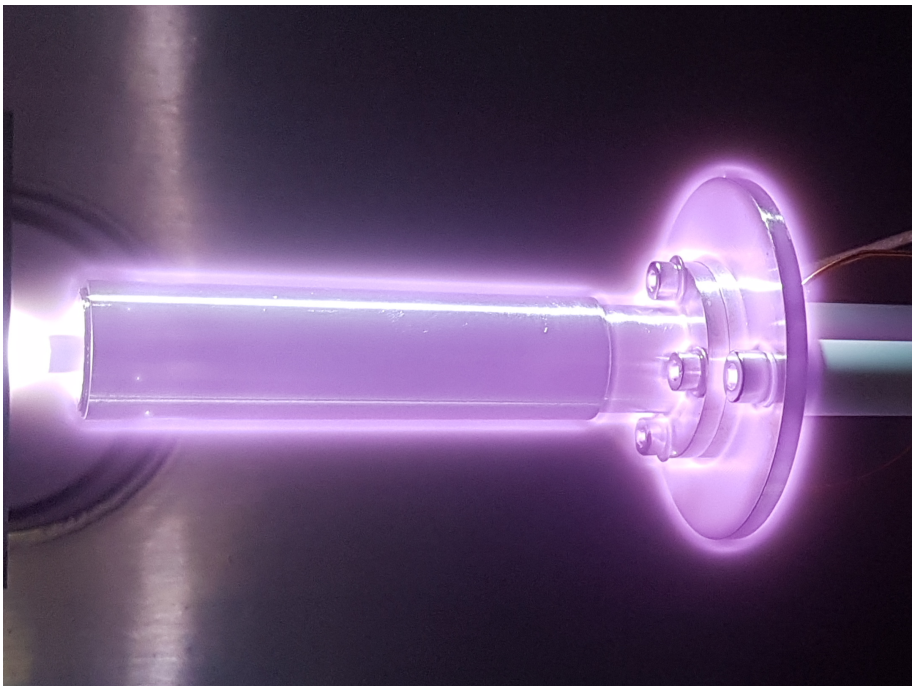

Figure 5.15: Initial HHC protype test with a 100 mA, 5 mbar (Ar) backfilled keeper discharge.

This issue has resulted in other authors [38] utilising very quick transitions to the thermionic discharge, by just heating a localised area, though this may be more erosive, due to the resulting non-uniform ion bombardment. Alternative to this approach, a novel system was constructed to supress parts of the diffusive discharge attachment and control the heat flux input through the

heating phase. This is achieved through the use of a non-conductive sleeve placed on the exterior of the cathode tube (see Figure 5.1), which causes the discharge attachment to reside inside the hollow cathode and not on the exterior.

As was discussed in Section 3.3.3, the glow discharge extinguishes when the anode-cathode separation becomes less than the cathode fall thickness, the normal glow cathode fall thickness has been reported to be ~0.31 Torr ∗ cm for Ar [28]. Such that with this HHC system with a typical 1-8 mbar pressure during the heating phase, the cathode fall thickness can be estimated to be 4-0.5 mm. Hence, to ensure the glow discharge does not form over the cathode, the non-conductive sleeve is placed with a concentric separation <0.25 mm from the cathode tube surface, significantly less than the estimated cathode fall thickness. This controlled plasma attachment enhances the heat flux input and supports a stable transfer to a thermionic discharge. The outer sleeve also acts as a support for the radiation shielding as shown in Figure 5.1.

5.2.14 ELECTRICAL SYSTEM

HHCs have suffered heavy erosion and melting during start-up operation, as discussed in Chapter 2, this is due to the process of *hard starts* in which electrical surges occur during the breakdown and heating phases, where uncontrolled high current pulses lead to vaporization of the electrodes. Additionally, the *soft starts* attempted by using ballast resistors resulted in unacceptable power losses for high current HHC applications. To mitigate these issues, a novel type of soft start electrical ignition system was developed, which enables a controlled rise of current through ignition, suppressing electrical inrush surges while also stabilising the diffusive secondary electron emission sustained discharge by providing adequate current control.

The impact of the electrical discharge surge during breakdown is measured for an initial HHC prototype model in Figure 5.17. The power supply is set to 600 V with a 0.1 A current limit, with the cathode-keeper in an 8.5 mbar Ar, backfilled configuration with a 5 mm separation. The electrical breakdown occurred at ~500 V with an induced current peak of around 650 A within 40 μs. This high current discharge occurs due to the power supply capacitance, which in this case is 70 mF. During this discharge process, this power supply capacitance is charged to 500 V and discharged across the cathode-keeper gap during breakdown, where the resistance of the gap drops from an >1 MΩ measured resistance to under 1 Ω. This capacitance discharging at 500 V can release a total energy of 8.75 J within a mere 110 μs, which is equivalent of a mean power of 79.5 kW over that period. This significant power use can result in the discussed cathodic spots and vaporization of the electrodes.

Thus, the HHC electrical system is critical to preventing current surges through breakdown and stabilising the discharge to ensure it is stable and diffuse through ignition. To support the electrical

setup, a semiempirical model has been created utilising freeware software for electrical simulations. A good agreement between the produced model and the measured HHC current surge can be seen in Figure 5.17. This model allows for rough sizing and sensitivity analysis of the current control measures developed. The model created in LT Spice XVII is comprised of three main parts, the power supply, electrical controls, and plasma load. The model overview can be seen in Figure 5.16.

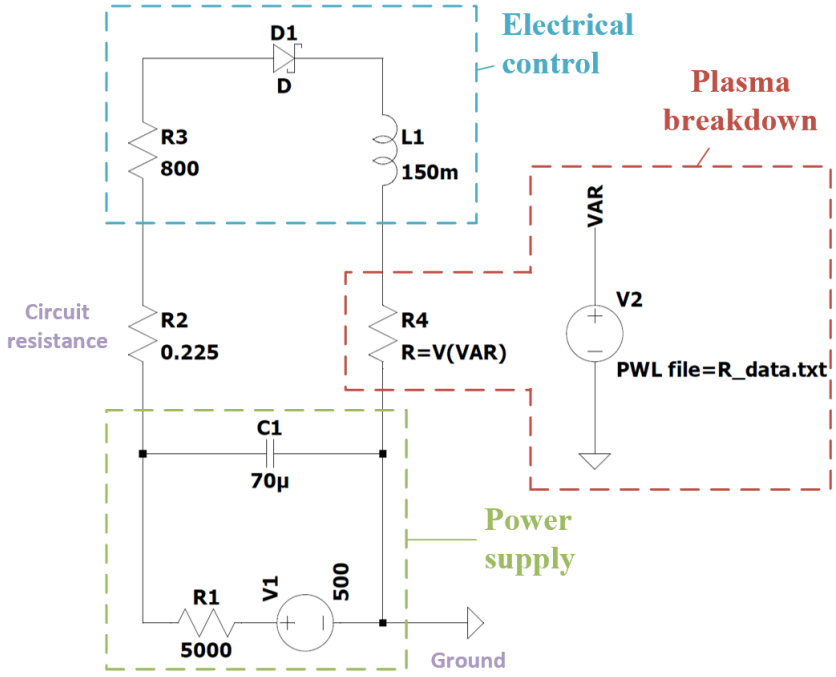

Figure 5.16: Electrical model of HHC breakdown.

The plasma load is modelled as a variable resistor, prior to the discharge breakdown the resistance is effectively infinite, which is modelled as a very high resistance of $1*10^{15}$ Ω, then when the gas electrical breakdown occurs, as the plasma has a negative differential resistance, the current increases and resistance decreases to less than 1 Ω in under a few μs.

Thus, to accurately model the breakdown, the model plasma resistance is taken from the experimental profile, see Figure 5.17. This is inputted into the model resistor from when breakdown occurs. Due to a program limitation a model work around is used to achieve this, in which the resistance profile is inputted into a voltage supply, V2, which in turn exports the empirical data as a local variable, VAR, which is than inputted into the plasma load, R4.

The empirical resistance profile is used throughout the parameter sweeps, though the electrical controls implemented will likely reduce the severity of the plasma resistance drop, as the plasma

resistance decreases with increasing current, such that inputting the same empirical profile may not be strictly valid. Nevertheless, this results in the model presuming the worst-case resistance profile, and therefore the electrical controls implemented are conservative.

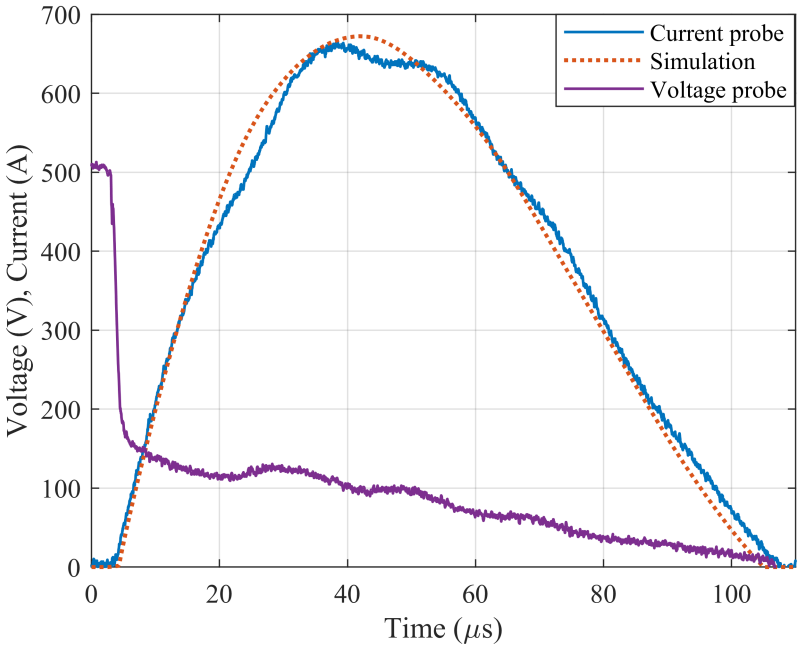

Figure 5.17: Electrical breakdown surge between the keeper and cathode with Ar backfilled configuration at 8.5 mbar, with a 4 mm separation and a power supply current limit of 0.1 A.

The power supply model, seen in Figure 5.16 shows the main characteristic of the power supply investigated, which is the capacitance discharging that occurs through breakdown. Therefore, the power supply is modelled as a voltage source with resistance, R1 that limits the current to 100 mA, as set in the experimentation, which acts as the current limiting function of the power supply, then a 70 μF capacitance is placed in parallel, which is the internal capacitance of the EA 750V-12 A keeper supply used. This capacitance is discharged, when breakdown occurs, and the result of the discharge across the breakdown is shown in Figure 5.17. Additionally, a resistance, R2, is set as 0.225 Ω, which is the circuit resistance, finally the power supply negative is tied to ground as in the experimental setup.

The ignition control system used consists of NTC thermistors, R3, inductors, L1, and a diode, D1, which combined passively limits maximum current while resisting changes in current and preventing possible reverse currents. The inductor and diode are directly modelled, and the NTC thermistor is simplified as a constant resistor due to lack of significant self-heating in the <1 ms of interest in the modelling.

The effect of the breakdown voltage on the discharge current is shown in Figure 5.18, which is due to the increased charging of the power supply capacitor, as $Q = CV$, where Q is the stored charge, in coulomb, C is the capacitance, in F, and V is the voltage, in V.

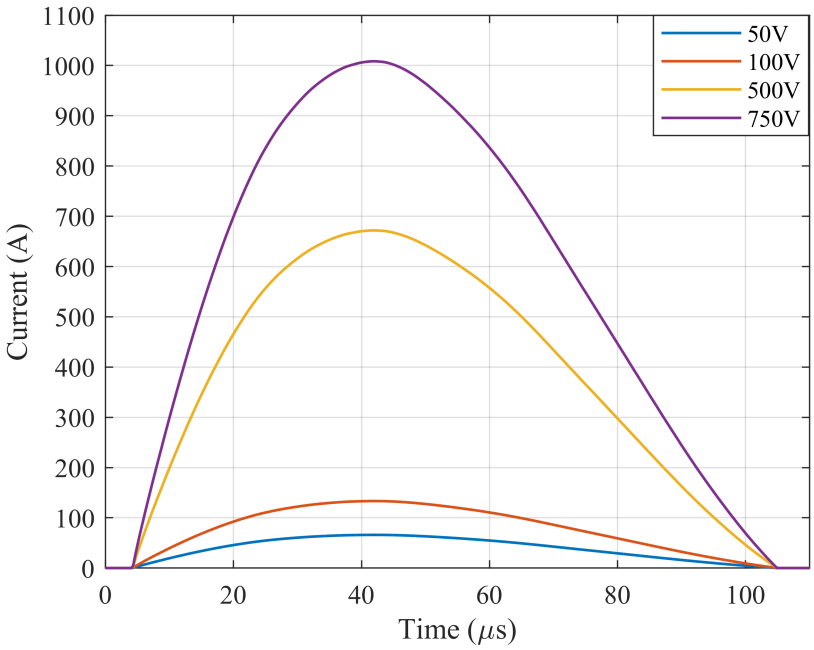

Figure 5.18: Electrical simulation of the breakdown voltage influence on the discharge surge.

This shows the high sensitivity to the breakdown voltage, clearly showing the benefit of igniting the HHC with a low breakdown voltage. For conventional cathodes that can ignite around 40-150 V [120, 163] the peak current could be around ~60-150 A. Though in such cases breakdown occurs with the emitter already thermionically emitting, such that it is possible the smaller current surges can be accommodated via semi-diffuse thermionic emission, reducing ignition erosion. Typically for conventional cathode testing electrical controls beyond the supply are not employed [42]. Whereas for heaterless ignition, due to both the different physical discharge mechanisms and higher ignition voltages, electrical controls should be implemented.

To aid in controlling the current rise of the heaterless hollow cathode, additional circuit resistance and inductance was employed. The influence of circuit resistance on the discharge surge is shown in Figure 5.19. The resistance can greatly limit the current surge, as $I = V/R$, though to limit the discharge to 100 mA, would require a 5 kΩ resistance. As mentioned, ballast resistance is not a desirable electrical component as it wastes energy, through ohmic heating. To reach nominal keeper discharge operation can require a current over 1 A, such that a 5 kΩ ballast would produce a wasted power of over 5 kW. As such, to minimise the power loss, an NTC thermistor is utilised, which passively reduces resistance as current increases. This provides the highest resistance for

the breakdown phase and passively reduces through the heating and arc phases. This allows the HHC to maintain a nominal keeper discharge with minimal control circuit power losses. The thermistor characteristics determine the resistance decrease as the thermistor temperature rises, which in turn determines the heating phase period. Hence, the thermistor characteristics can be tailored to minimise thermal shock by reducing the thermal gradients.

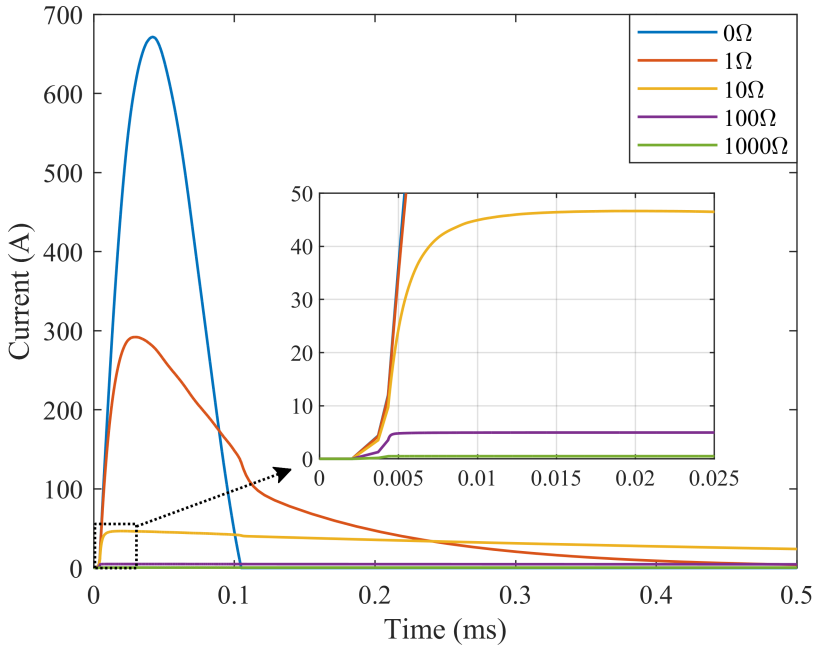

Figure 5.19: Electrical simulation of the resistance influence on the discharge surge.

In addition to controlling the in-rush current, the overall electrical system must provide adequate electrical resistance to sustain the diffusive discharge during the emitter heating phase, otherwise, it was found that the discharge can localise into arcing (prior to the emitter fully reaching thermionic temperatures) and thus cause high non-uniform erosion.

To support maintaining a stable discharge, the influence of additional circuit inductance was investigated, to slow the rate of current change. In Figure 5.20 a 100 mH inductor can be seen to reduce the current peak to ~12.5 A from around 650 A, though without a diode, which impedes reverse currents, this can result in reverse currents that will disrupt the discharge and damage the power supply electronics.

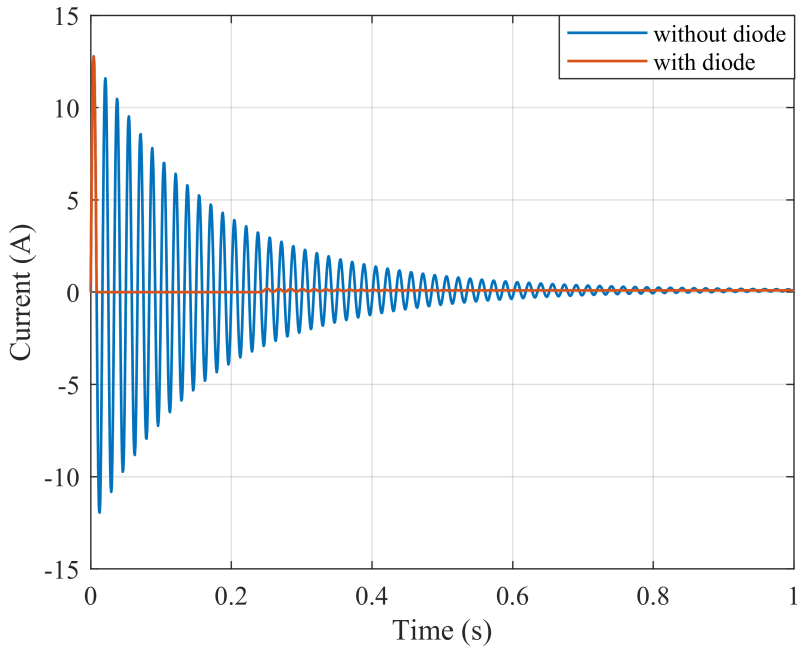

Figure 5.20: Electrical simulation of a 100 mH inductor on the discharge surge, with and without an in-series diode.

The sizing influence of the added inductor can be seen in Figure 5.21 with magnified subplots that use the same units as the main plot. As shown the rate of current increase and peak current are both reduced. However even a very large 1 H inductor only limits the peak current to around 4 A, well beyond the 100 mA set by the power supply. That said, the inductances slowed rate of change can greatly aid the stability of the discharge as it can reduce the severity of the resistance drop, which reduces the current peak, though such feedback is not considered in the electrical model. Additionally, if instabilities occur during the heating discharge, this inductance helps to prevent the change to an unstable state, by slowing any current change.

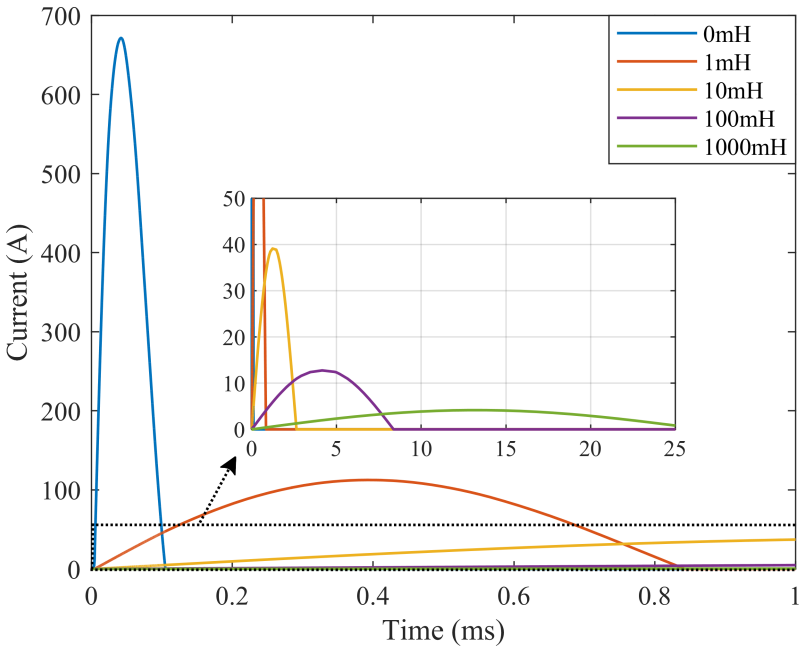

Figure 5.21: Electrical simulation of the inductance influence on the discharge surge.

Utilising this simulation led sensitivity analysis, an empirical test campaign found that discharge stability throughout ignition was greatly improved with an 800 Ω thermistor and a 150 mH inductor. This electrical control selection was also a trade-off of equipment cost and availability given that the electrical controls were also sized to allow steady state currents of up to 5 A during operation. A 150 mH inductor is still very large for in-space applications, especially an inductor rated for 8 A, which has wiring with a larger cross-section and thus increased overall size, though for this proof of concept HHC it allows greater flexibility in the maximum keeper current attainable, future designs can minimise this sub-component. The final electrical control setup utilised is shown in Figure 5.22 with magnified subplots that use the same units as the main plot. This shows that the current surge during ignition is significantly smaller, down to ~600 mA from the original 650 A, and reaches the peak in over 1 ms compared to the mere 40 μs. Furthermore, the model utilises the empirical resistance data of an uncontrolled breakdown surge. As such, the model provides a conservative estimate of the discharge surge with the implemented current controls, as the surge plasma resistance increases with decreasing current due to the negative differential resistance. This characteristic resistance profile is the reason the surge propagates and discharges the power supply capacitance.

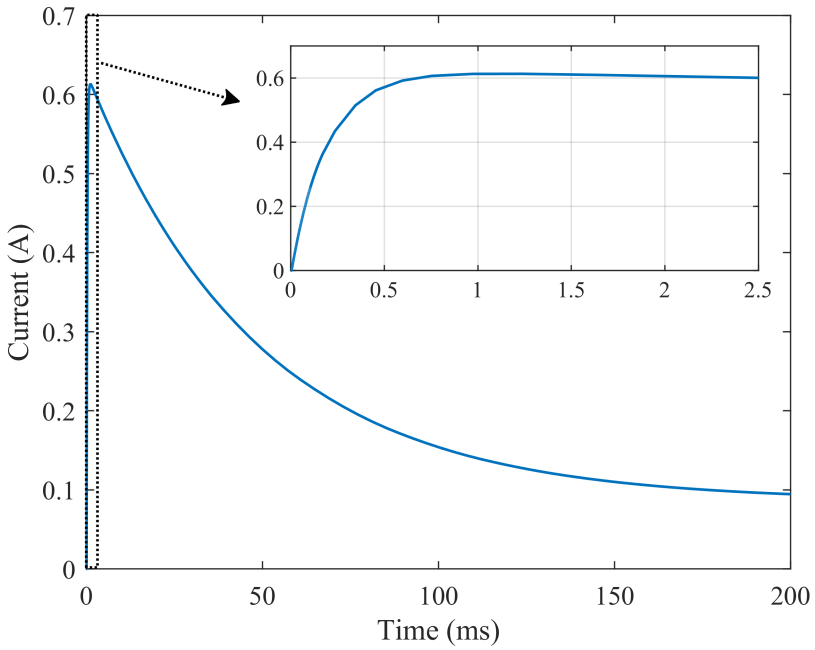

Figure 5.22: Electrical simulation of the combined 800 Ω resistance and 150 mH inductance influence on the discharge surge.

5.3 SUMMARY OF THE NOVEL HHC DESIGN METHODOLOGY

The design methodology to create a high current (>20 A) heaterless hollow cathode has been developed by assessing the main influences of all the critical subcomponents of the cathode, in relation to high current heaterless operation. Furthermore, the thermal and electrical influences to enable efficient high-power ignition are parametrically analysed. The trade-offs of the main influences assessed coupled with initial testing of several prototype models led to forming the novel soft heaterless ignition system. This system controls the discharge attachment and current through ignition, to efficiently and uniformly raise the emitter to thermionic temperatures. Thus, minimising erosion and thermal shock to the system to increase lifetime and performance. The summary of the design methodology is outlined below:

- The cathode emitter is critical to the system performance and lifetime, BaO-W and LaB_6 emitters allow long life and high-performance operation. The BaO-W emitters lower work function yields greater performance for low-mid power operation (<30 A), though the LaB_6 emitters high achieved current densities, coupled with good handling characteristics make them beneficial for operation beyond 30 A. However, individual mission requirements can skew such trade-offs. The LaB_6 emitter sized for the HHC has an estimated lifetime of several thousand hours and is sized to produce emission $\geq$ 20 A.

- The cathode tube that supports the emitter can significantly influence HC performance. Mo-Re45% has a strong heritage, and low thermal conductivity, though Ta or Mo can provide a low-cost substitute. A high length to width aspect ratio of the cathode tube can significantly increase power performance. Additionally, a smaller cathode wall thickness can be beneficial, though must be set to ensure structural integrity through operation.
- The keeper material has a high impact on lifetime, as was seen in the NSTAR lifetime test in which the Mo keeper was completely eroded. POCO carbon has been found to be a suitable alternative with the NEXT achieving a nearly 6-year lifetime test with such a keeper. The keepers in HHCs are typically constrictive to allow ignition with nominal flow rates with low breakdown voltages <500 V, and due to this no cathode orifice is required for operation. Though having a non-constrictive cathode orifice downstream of the emitter may benefit inducing discharge attachment inside the hollow emitter.
- Mo or Ta radiation shielding aids power efficiency, with the highest performance gain with the radiation shield covering the whole length of the cathode tube. Additionally, the first 5 layers of shielding give huge benefit, though there is a negligible difference with more than 25 layers.
- Implemented for the first time in an HHC, an insulating casing suppresses discharge attachment to the exterior of the cathode during the heating phase, this enhances the power input into the emitter, minimising power usage and erosion. This controlled glow discharge heating allows minimising of the thermal shock to the HHC.
- A novel HHC electrical system, consisting of a thermistor, diode and inductor is implemented to provide the required control of the current through ignition in a passive and low power usage manner. The system stabilises and maintains a uniform plasma discharge without current surges, while also working in parallel with the insulating casing to minimise thermal shock and erosion of the emitter during ignition. The design only utilises off-the-shelf components with two standard laboratory power supplies, thus allowing cost-effective incorporation of the heaterless hollow cathode apparatus into a given thruster or test system.

CHAPTER 6

OPERATIONAL CHARACTERIZATION

6.1 INTRODUCTION

The critical parameters of electron sources for in-space propulsion are the discharge current achievable, ignition and steady state power consumption, propellant usage and lifetime. These are the main performance benchmarks used to assess if an electron source is applicable for a given mission. As such, this chapter presents the UoS-HHC proof of concept and operational characterisation with emphasis of these performance parameters and their main influencers. To this effect, results are discussed for the breakdown, heating, transition and nominal keeper operation phases. This chapter also focuses on the influence of the novel ignition method employed in this HHC. Further discussion is based on the discharge attachment, internal pressure requirements, gas species influence, and the emitter thermal profile. Finally, the anode discharge operation is analysed in context to well established conventional HCs, with discussion on the HHC keeper orifice effect and initial keeper erosion observations.

6.2 BREAKDOWN PHASE

6.2.1 TOWNSEND DISCHARGE

The first stage of HHC ignition, in common with conventional HCs, is the breakdown stage. It is where a potential is applied to the keeper electrode in reference to the cathode, in a gaseous medium. This potential causes a cascading ionisation avalanche that ultimately results in the transformation to a conductive gaseous medium. Heaterless ignition does not have the supply of

electrons from a pre-heated thermionic emitter which enables conventional HCs to ignite with potentials as low as 50 V [163]. Thus, HHCs require a higher electric field strength to onset the ionisation avalanche.

As discussed in the breakdown theory, see Section 3.2.2, the breakdown voltage is a function of gas properties, the pressure-distance product, pd, and the cathode secondary electron coefficient, γ_{se}. To investigate the influences of pressure, gas species, and keeper-cathode separation, d_{c-k}, on the HHC breakdown voltage, the backfilled keeper discharge facility, see Section 4.4, was utilised. The backfilled keeper discharge setup has a static pressure profile and open keeper geometry compared to that of the main flow discharge setup (see Figure 4.3 & Figure 4.4). Such that there are differences between the open and enclosed system in terms of the pressure and flow profile, though the benefits of the quick parameter changes and visual verification of the breakdown allow a more significant sensitivity assessment of the parameters influencing HHC breakdown.

With classical Paschen curves, the experiment is conducted with parallel plates, and as these breakdown tests are conducted using the HHC, the geometry is more complex, as can be seen in Section 5.2.1. This has two main influences, firstly, the non-uniform electric fields, and secondly, the varying separation as the cathode and keeper electrode surfaces protrude away from each other (see Figure 4.3), such that d_{c-k} is the minimum distance between the electrode surfaces. Hence it is possible for the breakdown to strike anywhere along the length of the emitter, $l_e = 20\ mm$. Due to the complex geometry there are many possible breakdown paths, such that it is challenging to experimentally determine the exact breakdown path. Hence, this characterisation quantifies V_b for practical conditions on the HHC. Though the actual breakdown paths are of interest to assess controllability of where the breakdowns occur, this could be achieved by varying pd through adjustment of the mass flow rate applied. Such that the breakdown path may potentially be varied throughout the operational life of the HHC, in order to spread the breakdown erosion across the emitter, or alternately, to set the breakdown path to a non-active section of the cathode.

The breakdown testing was conducted by pre-setting the keeper supply voltage to 700 V and applying the output between the emitter and keeper which was increased at the supply's slew rate of 500 V/s, with the current limit on the supply set to 10 mA. When breakdowns occur, the voltage drop triggers the oscilloscope, and the corresponding *V-I* trace is recorded to the PC, with post-processing determining the breakdown voltage. This breakdown testing is conducted at various d_{c-k} set points, from 0.5 mm to 2 mm, in 0.5 mm intervals. This is repeated for various pressures around 5 mbar with krypton, argon and xenon. As breakdown is stochastic in nature, each set point is automatically repeated at least 10 times. In total including commissioning tests the system

has gone through approximately 800 breakdowns. The results are plotted from Figure 6.1 to Figure 6.3 for krypton, xenon, and argon respectively, the lines joining data points are shown only for easier identification of the datasets.

Figure 6.1 shows the breakdown characteristics for krypton, across most of the pressures tested there is a higher V_b at the smallest and largest separation and a minimum V_b in-between, which is characteristic of breakdown plots, with similar trends followed with the xenon and argon tests. A clear difference between the gases is apparent with argon having the lowest breakdown voltages and xenon the highest, this is due to the difference in the mean free path of the electron ionization incidents, which is the average distance in the field direction for an electron to travel between two ionization incidents. Table 6.2 highlights this disparity between gas species, showing that the minimum reached breakdown voltage was 271 V for argon, other developers HHC attempts have achieved minimum breakdown voltages of around 300-350 V for xenon, as shown in Table 2.2. The variance of the breakdown voltages of each gas species is relatively small, <10% from mean, for the pressure and distance ranges tested.

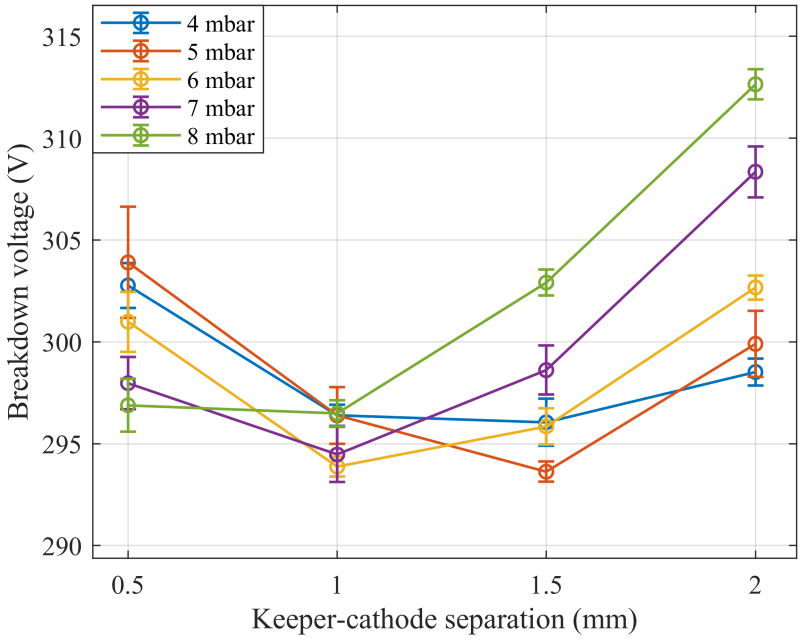

Figure 6.1: Krypton breakdown voltage characterisation, open keeper backfilled configuration.

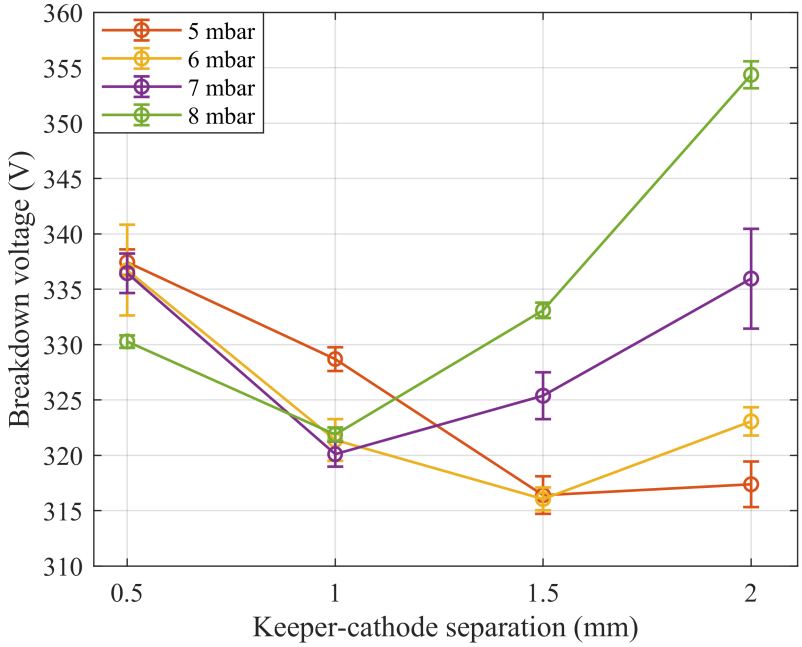

Figure 6.2: Xenon breakdown voltage characterisation, open keeper backfilled configuration.

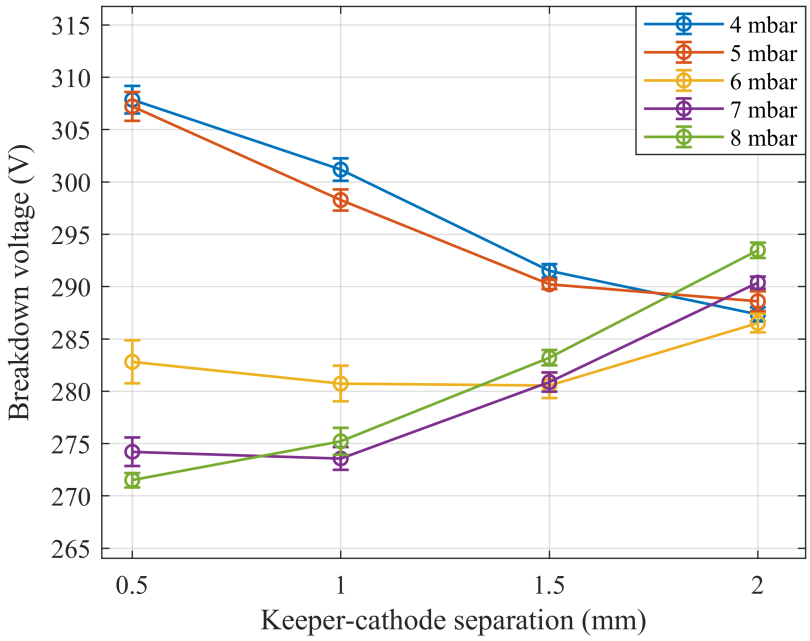

Figure 6.3: Argon breakdown voltage characterisation, open keeper backfilled configuration.

Assuming the breakdown occurs at the minimum electrode distance, d_{c-k}, and also taking the Paschen minimum for each pressure dataset as the separation at which the lowest breakdown voltage occurs, allows for estimating the mean Paschen minimum across the pressures tested for Kr, Xe and Ar in this HHC open keeper configuration. These results are shown in Table 6.1 and

are compared with the classical breakdown plots which are conducted with parallel plates, shown in Figure 3.1.

Table 6.1: Summary of the Paschen minimum.

Gas	Classical pd_{min} [74] (mbar∗cm)	HHC $\overline{pd}_{min}$ (mbar∗cm)	σ
Krypton	1.46	0.69	0.09
Xenon	0.89	0.79	0.09
Argon	1.32	0.76	0.23

The Kr and Ar mean Paschen minima are found to have a percentage change of 53% and 56% lower than that of the classical breakdown plots respectively, though Xe is found to be only 11% lower. These differences are likely due to the hollow cathode geometry, as was shown in Figure 3.2, the hollow cathode geometry can reduce the Paschen minimum by 25%, indicating that this HHC breakdown data reasonably agrees with the classical theory though with the hollow cathode offset. There could be a large uncertainty in the distance due to the mentioned assumptions in calculating these Paschen minima, but this uncertainty would increase the Paschen minimum values calculated as they are based on the smallest electrode separation.

Outside the pd operating ranges shown there is likely breakdown voltages which increase as shown in conventional Paschen curves. Though practically testing this within this backfilled setup is not possible, at lower cathode-keeper pd values, the discharge visibly propagates around the cathode to the back plate, due to the preferential pd. At higher cathode-keeper pd values, the discharge localises and there is spot attachment to the tube or radiation shield. Furthermore, this discharge stability behaviour is realised in the nominal enclosed keeper testing, where discharge stability is significantly enhanced with a propellant line pressure of 3-7 mbar, with failed ignitions occurring frequently outside that range, in which non-uniform discharges are formed. The electrode separation was not observed to have a significant influence on the discharge stability, ignitions were possible from 0.25 to 5 mm. Though, as can be seen from the results, 0.5-1.5 mm cathode-keeper separation provides the required pd to reach minimum V_b for most of the pressures with each gas.

Table 6.2: Summary of breakdown voltages, in V.

	Argon	Krypton	Xenon
$\overline{V_b}$	287	299	328
$V_{b,min}$	271	293	316
$V_{b,range}$	36	19	38

Visual inspection of the emitter before and after ~800 breakdowns found that no significant erosion occurred; the emitter downstream ID was measured and remained 2 ± 0.1 mm. Although some surface discoloration was noticeable, with blackening occurring near the emitter tip from original purple colour, indicating deposit from the carbon keeper to the emitter, this may cause an effective work function increase. However, full ignition was successfully achieved before and after the breakdown test campaign, indicating no significant detriment to the emitter surface from these ~800 breakdowns. This indicates that in practice the ignition control system employed (Section 4.2) effectively minimises the current surge through breakdown, mitigating the damage often apparent in other HHC designs (Section 2.3). On a separate emitter, initial commissioning attempts were made without any ignition control system, it was found that pulsed breakdowns occurred, as shown in Figure 5.17. During such breakdowns, material was visibly seen to sputter from the emitter surface, demonstrating the significant level of erosion occurring in uncontrolled heaterless ignition.

6.2.2 POST BREAKDOWN GLOW DISCHARGE

After breakdown occurs a low current discharge forms, which is sustained via secondary electron emission; for classical parallel plate discharges this transition is shown in Figure 3.3. To characterise this for the HHC, the keeper-cathode discharge voltage was measured during the V_b testing. The post breakdown discharge voltage is taken as the average voltage from 0.8 to 1 second after the breakdown occurs, as the discharge voltage stabilises after ~0.5 seconds. As mentioned, the current is limited to 10 mA by the power supply in conjunction with the ignition control system. The results can be seen in Figure 6.4. The discharge voltage drops from the breakdown voltage, as less potential is required for the current generation due to the space charge influence forming a sheath over the cathode, inducing more energy efficient ionisation. The discharge is enhanced further by the hollow cathode effect, and the secondary emission coefficient of the emitter, which has not been reliably reported for LaB_6 to the author's knowledge. The cathode-keeper separation has minimal influence on the operating voltage as Figure 6.4 shows. As the voltage drop is predominantly over the cathode sheath in glow discharges, such that increasing the electrode

separation only requires a small voltage increase to mitigate electron losses over the positive column [68].

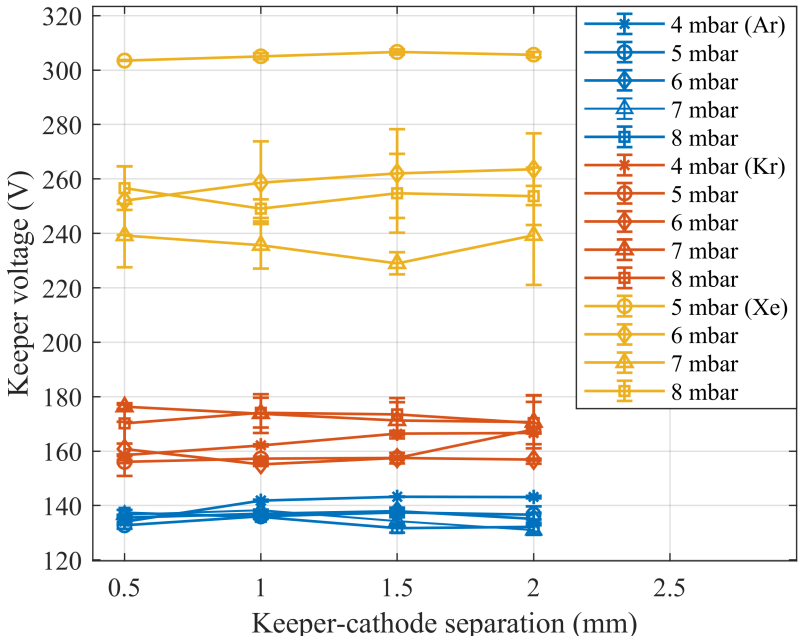

Figure 6.4: Post breakdown 10mA backfilled open keeper discharge.

Table 6.3 summarises the post breakdown discharge results. It can be seen, as with the breakdown results, the lowest potentials are for argon and highest for xenon, again this is due to the differences in the electron ionization mean free paths for the different gas species. Additionally, this results in higher potential drops from the breakdown voltage.

Table 6.3: Summary of post-breakdown discharge voltages, in V.

	Argon	**Krypton**	**Xenon**
$\overline{\mathbf{V}}$	136	165	263
$\mathbf{V}_{\mathbf{min}}$	131	155	229
$\mathbf{V}_{\mathbf{range}}$	12	21	78
$\overline{\mathbf{V}}_{\mathbf{b}} - \overline{\mathbf{V}}$	151	134	65

6.3 HEATING TO NOMINAL OPERATION

6.3.1 OVERVIEW

Once breakdown occurs, and the gaseous medium within the keeper-cathode region becomes electrically conductive, the heating phase begins, in which the discharge is sustained via secondary electron emission. This discharge mode rapidly heats the emitter via ion bombardment to the thermionic regime, if the required power is applied. The electrical and emitter thermal profiles of this process is characterised from Figure 6.5 to Figure 6.7, with the description and discussion over the following pages. These tests were conducted in the enclosed keeper discharge configuration, see Section 4.4, in which a xenon flow rate of 1.75 sccm was applied, with a keeper aperture of 0.25 mm. For the characterisation, the main ignition procedure outlined in Section 4.6.2 is carried out, where the keeper supply is pre-set to 700 V, 5 A, and the supply output is turned on. This increases the voltage until the voltage or current control limit is met. This ignition process is automatic beyond the power supply output being initiated by the user.

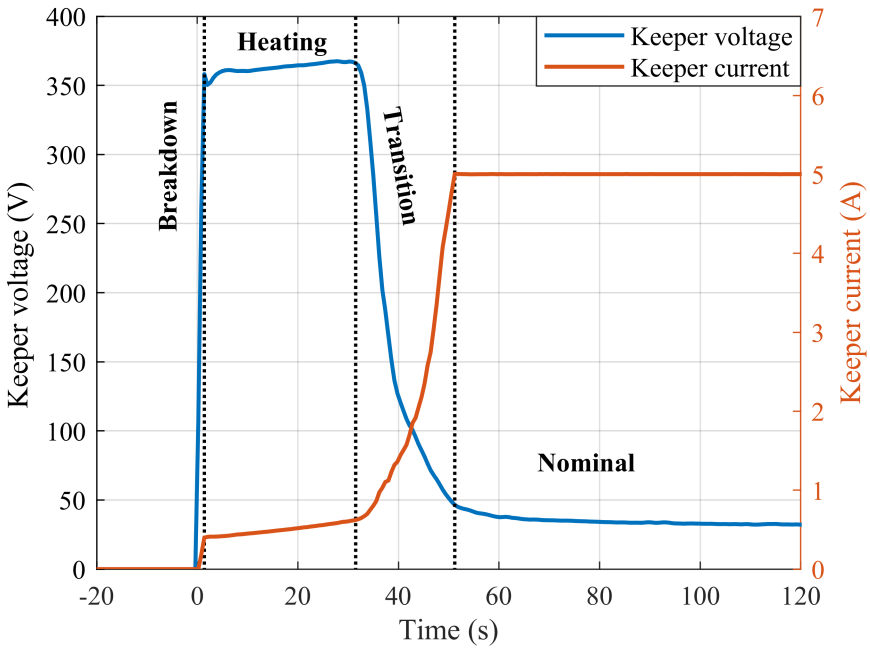

Figure 6.5: Keeper *V-I* vs time characterisation, enclosed keeper discharge configuration.

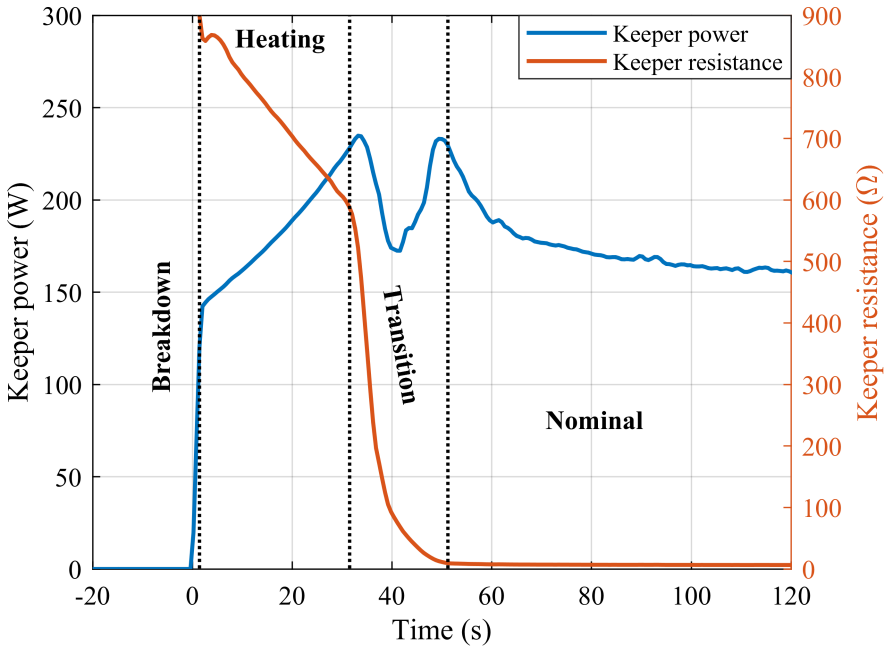

Figure 6.6: Keeper P-R vs time characterisation, enclosed keeper discharge configuration.

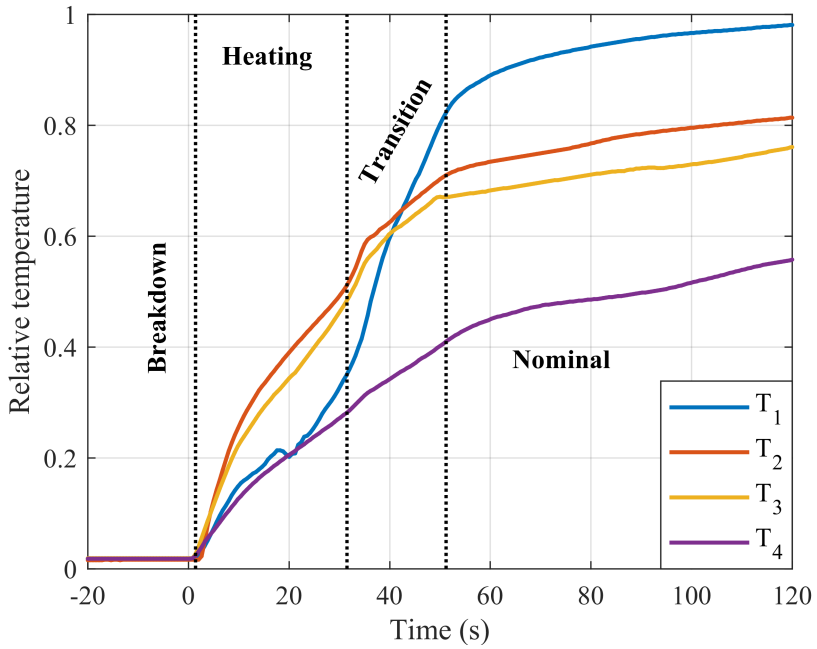

Figure 6.7: Emitter thermal profile vs time characterisation, enclosed keeper discharge configuration.

6.3.2 HEATING DISCHARGE

Figure 6.5 shows breakdown occurring with an immediate ~10 V voltage drop, from 1-3 seconds, as the discharge reaches the secondary emission stage, with an initially sustained current of 300-400 mA. This is the almost instant transfer to an abnormal glow discharge which has already surpassed the normal glow state, which was characterised for the HHC in Figure 6.4 for a current controlled discharge at a mere 10 mA. Hence the comparatively higher voltage post breakdown in the flow configuration is due to the increased current limit which causes the discharge to quickly enter the abnormal glow state. Though this higher current allows increased heating power to the emitter.

Through the heating phase the discharge current rises further, to around 700 mA, due to the increasing discharge voltage applied and a reduction in discharge resistance. This discharge voltage increase is due to the transient drop in the thermistor resistance, caused by the thermistors ohmic heating characteristics. The plasma resistance drops due to the discharges negative differential resistance, this property is the cause of requiring the ignition control system to stabilise the rise in current, as discussed in Section 5.2.14.

This process of gradually increasing the discharge current through the heating stage increases the heat flux into the emitter, enabling quicker transfer to a thermionic regime. Furthermore, beginning with a low initial current limitation, by having an initially high resistance, limits erosive inrush currents that form due to the sudden plasma resistance drop from effectively infinite resistance pre-breakdown, to <900 Ω during breakdown. This heating stage can be seen to be around 30 seconds, this time depends on the voltage limit of the power supply, thermistor and inductor characteristics, as well as the discharge characteristics such as gas type and pressure.

The discharge power and resistance are depicted in Figure 6.6, the power can be seen to steeply increase at a rate of 3 W/s during the heating phases due to the mentioned voltage and current increases, as the resistance drops at a rate of 10 Ω/s.

In Figure 6.7, the relative thermal profile of the emitter is shown, from the upstream end of the emitter at T_4 to the downstream emitter end at T_1, see Section 4.5.2. The emitter thermal profile starts with the HHC at room temperature and shows the profile change through ignition. The centre of the emitter, monitored by T_2 and T_3, can be seen to rise at similar rates through the heating phase, as does the emitter edges for most of the phase, monitored by T_1 and T_4. Though the centre rate rise is on average 1.5 times faster than the edges. This profile of the emitter centre heating at higher rates than the emitter edges supports that the emitter has a relatively uniform heat flux applied during this phase. This is due to the thermal heat balance of the emitter, with higher radiative losses from the emitter tip and higher conductive losses from the emitter base,

and thus the lower temperature at the emitter edges despite the uniform discharge power applied across the emitter during this phase.

6.3.3 TRANSITIONAL DISCHARGE

Once the emitter begins non-negligible thermionic emission, the transition phase begins. Practically this is seen as the discharge voltage and resistance reduction, that occurs around 30 seconds into the ignition, caused by this increasing thermionic emission. However, at around 25 seconds into the ignition, still within the defined heating stage, T_1 can be seen to begin diverging from T_4, with a sudden 15% increase in its temperature rate in comparison to T_4. This signifies that changes in the heat flux input into the cathode are occurring, perhaps from the discharge location beginning to transition to the emitter tip even with the absence of the production of significant thermionic emission to cause the voltage drop characteristic.

At 30 to 50 seconds T_1 rate significantly increases, up to 50% higher compared with the first 20 seconds of the discharge. T_4's rate of increase drops 30% during this transition phase, whereas T_2 and T_3 rate decreases by just over 50%. This signifies a significant change in the thermal input towards the emitter tip from relatively uniformly across the emitter, with the emitter tip becoming significantly hotter than the emitter base.

Interestingly in this transition period the power drops suddenly, as the discharge transforms to the thermionic regime, with plasma resistance dropping at 57 Ω/s for the first 10 seconds, then levelling off to 10 Ω over the remaining 20 seconds of the transition period. The power shortly recovers from the dip minimum 10 seconds into transition, this is due to the discharge requiring a sufficient heat flux to maintain the thermionic emission.

The discharge power before and after transition is almost identical, as the emitter is still bombarded by ions for heating. Though conversely to the heating stage there is a significantly increased quantity of ion bombardment incidents at lower energies, as is seen by the 320 V drop in voltage during transition. This results in a higher current emission to erosion ratio, as the sputtering is a function of the ion energy, as shown in Figure 5.10. This repeatable transition characteristic clearly identifies the change from the secondary emission to that of the thermionic. The resistance and inductance from the ignition control system dampen this unstable transition process, in order to maintain a diffusive discharge throughout, as cathodic spots can form during sudden current changes between the glow to thermionic transition.

During this transition the current rapidly rises from 0.6 A to the required value, arbitrarily set to 5 A in this test to demonstrate the quick and large current rise possible. Meanwhile the voltage drops 320 V to just under 50 V. The keeper discharge can be ignited to just 1-1.5 A to reach the

nominal ignition, for subsequent transfer to the anode discharge. The transition period shown is around 20 seconds, this depends on the cathode thermal shielding as well as the electrical and gas properties mentioned before, and on the current limit for the nominal discharge.

6.3.4 NOMINAL KEEPER DISCHARGE

The cathode is ignited from room temperature, and after 50 seconds the keeper discharge is in nominal operation, compared with over 10 minutes for conventional ohmic heated cathodes [26]. At this stage the HHC appears to operate equivalently to conventional HCs. Though nominal keeper discharge operation is still not equivalent to thermal steady state operation, which can take over 30 minutes to be reached. Over the 70 seconds of nominal keeper discharge shown in Figure 6.7, the rate of temperature increase reduces significantly, for T_1, an over 90% drop compared with the transition phase, which is due to the emitter thermionic temperatures already being reached and further thermal increases merely caused by transition towards thermal equilibrium. In nominal operation the relative difference between the T_1 to T_4 rate of change is <10 %, indicating a relatively static emitter thermal profile input has been reached. Though the emitter heat flux profile is again significantly proportioned toward the downstream emitter tip. Also over the 70 seconds of nominal keeper discharge shown the discharge voltage reduces from 51 to 31 V, with a discharge resistance dropping to 6 Ω by 120 s. After 30 minutes relatively smaller changes occurred to the discharge parameters, with the voltage dropping to 25 V, with a corresponding discharge power of 125 W.

6.4 DISCHARGE ATTACHMENT

The keeper-cathode discharge propagation from 0.01 to 1.00 A is displayed in Figure 6.8, these tests were conducted in the backfilled open keeper configuration, see Section 4.4, to allow for optical access between the keeper and cathode. For this testing the keeper power supply voltage was set to 700 V, and the supply's current limit was manually varied from 0.01 to 1.00 A with imaging taken at various setpoints, during this test the supply remained in current control.

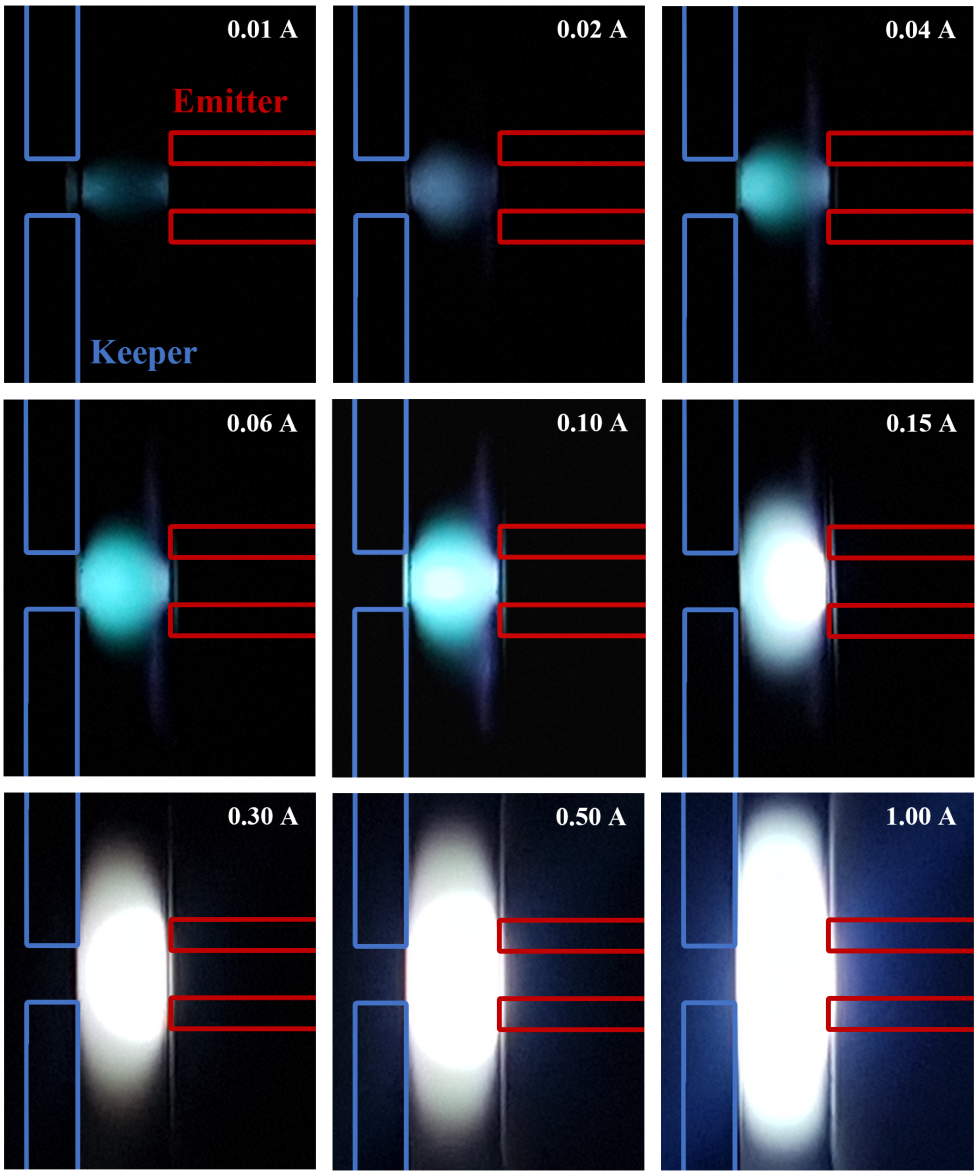

Figure 6.8: Backfilled open keeper discharge imaging from 0.01-1.00 A in Xe, at 5.5 mbar with a d_{k-c} of 4 mm, and 1/500 sec optical exposure.

At the initial 0.01 A keeper discharge, the keeper and cathode glows are apparent, both attachments emanating from their inner hollow cylindrical geometries, due to the hollow cathode and anode effects [20, 172]. At 0.04 A a faint vertical discharge on the cathode can be seen, this is the discharge attaching over the outer cathode surface with the increased current, which is a characteristic of the normal glow, to spread attachment across the entire cathode surface to increase secondary emission, with minimal voltage increase. As the current increases beyond 0.04 A the discharge cannot spread further due to the insulating sleeve (shown in Figure 5.1) limiting the attachment area, so the discharge intensity increases to yield higher secondary emission in order to sustain the higher current operation, with increasing voltage as was seen in Figure 6.5. With a higher current, typically more than 0.15 A and enough time, thermionic emission can occur,

as shown in the 0.15 to 0.3 A images. With thermionic emission the discharge transitions into an intensified ball discharge, that simultaneously retracts partially into the hollow cathode cavity, again due to ionisation enhancements of the hollow cathode effect. Additionally, the keeper and plasma column discharge sections become much dimmer and more optically transparent, with the luminosity strongest from the hollow cathode. With increasing current, the ball discharge begins to emerge from the hollow cathode. The discharge additionally appears to further whiten due to the increased thermal radiation, that saturates the visible spectrum. Also, it appears that as the current increases the discharge column cross section increases, this influence is likely enhanced by the unconfined open keeper setup. Finally, without containment of the normal glow discharge, by the insulating casing, the discharge would continue to spread over the whole cathode area, as was shown in Figure 5.15, which results in inefficient heating of the emitter, and makes transition to the thermionic regime challenging.

6.5 GAS AND PRESSURE INFLUENCE

6.5.1 GAS SPECIES INFLUENCE

The emitter downstream end was measured with an optical pyrometer, as described in Section 4.5.1, from the transition to thermionic emission which occurs around 0.3 A to nominal keeper discharge operation above 1 A. The pyrometer gives accurate temperature measurements of the emitter tip through this process, however below 0.3 A the thermal radiation emission is too low for the pyrometer to accurately measure, hence measurements begin from 0.3 A. Figure 6.9 and Figure 6.10 display the emitter tip temperature and *V-I* characteristics for Ar, Kr and Xe gases in the backfilled open keeper configuration, see Section 4.4, at 5.5 mbar with a 4 mm cathode-keeper separation.

Figure 6.9 shows that the emitter tip temperature increases steeply from 0.3 to 0.5 A, going from around 1100 ℃ for all three gases and increasing by 125 ℃ for Xe, 225 ℃ for Kr and 275 ℃ for Ar. Beyond this, the emitter temperature increases are significantly smaller, as the discharge is more significantly thermionically emitting. The voltage can be seen to drop significantly during this process as expected. The higher voltage and temperature of the emitter for argon is likely due to the higher ionisation potential, and lower ion mass, requiring a higher electric field strength to maintain sufficient ionisation, which also increase the ion bombardment energy to the surface, thus increase the emitter temperature and therefore the thermionic emission. Additionally, at 0.3 A the temperature difference between the gas species is the smallest, indicating a higher proportion of secondary emission discharge at this stage compared to that of the 0.5 A. These results and that of the transient ignition characterization, support that the transition period occurs

in which the discharge is both a thermionically and secondary emission sustained discharge. This stage is found to be stable, via power supply current limitation, for only short periods of time, typically <5 minutes, as either it will switch to a thermionic regime, or cathode spots can appear, in which damaging discharge localization occurs. Quick, though stable transfer through this transition period is critical for successful ignition.

Figure 6.9 also plots the Richardson equation to calculate the emitter temperature required to provide the current from thermionic emission only, see Section 5.2.2 - Equation (5.4), with $J = S/I$, where S is the exposed emitter surface and I is the discharge current. As such the Richardson equation is plotted for varying surface attachment, from 30% to 100% of the emitter surface. The thermionic profile matches the Ar plot from 0.5 to 1.3 A, for a 0.6S well. Though the relative thermal profile given in Figure 6.7, shows a large temperature gradient from T_4 to T_1 in nominal operation, indicating that likely <30% of the emitter is active. Hence there is a disparity in the predicted and measured tip temperature. Other groups have also reported lower temperatures than predicted for LaB_6 [26], which may be due to lanthanum recycling mechanisms converting the LaB_6 to LaB_4 which has a lower work function. Though alternatively, this disparity may be due to a sizable ionic current, thus requiring less thermionic emission to sustain a given current. The trend agreement between the experimental and predicted emission supports that from 0.5 A the discharge current increases are supplied by predominately thermionic emission.

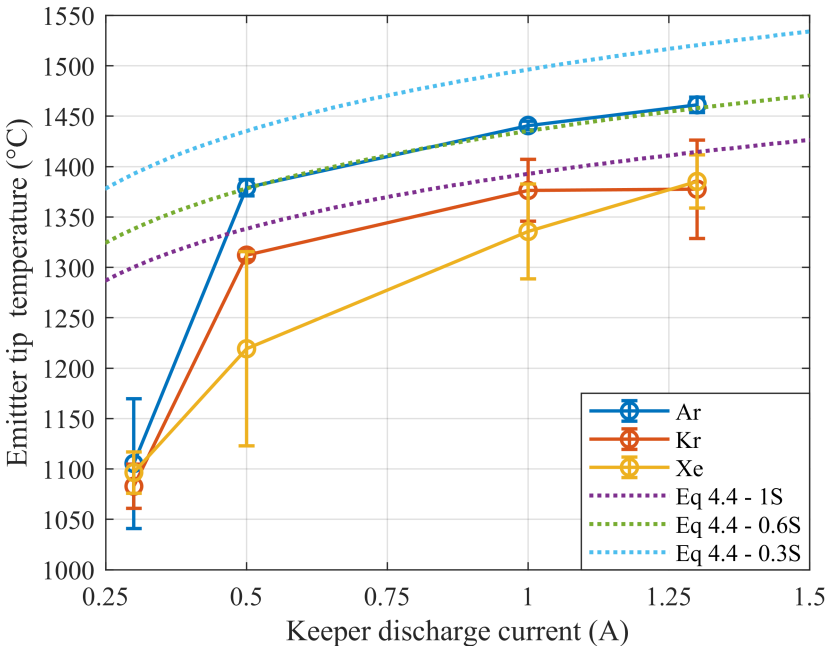

Figure 6.9: Influence of gas species on emitter tip temperature in the backfilled open keeper configuration, 5.5 mbar, 4 mm separation.

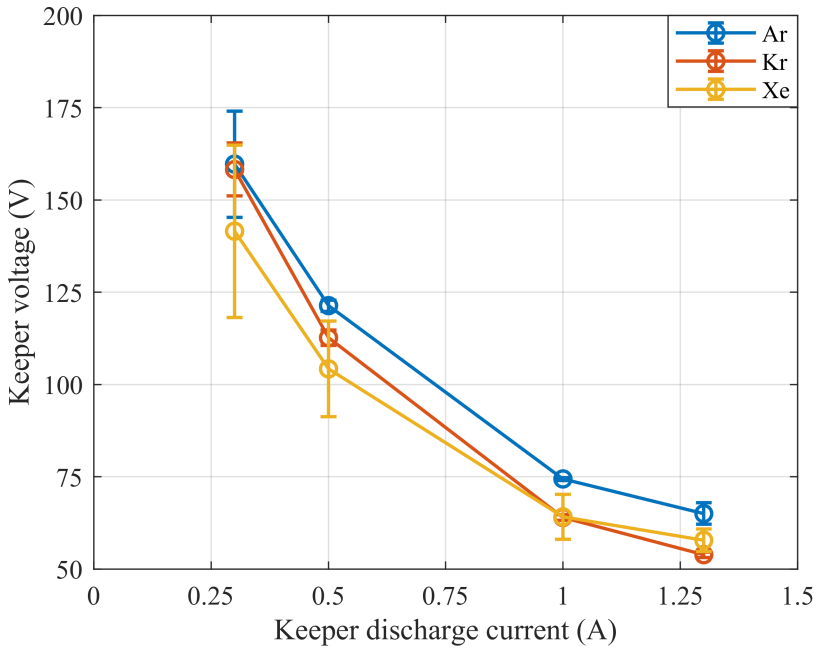

Figure 6.10: Influence of gas species on keeper voltage in the backfilled open keeper configuration, 5.5 mbar, 4 mm separation.

6.5.2 PRESSURE INFLUENCE

The pressure influences on the transition to nominal keeper discharge were investigated in the same backfilled open keeper configuration with pyrometer measurements as the prior section on the gas species investigation. Although only Xenon is used for the pressure investigation. Three keeper discharge pressures, 2, 5.5 and 10 mbar are shown characterised in Figure 6.11 and Figure 6.12. These operating pressures are stable and repeatable once the HHC is ignited to the transition or nominal operation phase. The HHC cannot breakdown and form a stable secondary electron emission sustained discharge with pressures below ~4 mbar and above ~7 mbar as discussed in Section 6.2.1, due to the discharge not attaching uniformly or at all to the emitter outside this pressure range. 5.5 mbar was empirically found to consistently operate across Ar, Xe and Kr to efficiently ignite the discharge, hence this was defined as a standard setpoint for various tests. Thus, to conduct these pressure influence tests the ignition was achieved with a pressure first set to 5.5 mbar, and then once ignited to a keeper current of 1 A, the pressure was adjusted to the required value and the current was varied from 0.3 to 1.3 A.

The pressure influence on the keeper discharge is apparent in the tests shown in Figure 6.12 and Figure 6.11. From 10 mbar to 2 mbar there is a ~20% increase in keeper discharge voltage across the current range which corresponds to a nearly 15% increase in emitter tip temperature at 0.3 A, that gradually drops to a 2.5% increase at 1.3 A. This indicates that at lower pressure the increase in the ionisation mean free path, results in an increase in the voltage to sustain the required

ionisation incidents. The increase in voltage also increases the energy of the ion bombardment, further heating the surface. The 15% temperature increase from 10 mbar to 2 mbar at 0.3 A indicates that the thermionic emission component of the discharge current increased as pressure decreased due to the reduction in the ionisation incidents. As the current rises the thermal differences between the three pressures measured reduces, this is perhaps partially due to the discharge changing to a mostly thermionic discharge at this current level, and hence reducing the dependency on gas pressure. Also, at higher temperatures the thermionic emission sensitivity increases, such that small temperature differences gives rise to large emission current differences, as shown in Figure 5.2. The 2 mbar pressure sustains higher voltage than the 5.5 and 10 mbar pressures despite the emitter temperature difference reducing, this is still likely due to the increase in the ionisation mean free path, so that the higher voltage is required to attain the equivalent emitter heat flux. Finally, the Richardson curves show the same effect as seen for the gas species plots, with the measured temperatures significantly below that of the prediction, given plausible surface attachment assumptions, as discussed.

The *V-I* transition from secondary emission sustained discharge to thermionic discharge shown in Figure 6.10 and Figure 6.12 is noticeably similar to the classical gas discharge characteristic shown in Figure 3.3, indicating that despite the complex geometry and thermal arrangement of the HHC the operational trends are still similar to classical gas discharge theory.

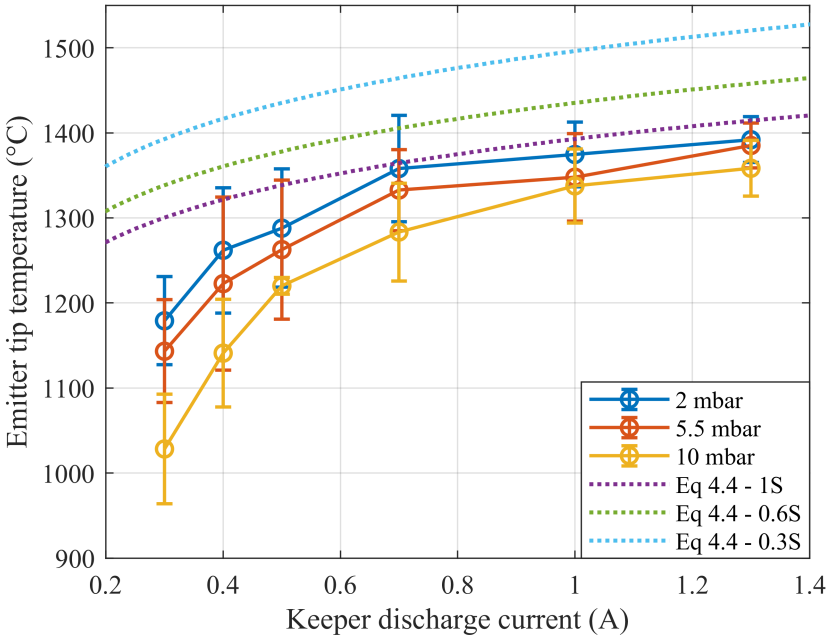

Figure 6.11: Influence of pressure on the emitter tip temperature in the backfilled open keeper configuration, 5.5 mbar, 4 mm separation.

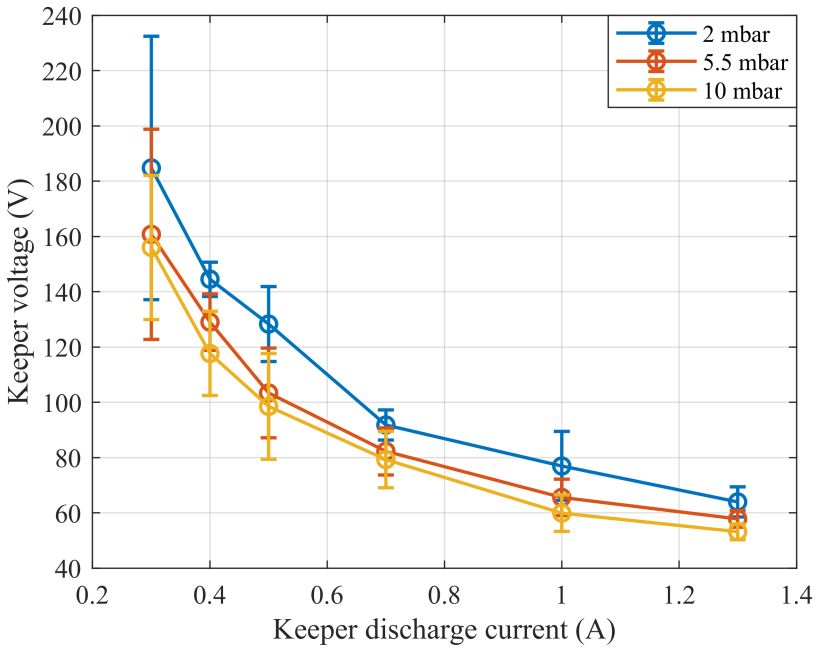

Figure 6.12: Influence of pressure on the keeper voltage in the backfilled open keeper configuration, 5.5 mbar, 4 mm separation.

6.5.3 PLASMA DENSITY CHARACTERISTICS

The cathode-keeper plasma electron density, n_e, for Kr and Ar is measured spectrographically in the backfilled open keeper configuration, with the procedure and setup outlined in Section 4.5.3. As discussed, the Xe discharge electron density was unable to be measured with this approach due to a relatively strong Xe ion line concealing the $\lambda_{H-\beta}$ line. The results of the plasma electron density verses keeper discharge current are shown in Figure 6.13. The Kr density is initially around $2.4{*}10^{20}$ m^{-3} compared with the $1{*}10^{20}$ m^{-3} for Ar at a keeper current of 0.4 A. $n_{e,Kr}$ can be seen to rise initially at 0.5 A and then gradually decrease up to 2 A. $n_{e,Ar}$ appears to have a similar trend of increasing up to 1 A, and with the mean then decreasing at 1.3 A. The cause of the electron density decrease is likely a result of the measurement collecting emission from the whole discharge cross section from cathode to keeper (see Figure 6.8). Thus, measuring the effective average electron density of the discharge. It is suggestive that the plasma discharge volume increases due to the unconfined nature of the backfilled open keeper discharge, as potentially seen in the imaging in Section 6.4. An increase in discharge volume can cause the average N_e density to decrease, with the core plasma density increasing with current as expected.

The order of magnitude of these plasma density measurements are reasonably close to those of a conventionally heated LaB_6 cathode conducted with Langmuir probes [23]. These Langmuir

probe measurements were conducted on a HC with an anode discharge and operated at significantly higher currents, 20-100 A, though the results showed the peak plasma density consistently remaining within ~$5*10^{20}$ to $1*10^{21}$ m^{-3} for this large current range. Thus, as this HHC plasma density profile is approximately within an order of magnitude of these results shows reasonable alignment of the data with that available in the literature for comparative LaB_6 systems.

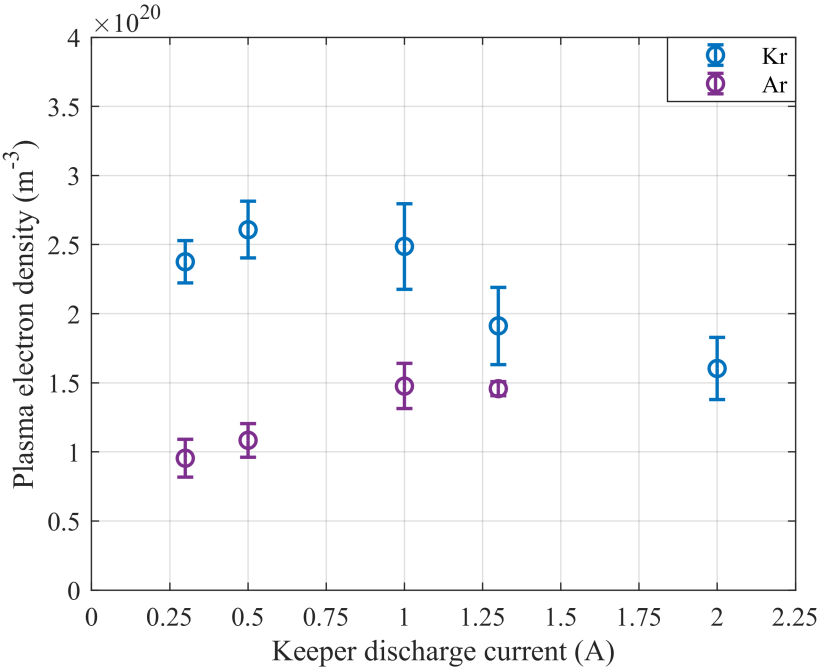

Figure 6.13: Plasma density characteristics for Kr and Ar in the backfilled open keeper configuration, 5.5 mbar, 4 mm separation.

6.6 ANODE DISCHARGE

6.6.1 ANODE *V-I* CHARACTERISTICS

Once a cathode is ignited with a nominal keeper discharge, the discharge is then transferred to the thruster discharge chamber or ion beam for main operation. Alternatively, the discharge can be transferred to an anode to simulate operation with the thruster, which can also give a stable benchmark for cathode testing. Though unfortunately there is still no standardisation within the EP field on anode test configurations, such that cathode comparisons are challenging. The HHC has been tested in the anode discharge test facility, as described in Section 4.3. The HHC is tested with a keeper aperture of 1.8 mm. For the anode discharge testing the main ignition procedure is operated (see Section 4.6.2). Once the HHC was ignited and thermionically emitting with the keeper discharge between 1-2 A, the discharge is maintained for a stabilisation period of 1-3 minutes then the anode potential is applied, with the anode current limited initially to 0.5 A and

then levelled up to the required setpoints, this gradual ramp-up is to support the discharge stability. Once the anode discharge is beyond 1 A, the keeper discharge is switched off, such that the keeper is left floating, this is a typical practice for most conventional discharge HCs.

Throughout ignition of the HHC for the anode discharge tests, the xenon mass flow rate was set to 13 sccm. With a 1 A anode discharge, this flow rate was found to give a pressure reading of around 6 mbar on the propellant line dial gauge, which is ~1.5 m upstream of the HHC, described in Section 4.3. Estimating the keeper entrance pressure using the analytical equations described in Section 5.2.11, with a gas temperature in the order of the measured emitter temperature of 1400 °C, this calculates a pressure of 3.6 mbar for a keeper aperture of 1.8 mm. With the discharge on at 15 A, the upstream pressure would increase to around 6.5-7.5 mbar. Mikellides has shown that the viscosity of the cathode flow can have a large impact on the pressure calculations, with more than 40% increase in pressure with viscosity considered [89]. The backfilled testing indicated that a pressure of >4 mbar is required for reliable ignition, this was due to the discharge attaching around the cathode to the mount, as the system was not enclosed. Whereas the enclosed keeper flow setup, contains the discharge between the keeper and cathode, such that <4 mbar may be possible. A few other propellant flow rates were attempted, such as 10 sccm. The HHC did achieve ignition at such flow rates, though during nominal anode operation, high voltages occurred, characteristic of plume operation, in which there is insufficient neutral pressure for ionisation to maintain the spot mode operation. Thus, the flow rate was maintained at 13 sccm for xenon.

The HHC anode discharge *V-I* characteristic from 1-30 A is shown in Figure 6.14. The discharge voltage is initially significantly higher, with 60 V at 1 A, halving to around 30 V at 5 A, this effect is merely to sustain the discharge power for sufficient heating of the emitter via ion bombardment. This is also the same profile trend seen for the keeper discharge, as shown in Figure 6.10, and again of the classical discharge theory, as shown in Figure 3.3. With increasing current from 5 to 20 A the discharge voltage can be seen to level off, around 20 V, with little change above 10 A, this is typical of hollow cathodes [39]. Though with further increases in discharge current HCs have a small variance in the discharge voltage until the current becomes too high and the voltage begins to rise [39]. The discharge voltage rise at high current is typically due to the thermal balance of the cathode, with increasing radiative losses at higher temperature operation, requiring increased ion bombardment. The thermal design of the cathode can significantly influence the magnitude of this trend, due to the thermal balance.

The HHC was sized for a nominal discharge current of 20 A as mentioned, though due to research aims of high power HHC development, this HHC was operated up to 30 A, as shown in Figure

6.14. During this high current anode testing, operating at >20 A, no adverse effects, such as a rise in discharge voltage mentioned, high voltage fluctuations or shifting to plume mode were detected. Thus, this indicates that the HHC could operate above 30 A, though precautionarily higher current operation was not tested. Furthermore, if the HHC were to operate at very high currents, beyond 40 or 50 A, the discharge voltage would likely rise as discussed and given the sizing of the cathode such operation would significantly reduce HHC lifetime, as shown in Section 5.2.3.

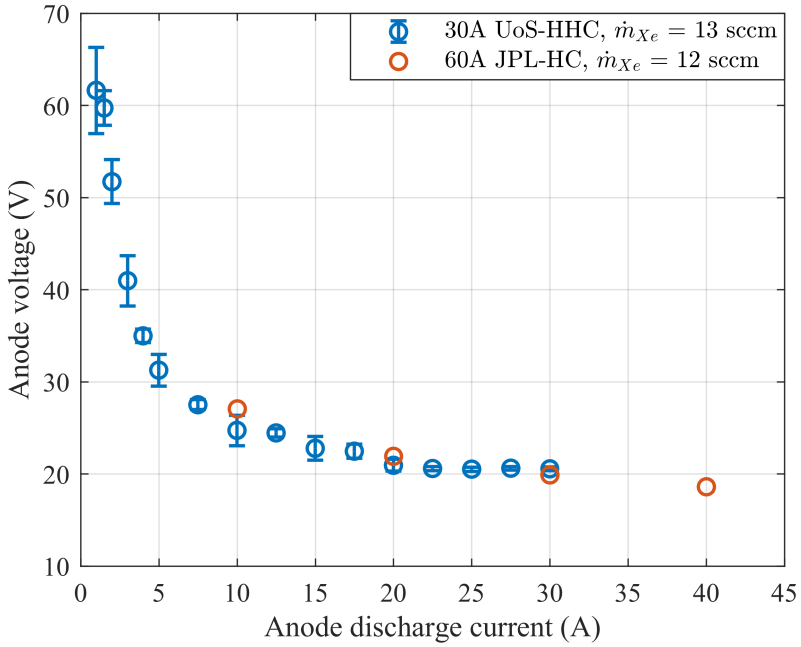

Figure 6.14: Anode discharge *V-I* characteristics for the UoS-HHC and JPL-HC [120].

The performance of a well-established conventionally heated LaB_6 HC from JPL NASA is also displayed in Figure 6.14. It must be noted that direct quantitative comparison of the HHC and the JPL HC would be misleading due to a lack of standardised cathode testing as discussed, leading to inevitable variance in test conditions. Specifically, it is well known that the anode geometry and positioning have a strong impact on performance, furthermore the conventional JPL cathode displayed is designed for current operation 3 times higher than the HHC and for a flow rate 1 sccm less. Hence this plot does not discern in any way which cathode has better performance. Nevertheless, the striking similarity in operational trends is a good initial indication that this heaterless ignition method does not significantly degrade nominal operational performance of the HHC, while achieving the fast heaterless ignition with nominal flow rates.

6.6.2 KEEPER PURPOSE AND INFLUENCE

The keeper orifice reduction is one of the main geometric differences from the HHC to conventional HCs. The HHC keeper from breakdown to the nominal heating phase acts as a conventional HC keeper, to aid ignition, helping to maintain a stable discharge and protecting the emitter. Also, the HHC keeper acts as a conventional HC orifice increasing the pressure in the emitter region, though this is as well as increasing the pressure in the emitter-keeper gap to support relatively low voltage heaterless ignition as discussed. Post-ignition, in nominal operation with an anode discharge the HHC keeper is geometrically similar to a conventional cathode orifice, constricting flow, and electrically like a conventional discharge HC keeper as it's electrically floating. The keeper could possibly be tied to cathode potential post anode transfer, via a switching mechanism, though this could affect discharge stability and furthermore this may increase the heaterless keeper erosion due to the larger keeper-plasma potential difference with the keeper grounded. Nevertheless, if the keeper were to be grounded in nominal operation, it would be very similar electrically and geometrically to a conventional HC orifice at that stage.

A photo of the anode discharge operation is shown in Figure 6.15, at the 30 A setpoint, with the discharge in spot mode. The discharge can be seen appearing from the keeper exit, with the hollow cylindrical anode seen on the right-hand side. Also the keeper end can be seen to be light red and occurs during high current operation, >20 A; this is due to the plasma heating. It is a common occurrence for the cathode orifices of high current HCs [173], which have measured orifice temperatures of 1300 ℃ at anode discharge current of 30 A [120]. This has led developers to design orifices with enhanced radiative cooling, contrary to the typical design process of minimising cathode thermal losses. Although the keeper was visually light-red the thermal measurements with the pyrometer were not possible, as the thermal radiation was below the accurate measuring capabilities of the pyrometer, indicating the keeper temperature remained below 800 ℃. This lower temperature of the HHC keeper orifice compared with the conventional HC orifice is likely due to the higher radiative losses of the HHC external keeper orifice.

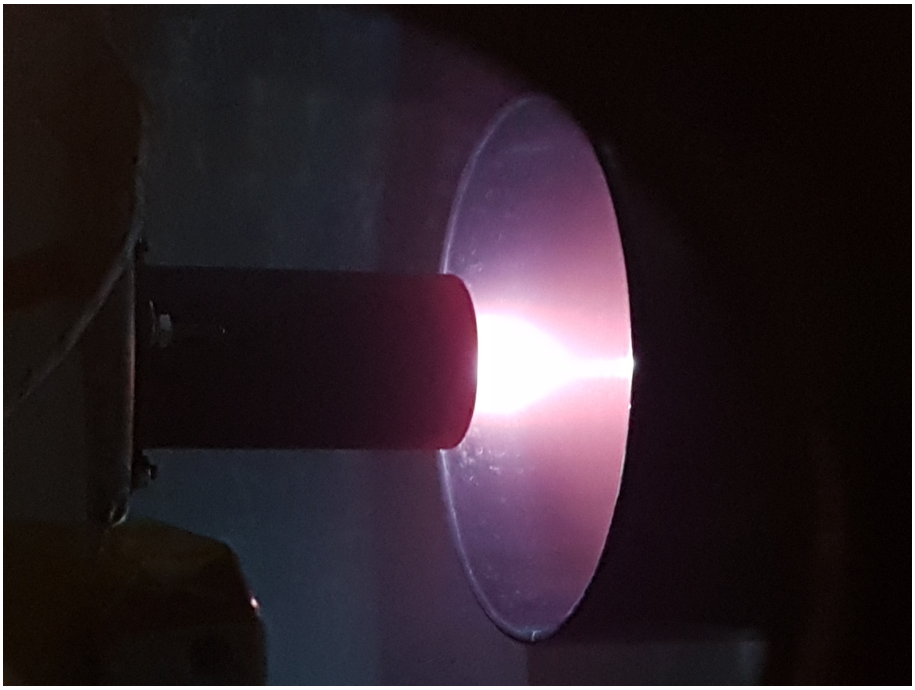

Figure 6.15: UoS-HHC 30 A anode discharge with 13 sccm (Xe)

6.6.3 KEEPER FLOATING VOLTAGE

The floating keeper potential is shown in Figure 6.16, again with the JPL-HC for reference, with the prior mentioned caveats when quantitively comparing. The keeper floats positive by around 55 V at 1 A with high variance, then drops rapidly within the first 5 A, before levelling off, with a very similar profile to that of the discharge voltage. The trend beyond 5 A is similar to that of the conventional JPL cathode, though the magnitude is significantly higher. The JPL keeper orifice is 68% larger than the emitter ID [23], whereas the HHC keeper in this configuration is about 6% smaller than the emitter ID, such that it constricts the plasma flow, effectively like a conventional orifice as mentioned. As the HHC keeper has a smaller orifice compared with conventional HCs, it collects more charged particles. The floating condition balances the ion and electron fluxes to have a zero-net current, such that the higher keeper floating voltage indicates increased ion bombardment to the keeper. Though as discussed, the keeper erosion will significantly depend on the keeper-plasma potential difference, due to the non-linear sputter yields (see Figure 5.10).

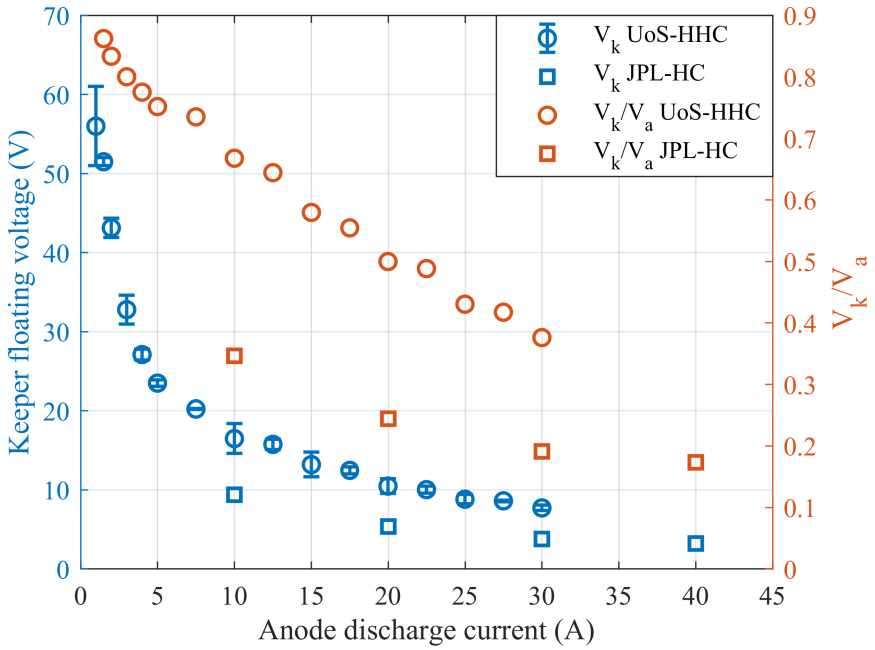

Figure 6.16: Floating keeper *V-I* characteristics for the UoS-HHC and JPL-HC in anode discharge mode.

Interestingly it can be seen in Figure 6.16 that the HHC keeper floating voltage, V_k, as a proportion of the anode discharge voltage, V_a, decreases almost linearly from 0.88 at 1 A to 0.38 at 30 A. The keeper floating measurement shows that as the discharge current increases, V_k drops at an increased rate, this is perhaps due to the thermionic emission proportion of the current increasing with increased discharge current, thus changing the net charge balance in the keeper potential. The conventional JPL cathode also shows V_k reducing at an increased rate to V_a, though as a much smaller proportion of the discharge current, from 0.35 at 10 A to 0.19 at 40 A.

6.6.4 KEEPER ORIFICE EFFECT

As discussed, the keeper orifice is reduced in comparison to conventional HCs for the purpose of increasing the emitter-keeper pressure to induce sub-kilovolt breakdown, as shown in Section 6.2.1. However, the keeper orifice size influences the current extraction to the anode as shown in Figure 6.17. For a keeper orifice diameter of 0.25 to 1.8 mm the maximum keeper orifice current density extraction to the anode was recorded. For the 0.25 and 0.4 mm keeper orifice the anode supply was set to the maximum potential of 200 V. At 1 mm diameter the discharge voltage was increased to a maximum of 73 V, and the current extracted was 7 A, and although potentially higher current could be extracted to the anode by increasing the voltage further, this was avoided due to the discharge becoming highly volatile, effectively limiting current density extraction below 800 A/cm^2 for the 1 mm keeper orifice. For the 1.8 mm orifice, the current extraction was not found to be limited up to 30 A, as was shown in Figure 6.14, and thus could potentially reach significantly higher extracted current densities with that orifice size. The mass flow rate for each

orifice size was adjusted to maintain a minimum flow rate while still in spot mode operation, this was between 1-13 sccm Xe throughout these tests.

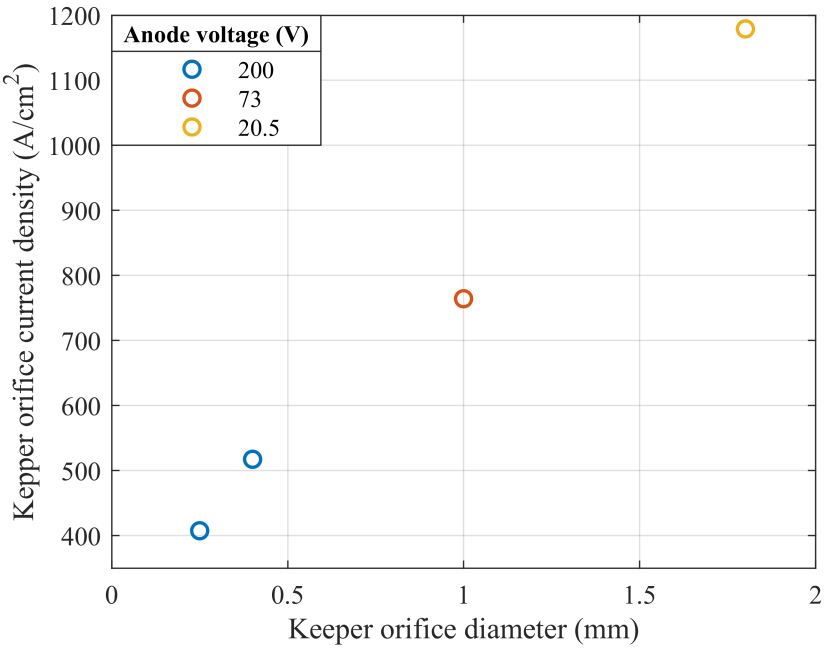

Figure 6.17: Maximum current density extracted through the HHC keeper orifice for various keeper orifice diameters.

Although this data inevitably has more than one varied parameter, it still clearly shows that the maximum extracted current density increases significantly with orifice size. For a 62.5% increase in orifice diameter the extracted current density increases by 75%, this enhancement is perhaps due to reduced wall losses, from the enhanced electron extraction from the emitter to the anode with the less constrictive orifice, such that the current density increases.

6.6.5 KEEPER OBSERVATIONS

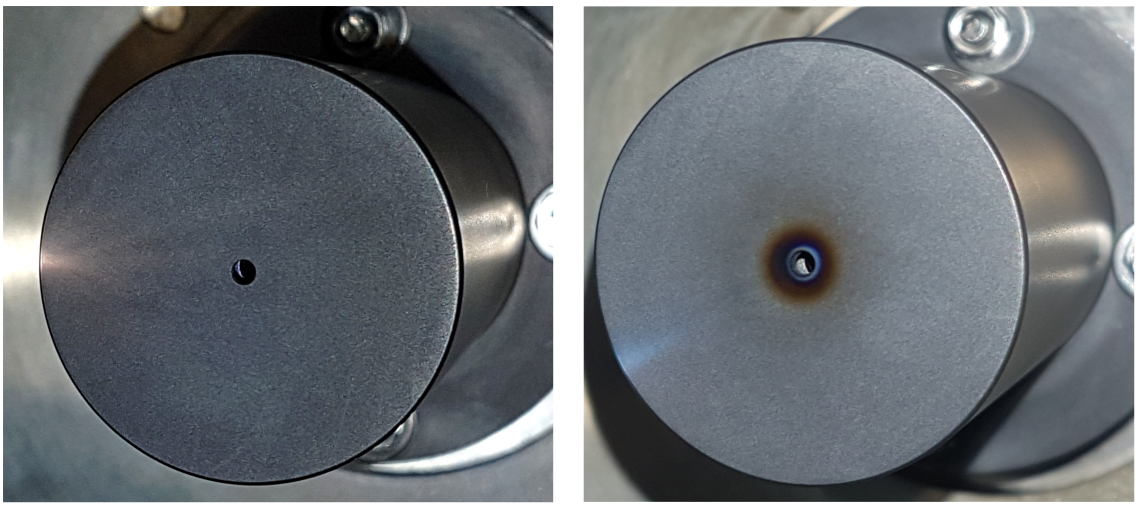

Figure 6.18: Photo of the keeper before (left) and after (right) several hours of anode discharge operation from 1-30 A.

The keeper was visually inspected before and after several hours of operation and multiple ignitions. The orifice diameter did not noticeably change, though there was a violet blue discolouration near the keeper orifice, as seen in Figure 6.18. These discolorations form uniform rings around the orifice, approximately 4 mm in diameter to the most outer ring; this is symbolic of ion bombardment sputtering, similar effects have been noticeable in conventional cathodes [174]. Operation in the hundreds of hours is required to meaningfully ascertain operational erosion levels. Conventional HCs have been significantly researched in regards to keeper erosion [155-157, 175], mostly since the NSTAR lifetime test resulted in the complete keeper orifice plate erosion after 30,000 hours [46], as was shown in Figure 5.11.

CHAPTER 7

CONCLUSION AND FUTURE RESEARCH

7.1 RESEARCH OVERVIEW

A novel high current heaterless hollow cathode concept has been developed, constructed and successfully undergone proof of concept and operational characterisation. This operational HHC can ignite with nominal flow rates, below 15 sccm, and does not require any additional propellant pulsing or bypass, in addition the system achieves ignition with voltages below 400 V, with discharge operation demonstrated up to 30 A. Thus, this UoS-HHC is a significant step towards the obsoletion of the conventional cathode heater component. The cathode heater component is a prominent failure mechanism of HCs within electric propulsion systems and is mitigated in the HHC, while also gaining savings in; mass, volume, PPU simplicity, ignition power, and cost.

This novel HHC has been characterised for the ignition operation, including breakdown, heating, transition and nominal keeper and anode discharge phases. Testing has been conducted both in a backfilled configuration, which allows increased diagnostic access to the system, and a nominal flow configuration, with an anode to simulate in-thruster operation. Diagnostics including the first direct pyrometer measurements of an emitter surface in a LaB_6 cathode developed for in-space applications, spectrographic electron density measurements of the emitter keeper gap, and thermocouple measurements of the emitter temperature profile.

7.1.1 NOVEL HHC DESIGN FEATURES

The high current HHC design encompasses multiple novel aspects to enable the soft diffusive heaterless ignition, which has had a patent application filed, with application number:1807683.6 [2]. Critically this novel heaterless ignition system for the first-time controls both the rise in

current and discharge attachment, to enable the non-surging diffusive attachment throughout ignition. Without this novel HHC soft start system the HHC can experience huge erosion and melting [27]. For the first time, the HHC ignition current rise and current stability are maintained by inductance, which impedes changes in current, and an NTC thermistor, which limits the maximum current, and passively self-heats reducing resistance with increased current and time. A 800 Ω thermistor and 150 mH inductor have been found to reliably enable this operation for HHC ignition. Furthermore, for the first time, the discharge attachment is isolated from the exterior cathode tube, to suppress the discharge spreading to the whole cathode during heaterless ignition, allowing significantly increased power input into the emitter, and thus reducing the required ion bombardment heating, and in turn reducing the sputter erosion.

7.1.2 IGNITION CONTROL SYSTEM INFLUENCE

Experimentally it was found that with an uncontrolled breakdown, the discharge current reached a peak in excess of 650 A, in under 40 μs, this visibly creates an erosive arc between the keeper and emitter. The influence of the ignition control system for HHC ignition has been characterised, with a semi-empirical electrical model. The breakdown voltage has a large influence on the discharge energy, with a peak current of 1 kA with a breakdown voltage of 750 V, compared with peak current of only 130 A for a breakdown voltage of 100 V. Thus, minimising the breakdown voltage minimises the requirements placed on ignition control system to stabilise the current. Additionally, the ignition control system can be seen to reduce the original peak current by 3 orders of magnitude to 0.6 A, whilst also delaying the current rise, such that the current peak occurs almost 20 times slower, at 0.75 ms. These effects can significantly reduce the erosion in heaterless ignition and support more reliable ignition.

7.1.3 THERMAL DESIGN

For high power cathode operation, the thermal analysis of the cathode is critical for efficient power usage and to extend operational lifetime. A simple thermal model has been created to assess the main parameter changes which influence the cathode heat balance. These new findings are pertinent to not only this HHC, but the broader HC field, as the thermal design of the HHC is in common with that of HCs. The radiation shield was found to be most efficient when covering most of the cathode tube length, such that a 55 mm long shield requires 12% less power input into the emitter to reach 1600 °C compared with a 25 mm shield, which is just longer than the emitter. Furthermore, it was found that the majority of the power savings are within the first layer of the heat shield and there are diminishing returns witch each extra layer. Beyond around 20 layers there is a negligible increase in power efficiency. Finally, a high cathode length to width aspect

ratio significantly increased power efficiency, though this requires appreciation to the structural integrity required to withstand launching and thermal fatigue endured during cycling.

7.1.4 BREAKDOWN ANALYSIS

The HHC breakdown was investigated with Ar, Kr, and Xe propellant in the backfilled open keeper configuration, with around 800 breakdowns occurring in total. Visual inspection found no significant emitter damage from this operation, and full ignition was achieved before and after the breakdown campaign. This indicates that the ignition control system implemented has ensured that the breakdown stage of ignition is not a life limiting operational phase. The keeper-emitter separation was investigated, demonstrating the Paschen minimum is reached for all three gases between 0.5-2 mm and 5-7 mbar. Breakdown was possible below 355 V for all the conditions tested, with argon and krypton having a lower mean breakdown voltage of 290 V and 300 V respectively, compared to 330 V for xenon, in line with the classical Paschen theory.

7.1.5 HEATING AND TRANSITION

The *V-I* characterisation of the HHC heating & transition phase demonstrated the ability of the HHC to start from room temperature to a thermionically emitting 5 A keeper discharge within 50 seconds, compared with 10-20 minutes required for a conventional cathode [26]. Polk recommended a heater power of 240 W with a heating time of 17 mins for their LaB_6 HC, which corresponds to a heating energy of 234.6 kJ. In contrast the HHC requires a total supply power of only 38.2 kJ to ignite within 50 s, and with just a mere 9.3 kJ consumed through the plasma load. This significant reduction in ignition energy is due to the direct plasma heating of the emitter, thus only the emitter or even the emitter surface is required to be at thermionic temperature to enable operation. These results demonstrate the clear advantage in ignition power of this heaterless system in comparison to conventional ignition, while also overcoming the melting issues encountered with prior HHC ignition [27].

7.1.6 NOMINAL OPERATION

The UoS-HHC has demonstrated an anode discharge current of up to 30 A, which is one of the highest currents achieved by a dedicated in-space heaterless hollow cathode with the keeper floating. This operation was conducted with a xenon mass flow rate of 13 sccm. The anode discharge performance has been compared with a well-established conventionally heated LaB_6 HC from JPL. Notwithstanding the oversimplicity of this direct cathode comparison, due to the lack of standardised cathode testing, the high similarity found in the cathode's operational performance trends indicates the HHCs power performance in steady state is not degraded by the novel heaterless ignition design changes. Thus, the findings of this nominal performance

characterisation combined with that of the ignition characterisation provide proof of concept of this novel heaterless ignition system.

7.1.7 GAS AND PRESSURE INFLUENCES

For the first time the pressure and gas influence on HHC operation has been investigated with emitter thermal diagnostics, allowing direct characterisation of these parameters influence on the emitter temperature which determines the emitter evaporation rate and thus lifetime. The HHC gas pressure in the open keeper backfilled configuration with xenon has been found to have a significant influence on the operational keeper voltage and emitter temperature. The keeper voltage increases by ~20% from 10 to 2 mbar. Additionally, the lower pressure has a ~15% increase in emitter temperature at low currents, below 0.7 A, and a more modest increase of 2.5% at 1.3 A. These tests indicate the emitter temperature, which is a function of emitter lifetime, decreases with higher pressure, and as such, the keeper orifice and mass flow rate, should support such nominal operation. The ignition was empirically found to be most stable and diffusive from 4-7 mbar across all operational gases.

The gas species has also been found to have a strong influence on the emitter temperature, with argon resulting in the highest emitter temperatures, then krypton and xenon. Emitter temperature differences are over 150 °C between xenon and argon at a keeper discharge of 0.5 A. These higher emitter temperatures with argon, and krypton correspond to higher operational voltages. These combined effects are likely the influence of the higher ionisation energy of argon and krypton compared with xenon.

7.1.8 THERMAL MEASUREMENTS

For the first time thermocouple measurements have been conducted on an HHC emitter, the results show clear changes in the emitter profile heating during ignition. As the discharge transitions from a secondary electron emission sustained discharge, in which the whole emitter is heated relatively uniformly, to the thermionic phase, the discharge heating power appears to significantly focus toward the emitter tip. The emitter tip is consistently recorded as the highest temperature, throughout the testing. Non-uniform discharges can result in reduced life from more localised erosion, and higher localised temperatures. The thermocouple measurements indicate that the emitter tip, measured by the pyrometer measurements, is close to the peak emitter temperature. Though, the emitter tip temperature is found to be significantly below the theoretically calculated thermionic emission, which may be due to LaB_6 transitioning to LaB_4 during operation, caused by lanthanum recycling as has been suggested by other groups [26], who have found similar discrepancies in the emitter temperature on conventional HCs.

7.1.9 PLASMA ELECTRON DENSITY MEASUREMENTS

Plasma Electron density measurements of the cathode-keeper gap with Kr and Ar have given insight into the internal plasma characteristics of the HHC, with the Kr density initially around $2.4*10^{20}$ m^{-3} compared with the $1*10^{20}$ m^{-3} for Ar at a keeper current of 0.4 A. A slight electron density rise occurs with current up to 1 A, though this is reversed with decreasing electron density beyond 1 A. This electron density decrease is likely due to the discharge cross section increasing, and thus causing a decrease in the average electron density measured, while the core plasma density increases. These electron plasma density values are similar orders of magnitude to that of conventional LaB_6 cathodes [23]. Experimental characterisation of this HHC plasma is significant to enable future modelling and optimisation efforts.

7.2 RECOMMENDATIONS FOR FUTURE RESEARCH

The current investigation on the heaterless ignition, has resulted in the development of a novel HHC ignition method, with a successful proof of concept. This opens an exciting development and research route towards space rating the system. Additionally, there are remaining areas in which the understanding of the underlying physics of the operation can be enhanced, to support performance and lifetime optimisation. The following sections outline the recommendations towards such research.

7.2.1 LIFETIME ANALYSIS

Although proof of concept has been achieved which is a significant step forward with this novel HHC concept, for progression toward being space rated, a substantially higher lifetime demonstration is required. Critically as the main difference between this HHC and conventional HC system is the ignition procedure, demonstration of ignition cycling is crucial, with a first milestone of 1000 cycles being recommended. Such cycling can include nominal steady state operation, such that both steady state operation, and ignitions are tested within the same experimental campaign. The objective of such a campaign should be to firstly demonstrate the reliability of sustained operation of the technology, and secondly, determine the life limiting mechanisms of the HHC operation, and thus identify which design features require analysis and improvement to further extend operational lifetime.

Already within the testing conducted design improvements have been identified, such as finding that the downstream emitter face may induce less uniform emission and localise the discharge attachment at that emitter edge during nominal operation, as indicated by the thermal measurements. A potential remedy would be to place a non-constrictive orifice downstream of the emitter, which acts as a high work function barrier, preventing discharge attachment on that

emitter face and edge, as depicted in Figure 7.1. With such a non-constrictive orifice the discharge should increasingly utilize the hollow cathode effect, increasing electron production efficiency as well as being more uniformly attached across the emitter, and hence increasing operational lifetime.

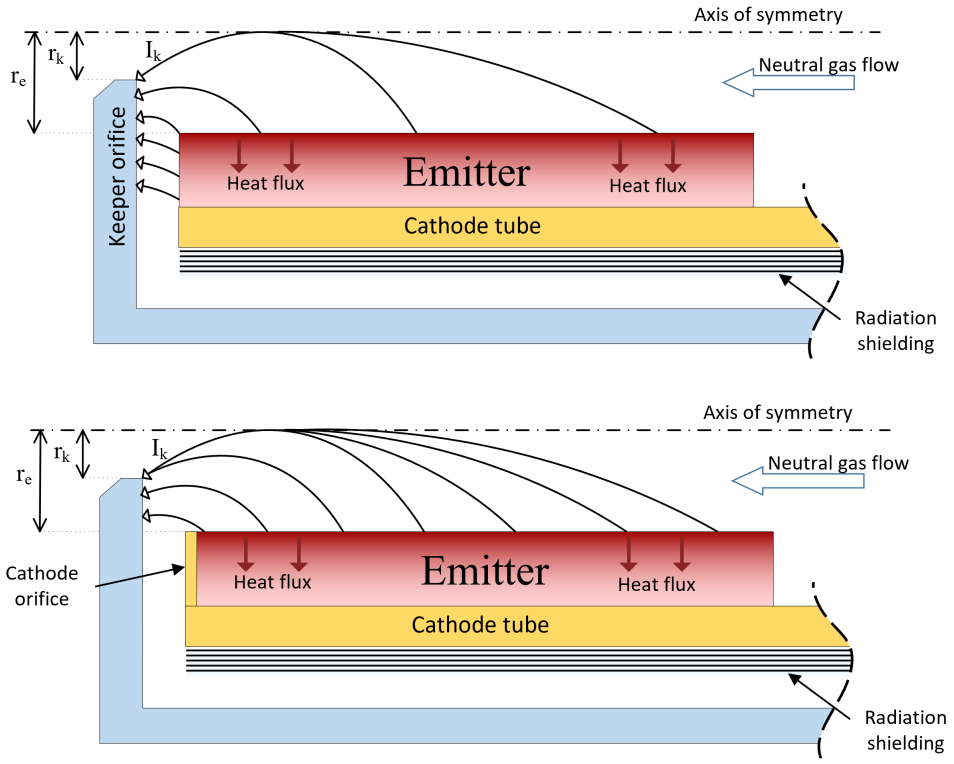

Figure 7.1: Diagram of the perceived current attachment during a nominal keeper discharge, with the original cathode configuration (top), and with the suggested new cathode orifice (bottom)

For lifetime optimization, it is critical to assess the emitter and keeper erosion during breakdown, heating, transition and nominal operation. Testing has already shown no significant erosion from the breakdown phase after completion of ~800 ignitions. Though the heating/transition phase requires further investigation, that can be conducted through dedicated heating phase cycling, with periodic mass measurements of the emitter and keeper. The same method can be applied to steady state nominal thermionic operation, with an anode discharge. As the keeper orifice is essentially a conventional cathode orifice during nominal operation, research focus should be placed on the erosion of this constrictive keeper orifice as well as the emitter.

7.2.2 IGNITION CONTROL SYSTEM OPTIMIZATION

The ignition control system developed has achieved the purpose of allowing standard off the shelf power supplies to reliably ignite the HHC, utilizing other cost effective off the shelf components,

namely thermistors and inductors. Although this is very useful for ground testing and near future research and development of the system, eventually for flight purposes an enhanced power processing unit is required. Such a system cannot use large inductors due to the large physical size; hence further optimization should investigate the removal of this subcomponent. To this effect it is most beneficial to develop a dedicated HHC power processing unit, which directly provides the stable current controlled power to the system, limiting any surges and stabilising the heating phase, while minimizing any waste power.

7.2.3 PHYSICS OF DISCHARGE OPERATION

Developing a model for the HHC is of importance to gaining better understanding of the HHC physics of operation. There has been a significant international effort for conventional cathode modelling, primarily on steady state HC operation, by JPL which developed the OrCa2D model [44, 45, 89, 176], and more recent attempts by Sary [90, 91]. Unfortunately, such models are not open source and require significant development time to re-produce, due to the coupled plasma, thermal, and flow physics nature. Hence development of a model using commercially available multi-physics software, such as COMSOL, or open source alternatives, such as OpenFOAM would be significantly beneficial to the overall field.

Initial modelling of HHC steady state operation can give further insight into the keeper orifice operation and can support erosion estimation for the orifice. The start-up modelling would be of interest, though this has not yet been substantially addressed for conventional cathodes let alone HHCs. Start-up adds complexity of the breakdown, Townsend discharge physics, and the secondary emission, during the heating phase for HHCs. A more practical option would be to model the secondary emission heating stage as steady state, to better understand that phase.

To develop these models for the HHC, more empirical data is required for validation. Critically, spatially resolved electron density, and temperature measurements, which may be conducted spectrographically, or alternatively utilising Langmuir probes as Goebel has shown [92], which can also provide the spatially resolved plasma potentials.

7.2.4 MISSION READINESS

Testing in the anode configuration allows easier assessment of the system and provides a benchmark for performance. Though the lack of standardisation, as mentioned in Section 6.6, makes it challenging to compare performance within the field. Therefore, when a cathode is coupled with a thruster toward mission development, it is challenging to determine if the cathode is operating well, or if the thruster configuration is ultimately supporting the operation. It has been shown that the anode configuration has a large influence on cathode behaviour [31], such that

standardisation of anode geometry and positioning should be set for HC power classes, to enable benchmark testing within the field.

As one of the main benefits of the HHC operation is the cost reduction, a potential mission class for this HHC is a mega constellation, which involves networks of hundreds to thousands of satellites in LEO. The One Web constellation [16] as an example, has a planned launch of around 900 satellites, with expansion to over two thousand satellites in consideration currently. As such this HHC system could be scaled for the adequate size thruster for these missions due to the large cost reduction. Furthermore, the HHC tests for the breakdown and heating phase with alternative propellants, Kr and Ar, have yielded promising results. Alternative propellants are being actively researched in the field currently [177], due to the rising Xenon costs, and critically for mega constellations there could be huge savings from development to flight with the system utilising such propellant alternatives. The Space X Starlink constellation [178], has 7000-12000 satellites in total planned and 60 currently operational, each utilising HETs with Kr propellant due to the mentioned cost benefits. HETs can be operated with only one cathode in comparison to GIEs, therefor a HET coupled with the HHC operating with Kr would be a very cost-effective system, and evidently suitable for such constellations. As such, further full ignition HHC testing should be conducted with these alternative propellants and additionally with the HHC coupled with a HET to determine the technology's suitability for such missions.

REFERENCES

1. Daykin-Iliopoulos, A.J.N., et al., *Characterisation of a Hollow Cathode Apparatus for High-Density Plasma Antenna Applications.* Plasma Sources Science and Technology [In preparation for submission], 2019.

2. Daykin-Iliopoulos, A.J.N., I.O. Golosnoy, and S.B. Gabriel, *Hollow Cathode Apparatus*, B.N.P. Office, Editor. 2018.

3. Daykin-Iliopoulos, A.J.N., I.O. Golosnoy, and S.B. Gabriel, *Development of High Current Heaterless Hollow Cathode*, in *Space Propulsion 2018*. 2018: Seville, Spain. p. 1-8.

4. Daykin-Iliopoulos, A.J.N., I.O. Golosnoy, and S.B. Gabriel. *Thermal Profile of a Lanthanum Hexaboride Heaterless Hollow Cathode*. in *35th International Electric Propulsion Conference*. 2017. Atlanta, USA.

5. Daykin-Iliopoulos, A.J.N., I.O. Golosnoy, and S.B. Gabriel. *Influence of Power Throughout Heaterless Hollow Cathode Ignition*. in *Space Propulsion 2016*. 2016. Rome.

6. Daykin-Iliopoulos, A.J.N., et al. *Investigation of Heaterless Hollow Cathode Breakdown*. in *34th International Electric Propulsion Conference*. 2015. Hyogo-Kobe, Japan.

7. Gabriel, S.B., I.O. Golosnoy, and A.J.N. Daykin-Iliopoulos, *Electric Propulsion at the University of Southampton*, in *Electric Propulsion Innovation & Competitiveness Workshop 2017*. 2017: Madrid, Spain. p. 14.

8. Gabriel, S.B., I.O. Golosnoy, and A.J.N. Daykin-Iliopoulos. *The Development of Heaterless Hollow Cathodes at the University of Southampton*. in *The Electric Propulsion Innovation & Competitiveness (EPIC) Workshop.* 2014. Brussels: The Electric Propulsion Innovation & Competitiveness (EPIC) Workshop.

9. Edison, T.A., *Electrical Indicator*. 1883: USA.

10. Paxton, W., *Thermionic Electron Emission Properties of Nitrogen-Incorporated Polycrystalline Diamond Films* 2013, Vanderbilt University.

11. Becquerel, E., *Rescherches Sur La Transmission De L'electricite Au Travers Des Gaz a Des Temperatures Elevees.* Annales de Chimie et de Physique, 1853. **39**: p. 48.

12. Fleming, J.A., *Instrument for Converting Alternating Electric Currents into Continuous Currents*. 1905.

13. Jensen, K.L., *Introduction to the Physics of Electron Emission*. 2017: Wiley.

14. Sovey, J.S., V.K. Rawlin, and M.J. Patterson, *Ion Propulsion Development Projects in U.S.: Space Electric Rocket Test I to Deep Space 1.* Journal of Propulsion and Power, 2001. **17** (3): p. 517-526.

15. Lev, D. *The Technological and Commercial Expansion of Electric Propulsion in the Past 24 Years*. in *35th International Electric Propulsion Conference*. 2017. Atlanta, USA.

16. OneWeb. *Http://Www.Oneweb.World/*. 2018 28/07/2018].

17. Betzendahl, R., *The 2014 Rare Gases Market Report*. 2014, Cryo-gas: Chicago.

18. Parissenti, G. and N. Koch. *Non Conventional Propellants for Electric Propulsion Applications*. in *Space Propulsion 2010*. 2010. San Sebastian, Spain.

19. Rudwan, I. and S. Gabriel. *Investigation of the Discharge Characteristics of the T6 Hollow Cathode Operating on Several Inert Gases and a Kr/Xe Mixture*. in *11th International Congress on Plasma Physics*. 2003. Sydney, Australia.

20. Little, P. and A. Engel, *The Hollow-Cathode Effect and the Theory of Glow Discharges.* Proceedings of the Royal Society of London. Series A, Mathematical and Physical Sciences, 1954. **224** (1157): p. 209-227.

21. Caixia, Q., K. Xiaolu, and Y. Shuilin. *Hollow Cathode Life Test for the 80 Mn Hall Thruster*. in *33st International Electric Propulsion Conference*. 2013. Washington, USA.

22. Zakany, J. and L. Pinero. *Space Station Cathode Ignition Test Status at 32,000 Cycles*. in *25th International Electric Propulsion Conference*. 1997. Cleveland, USA.

23. Goebel, D. and E. Chu, *High-Current Lanthanum Hexaboride Hollow Cathode for High-Power Hall Thrusters.* Journal of Propulsion and Power, 2014. **30** (1): p. 35-40.

24. Pollard, M. and D. Lamprou. *The Design, Development, Manufacture and Test of an Electric Propulsion System for Small Spacecraft*. in *Space Propulsion 2012*. 2012. Bordeaux, France.

25. Gulczinksi, F., R. Spores, and J. Stuhlberger. *In-Space Propulsion*. in *AIAA/ICAS International Air & Space Space Symposium and Exposition*. 2003. California, USA.

26. Polk, J., D. Goebel, and P. Guerreo. *Thermal Characteristics of a Lanthanum Hexaboride Hollow Cathode*. in *International Electric Propulsion Conference*. 2015. Kobe, Japan.

27. Schatz, M. *Heaterless Ignition of Inert Gas Ion Thruster Hollow Cathodes*. in *18th International Electric Propulsion Conference*. September 30-October 2, 1985. Alexandria, USA.

28. Lieberman, M. and A. Lichtenberg, *Principles of Plasma Discharges and Materials Processing*. 2005, Hoboken: Wiley.

29. Townsend, J., *The Theory of Ionization of Gases by Collision*. 1910, London Constable & Company: London.

30. Aston, G. *Ferm Cathode Operation in the Test Bed Ion Engine*. in *17th International Electric Propulsion Conference*. May 28-31, 1984. Tokyo, Japan.

31. Goebel, D., et al. *High Current Lanthanum Hexaboride Hollow Cathode for 20-200 Kw Hall Thrusters*. in *35th International Electric Propulsion Conference*. 2017. Atlanta, USA: 35th International Electric Propulsion Conference.

32. Von Engel, A., *Ionized Gases*. 1965, Oxford: Clarendon Press.

33. Grubisic, A., S. Gabriel, and D. Fearn. *Preliminary Thrust Characterization of the T-Series Hollow Cathodes for All-Electric Spacecraft*. in *30th International Electric Propulsion Conference*. 2007. Florence, Italy.

34. Arkhipov, B. *Development and Research of Heaterless Cathode-Neutralizer for Linear Hall Thrusters (Lhd) and Plasma Ion Thrusters (Pit)*. in *25th International Electric Propulsion Conference*. October, 1997. Cleveland, USA.

35. Albertoni, R. *Preliminary Characterization of a Lab6 Hollow Cathode for Low-Power Hall Effect Thrusters*. in *33rd International Electric Propulsion Conference*. October 6-10, 2013. Washington, USA.

36. Vekselman, V., *Characterization of a Heaterless Hollow Cathode.* Journal of Propulsion and Power, 2013. **29** (2): p. 475-486.

37. Ouyang, L., et al., *Experiment Research on Heaterless Hollow Cathode Cold Ignition Characteristic.* Journal of Propulsion Technology, 2015. **37** (6): p. 1195-1200.

38. Lev, D. and L. Appel. *Heaterless Hollow Cathode Technology - a Critical Review*. in *SPACE PROPULSION 2016*. 2016. ROME, ITALY.

39. Goebel, D., R. Watkins, and K. Jameson, *Lab6 Hollow Cathodes for Ion and Hall Thrusters.* Journal of Propulsion and Power, 2007. **23** (3): p. 552-558.

40. Lev, D., D. Mykytchuk, and G. Alon. *Heaterless Hollow Cathode Characterization and 1,500 Hr Wear Test*. in *52nd AIAA/SAE/ASEE Joint Propulsion Conference*. 2016. Salt Lake City, USA.

41. Loyan, A., et al. *Researching of Electric Propulsion Quick Start Problem for a Spacecraft Orientation System*. in *3rd International Conference on Spacecraft Propulsion*. 2000. Cannes.

42. Fearn, D., A. Cox, and D. Moffitt, *An Investigation of the Initiation of Hollow Cathode Discharges*. 1976, Royal Aircraft Estarblishment: London.

43. Kaufman, H. and J. Kahn. *Hollow Cathode without Low-Work-Function Insert*. in *International Electric Propulsion Conference*. 2005. Princeton, USA.

44. Katz, I., et al., *Insert Heating and Ignition in Inert-Gas Hollow Cathodes.* IEEE Transactions on Plasma Science, 2008. **36** (5): p. 2199-2206.

45. Mikellides, I., D. Goebel, and B. Jorns, *Numerical Simulations of the Partially Ionized Gas in a 100-a Lab6 Hollow Cathode.* IEEE Transactions on Plasma Science, 2015. **43** (1): p. 173-184.

46. Goebel, D. and I. Katz, *Hollow Cathodes*, in *Fundamentals of Electric Propulsion: Ion and Hall Thrusters*. 2008, Willy: Hoboken. p. 243-315.

47. Arhipov, B., et al. *Development and Application of Electric Thrusters at Edb "Fakel"* in *25th International Electric Propulsion Conference*. 1997. Cleveland, USA.

48. Jack, M. and S. Patterson, and Fearn, D. *The Effect of the Keeper Electrode on Hollow Cathode Characteristics*. in *36th AIAA/ASME/SAE/ASEE Joint Propulsion Conference and Exhibit*. 2000. Las Vegas.

49. Fearn, D. and C. Philip, *An Investigation of Physical Processes in a Hollow Cathode Discharge.* AIAA Journal, 1973. **11** (2): p. 131-132.

50. Fearn, D. and S. Patterson. *The Hollow Cathode - a Versatile Component of Electric Thrusters*. in *Spacecraft Propulsion, Third International Conference*. 10-13 October, 2000. Cannes, France.

51. Philip, C.a.F., D., *Recent Hollow Cathode Investigations at the Royal Aircraft Establishment.* AIAA Journal, 1973. **12** (10): p. 1319-1325.

52. Lev, S., et al. *Development of a Low Current Heaterless Hollow Cathode for Hall Thrusters*. in *34th International Electric Propulsion Conference*. 2015. Kobe, Japan.

53. Rand, L. and J. Williams, *A Calcium Aluminate Electride Hollow Cathode.* IEEE Transactions on Plasma Science, 2015. **43** (1): p. 190-194.

54. Hwang-Jin, H., *Physical Processes in Hollow Cathode Discharge*. 1989, Naval Postgraduate School: California.

55. Loyan, A., et al. *Middle Power Hall Effect Thrusters with Centrally Located Cathode*. in *33rd International Electric Propulsion Conference*. 2013. Washington, USA.

56. Koshelev, N., S. Lobov, and A. Loyan. *Experimental Investigation of a Gas Propellant Consumption Oscillation When Self-Heated Hollow Cathode Is Starting from Cold State*. in *26th International Electric Propulsion Conference Publications*. 1999. Kitakyushu, Japan.

57. Koshelev, N., A. Loyan, and A. Oransky. *Pecularities of Hollow Cathodes Erosion at Non-Incandescent Switching on_1995*. in *24th International Electric Propulsion Conference Publications* 1995. Moscow, Russia.

58. Lobov, S. and A. Loyan. *Physic-Mathematics Model of a Self-Heated Hollow Cathode Electric Discharge Evolution*. in *26th International Electric Propulsion Conference*. 1999. Kitakyushu, Japan.

59. Loyan, A. and N. Koshelev. *The Results of Researching of Low-Current Selfheated Hollow Cathodes on Electric Current Range from 0,3 up to 0,5 A*. in *27th International Electric Propulsion Conference*. 2001. Pasadena, USA

60. Koshelev, N. *Investigation of Hollow Cathode for Low Power Hall Effect Thruster*. in *30th International Electric Propulsion Conference*. September 17-20, 2007. Florence, Italy.

61. Loyan, A., A. Oransriy, and E. Ichenko. *High-Current Self-Heated Hollow Cathodes with Operation Current More Than 25 A. State and Development*. in *27th International Electric Propulsion Conference*. 2001. Pasadena, USA

62. Loyan, A., et al. *Results of Tests of High-Current Cathode for High-Power Hall Thruster*. in *32nd International Electric Propulsion Conference*. 2011. Wiesbaden, Germany.

63. Vekselman, V. *A Comparative Study of Heaterless Hollow Cathode: 2d Pic Modeling Vs. Experiment*. in *33rd International Electric Propulsion Conference*. October 6-10, 2013. Washington, USA.

64. Pedrini, D., et al. *Development of a Lab6 Cathode for High-Power Hall Thrusters*. in *International Electric Propulsion Confrence*. 2015. Kobe, Japan.

65. Shastry, R. and G.C. Soulas, *Post-Test Inspection of Nasa's Evolutionary Xenon Thruster Long-Duration Test Hardware: Discharge and Neutralizer Cathodes*, in *52nd AIAA/SAE/ASEE Joint Propulsion Conference July*. 2016: Salt Lake City, USA.

66. Polk, J.E., et al., *Barium Depletion in the Nstar Discharge Cathode after 30,472 Hours of Operation*, in *46th AIAA/ASME/SAE/ASEE Joint Propulsion Conference & Exhibit*. 2010: Nashville, USA.

67. Arkhipov, A., *Hlc Power System*. 1994: The Russian Federation.

68. Raizer, Y., *Gas Discharge Physics*. 1991, Moscow: Springer-Verlag.

69. Howatson, A., *Introduction to Gas Discharges*. 1976, OXFORD: Pergamon Press Ltd.

70. Wang, J., *Simulation of Gas Discharge in Tube and Paschen's Law.* Optics and Photonics Journal, 2013: p. 313-317.

71. Tighe, W., K. Chien, and D. Goebel. *Hollow Cathode Ignition Studies and Model Development*. in *29th International Electric Propulsion Conference*. 2005. Princeton, USA.

72. Lide, D., *Crc Handbook of Chemistry and Physics*. 2003, Florida: CRC Press.

73. Paschen, F., *Ueber Die Zum Funkenübergang in Luft, Wasserstoff Und Kohlensäure Bei Verschiedenen Drucken Erforderliche Potentialdifferenz.* Annalen der Physik, 1889. **273** (5): p. 69-96.

74. Marić, D., et al., *Gas Breakdown and Secondary Electron Yields.* The European Physical Journal D, 2014. **68**: p. 155-162.

75. Spyrout, N., et al., *Why Paschen's Law Does Not Apply in Low-Pressure Gas Discharges with Inhomogeneous Fields.* Journal of Physics D: Applied Physics, 1994. **28** (4): p. 701-710.

76. Eichhorn, H., K. Schoenbach, and T. Tessnow, *Paschen's Law for a Hollow Cathode Discharge* Applied Physics Letters, 1993. **63** (18): p. 2481-2483.

77. Pak, H. and M. Kushner, *Breakdown Characteristics in Nonplanar Geometries and Hollow Cathode Pseudospark Switches.* Journal of Applied Physics, 1992. **71** (1): p. 94-100.

78. Pak, H. and M. Kushner, *Simulation of the Switching Performance of an Optically Triggered Pseudo - Spark Thyratron.* Journal of Applied Physics, 1989. **66** (1): p. 2325-2331.

79. Boeuf, J. and L. Pitchford, *Pseudospark Discharges Via Computer Simulation.* IEEE Transactions on Plasma Science, 1991. **19** (2): p. 286-296

80. Roth, J.R., *Industrial Plasma Engineering: Volume 1: Principles*. 1995. 339.

81. Takaki, K., D. Taguchi, and T. Fujiwara, *Voltage–Current Characteristics of High-Current Glow Discharges.* 2001. **78** (18): p. 2646-2648.

82. Brown, S., *Basic Data of Plasma Physics*. 1959, New York: Technology Press and Wiley.

83. Saifutdinov, A., et al. *Dynamics Contraction of Dc Glow Discharge in Argon*. in *Journal of Physics: Conference Series: VII Conference on Low Temperature Plasma in the Processes of Functional Coating Preparation*. 2016.

84. Pekarek, L., *Ionization Waves (Striations) in a Discharge Plasma.* Soviet Physics Uspekhi, 1968. **11** (2): p. 188-200.

85. Gomes, M., B. Sismanoglu, and J. Amorim, *Characterization of Microhollow Cathode Discharges.* Brazilian Journal of Physics, 2009. **39** (1): p. 25-31.

86. Marić, D., et al. *Hollow Cathode Discharges: Volt-Ampere Characteristics and Space-Time Resolved Structure of the Discharge*. in *Journal of Physics: Conference Series: 2nd*

Int. Workshop on Non-equilibrium Processes in Plasmas and Environmental Science. 2009.

87. Lev, D., et al. *Low Current Heaterless Hollow Cathode Development Overview*. in *35th International Electric Propulsion Conference*. 2017. Atlanta, USA.

88. Schottky, W., Phys. Z., 1914. **15**: p. 872.

89. Mikellides, I.G., *Effects of Viscosity in a Partially Ionized Channel Flow with Thermionic Emission.* Physics of Plasmas, 2009. **16** (1): p. 013501.

90. Sary, G., L. Garrigues, and J.-P. Boeuf, *Hollow Cathode Modeling: I. A Coupled Plasma Thermal Two-Dimensional Model.* Plasma Sources Science and Technology, 2017. **26** (5): p. 055007.

91. Sary, G., L. Garrigues, and J.-P. Boeuf, *Hollow Cathode Modeling: Ii. Physical Analysis and Parametric Study.* Plasma Sources Science and Technology, 2017. **26** (5): p. 055008.

92. Goebel, D., K. Jameson, and I. Mikellades, *Plasma Characterization with Miniature Fast-Scanning Probes.* Journal of Applied Physics, 2005. **98** (10): p. 113302.

93. Konuma, M., *Film Deposition by Plasma Techniques*. 1992, New York: Springer.

94. Jiittner, B., *Properties of Arc Cathode Spots.* J. Phys. IV France, 1997. **7** (C4): p. 31-45.

95. Bochkarev, M. and A. Murzakaev. *Investigations of Vacuum Arc Cathode Spots with High Temporal and Spatial Resolution*. in *18th International Symposium on Discharges and Electrical Insulation in Vacuum*. 1998. Eindhoven, The Netherlands.

96. Benilov, M., *Multiple Solutions in the Theory of Dc Glow Discharges and Cathodic Part of Arc Discharges. Application of These Solutions to the Modeling of Cathode Spots and Patterns: A Review.* Journal of Plasma Sources Science and Technology, 2014. **23** (5): p. 1-23.

97. Lefort, A. and M. Abbaoui. *Theory About Cathode Arc Root: A Review*. in *1st International Symposium on Electrical Arc and Thermal Plasmas in Africa*. (2012). Africa.

98. Beilis, I., et al., *Structure and Dynamics of High-Current Arc Cathode Spots in Vacuum.* J. Phys. D: Appl. Phys. , 1997. **30**: p. 119 -130.

99. Hantzsche, E., *Theory of Cathode Spot Phenomena.* Physica B+C, 1981. **104** (1-2): p. 3-16.

100. Drouet, M., *Influence of the Background Gas Pressure on the Expansion of the Arc-Cathode Plasma; .* IEEE Trans. Plasma Sci., 1985. **13**: p. 285-287.

101. Ledernez, L., F. Olcaytug, and G. Urban, *Inter-Electrode Distance and Breakdown Voltage in Low Pressure Argon Discharges.* Contributions to Plasma Physics, 2012. **52** (4): p. 276–282.

102. Gruner, K.-D., *Principles of Non-Contact Temperature Measurement*. 2003, Raytek GmbH.

103. Storms, E.K., *The Emissivity of Lab6 at 650 Nm.* 1979. **50** (6): p. 4450-4450.

104. Michalski, L., *Temperature Measurement*. 2001, Chicago: Wiley.

105. Omega, *Tungsten-Rhenium Twisted Beaded Thermocouples*. 2016, OMEGA: London, UK.

106. Polk, J., D. Goebel, and P. Guerreo. *Thermal Characteristics of a Lanthanum Hexaboride Hollow Cathode*. in *34th International Electric Propulsion Conference*. 2015. Kobe, Japan.

107. Cotronics, *Resbond 904 Adhesive & Coating-Bonds-Coats-Protects*. 2016, Cotronics Corporation: New York, USA.

108. Konjević, N., M. Ivković, and N. Sakan, *Hydrogen Balmer Lines for Low Electron Number Density Plasma Diagnostics.* Spectrochimica Acta Part B: Atomic Spectroscopy, 2012. **76**: p. 16-26.

109. UoS, et al., *Plasma Antenna Technologies*. 2017-2020, EU Horizon 2020: UK, Italy, Greece.

110. Palomares, J.M., et al., *Hβ Stark Broadening in Cold Plasmas with Low Electron Densities Calibrated with Thomson Scattering.* Spectrochimica Acta Part B: Atomic Spectroscopy, 2012. **73**: p. 39-47.

111. Siepa, S., et al., *On the Oes Line-Ratio Technique in Argon and Argon-Containing Plasmas.* Journal of Physics D: Applied Physics, 2014. **47** (44): p. 445201.

112. Kunze, H.-J., *Introduction to Plasma Spectroscopy*. 1 ed. 2009: Springer-Verlag Berlin Heidelberg. 242.

113. Goebel, D.M., et al., *Life Model for Lanthanum Hexaboride Hollow Cathodes for High-Power Hall Thrusters*, in *35th International Electric Propulsion Conference*. 2017: Atlanta, USA.

114. Scialdone, J.J. *Pressure and Purging Effects on Material Outgassing and Evaporation*. in *Materials in a Space Environment*. 2003.

115. Richardson, O., *Electron Theory of Matter.* Cambridge Physical Series, 1914. **23**: p. 594-627.

116. Kohl, W., *Handbook of Materials and Techniques for Vacuum Devices*. 1967, New Yor: Reinhold.

117. Schottky, W., *Concerning the Discharge of Electrons from Hot Wires with Delayed Potential.* Annalen der Physik, 2014. **44** (15): p. 1011-1032.

118. Forrester, A., *Large Ion Beams*. 1988, New York: Wiley-Interscience.

119. Child, C.D., *Discharge from Hot Cao.* Physical Review (Series I), 1911. **32** (5): p. 492-511.

120. Chu, E. and D.M. Goebel, *High-Current Lanthanum Hexaboride Hollow Cathode for 10-to-50-Kw Hall Thrusters.* Ieee Transactions On Plasma Science, 2012. **40** (9).

121. Drobny, C., M. Tajmar, and R.E. Wirz, *Development of a C12a7 Electride Hollow Cathode*, in *The 35th International Electric Propulsion Conference*. 2017: Atlanta, Georgia, USA.

122. Kim, S.W., et al., *Synthesis of a Room Temperature Stable 12cao·7al2o3 Electride from the Melt and Its Application as an Electron Field Emitter.* Chemistry of Materials, 2006. **18** (7): p. 1938-1944.

123. Caruso, N.R.S. and M.S. McDonald, *Thermionic Emission Measurements of 12(Cao)-7(Al2o3) Electride in a Close-Spaced Diode*, in *The 35th International Electric Propulsion Conference*. 2017: Atlanta, Georgia, USA.

124. Williams, J.D., J.R. Sanmartin, and L.P. Rand, *Low Work-Function Coating for an Entirely Propellantless Bare Electrodynamic Tether.* IEEE Transactions on Plasma Science, 2012. **40** (5): p. 1441-1445.

125. Rand, L.P., R.M. Waggoner, and J.D. Williams. *Hollow Cathode with Low Work Function Electride Insert*. in *ASME 2011 International Mechanical Engineering Congress & Exposition*. 2011. Denver, Colorado, USA.

126. Rand, L.P. and J.D. Williams. *Instant Start Electride Hollow Cathode*. in *The 33rd International Electric Propulsion Conference*. 2013. Washington, D.C., USA.

127. Toda, Y., et al., *Intense Thermal Field Electron Emission from Room-Temperature Stable Electride.* 2005. **87** (25): p. 254103.

128. McDonald, M.S. and N.R.S. Caruso, *Ignition and Early Operating Characteristics of a Low-Current C12a7 Hollow Cathode* in *35th International Electric Propulsion Conference*. 2017: Atlanta, Georgia, USA.

129. Gibson, J., G. Haas, and R. Thomas, *Investigation of Scandate Cathodes: Emission, Fabrication and Activation Processes.* IEEE Transactions on Electron Devices, 1989. **36**: p. 209–214.

130. Shuguang, W. *Scandate Cathode for Twt*. in *The 5th International Vacuum Electron Sources Conference*. 2005.

131. Gibson, J.W., G.A. Haas, and R.E. Thomas, *Investigation of Scandate Cathodes: Emission, Fabrication, and Activation Processes.* IEEE Transactions on Electron Devices, 1989. **36** (1): p. 209-214.

132. Lafferty, J., *Boride Cathodes.* Journal of Applied Physics, 1951. **22**: p. 299.

133. Kohl, W.H., *Handbook of Materials and Techniques for Vacuum Devices*. 1967: New York : Reinhold, [1967].

134. Storms, E. and D. Jacobson, *Work Function Measurement of Lanthanum-Boron Compounds.* IEEE Transactions on Plasma Science, 1978. **6**: p. 191-199.

135. Storms, E. and B. Mueller, *A Study of Surface Stoichiometry and Thermionic Emission Using Lab6.* Journal of Applied Physics, 1979. **50**: p. 3691-3698.

136. Trenary, M., *Surface Science Studies of Metal Hexaborides.* Science and Technology of Advanced Materials, 2012. **13**: p. 023002.

137. Kim, V., et al. *Electric Propulsion Activity in Russia*. in *27th International Electric Propulsion Conference, Pasadena*. 2001. California, USA.

138. Coletti, M., R. Marques, and S. Gabriel. *Discharge Hollow Cathode Design for a 4-Gridded Ion Engine*. in *IEEE Aerospace Conference*. 2010. Big Sky, USA.

139. Salhi, A., R. Myerst, and P. Turchit. *Experimental Investigation of a Hollow Cathode Discharge*. in *International Electric Propulsion Conference*. 1993. Seattle, USA.

140. Grubisic, A., *Microthrusters Based on the T5 and T6 Hollow Cathode* 2009, PhD Thesis: Southampton.

141. Goebel, D.M. and R.M. Watkins, *Compact Lanthanum Hexaboride Hollow Cathode.* REVIEW OF SCIENTIFIC INSTRUMENTS, 2010. **81**.

142. Goebel, D.M., J.T. Crow, and A.T. Forrester, *Lanthanum Hexaboride Hollow Cathode for Dense Plasma Production.* 1978. **49** (4): p. 469-472.

143. Leung, K.N., P.A. Pincosy, and K.W. Ehlers, *Directly Heated Lanthanum Hexaboride Filaments.* 1984. **55** (7): p. 1064-1068.

144. Polk, J.E., et al. *Demonstration of the Nstar Ion Propulsion System on the Deep Space One Mission*. in *The 27th International Electric Propulsion Conference*. 2001. Pasadena, USA.

145. Luntlberg, L.B., *A Critical Evaluation of Molybdenum and Its Alloys for Use in Space Reactor Core Heat Pipes*. 1981: University of California.

146. Hoffman, D., B. Singh, and J.H. Thomas, *Handbook of Vacuum Science and Technology*. 1997: Academic Press.

147. DiStefano, J.R., B.A. Pint, and J.H. DeVan, *Oxidation of Refractory Metals in Air and Low Pressure Oxygen Gas.* International Journal of Refractory Metals & Hard Materials, 2000. **18**: p. 237-243.

148. Gulbransen, E.A., K.F. Andrew, and F.A. Brassart, *Studies on the High Temperature Oxidation of Molybdenum, Tungsten, Niobium, Tantalum, Titanium, and Zirconium*. 1967: WESTINGHOUSE ELECTRIC CORPORATION Research Laboratories.

149. Klopp, W.D. and W.R. Witzke, *Mechanical Properties of Electron-Beam-Melted Molybdenum and Dilute Molybdenum-Rhenium Alloys*. 1972: NASA.

150. Leonhardt, T., et al. *Investigation of Mechanical Properties and Microstructure of Various Molybdenum Rhenium Alloys*. in *Space Technology and Applications International Forum*. 1999.

151. Schneibel, J.H., E.J. Felderman, and E.K. Ohriner, *Mechanical Properties of Ternary Molybdenum–Rhenium Alloys at Room Temperature and 1700k.* Scripta Materialia, 2008. **59** (2): p. 131-134.

152. Polk, J., *Arcing Issues with Poco Carbon Orifices*, A. Daykin-Iliopoulos, Editor. 2015.

153. Doerner, R.P., D.G. Whyte, and D.M. Goebel, *Sputtering Yield Measurements During Low Energy Xenon Plasma Bombardment.* 2003. **93** (9): p. 5816-5823.

154. Doerner, R.P., *Low-Energy Sputtering Yields of Tungsten and Tantalum.* 2005. **23** (6): p. 1545-1547.

155. Domonkos, M.T. and J. George J. Williams. *Investigation of Keeper Erosion in the Nstar Ion Thrust*. in *27th International Electric Propulsion Conference*. 2001. Pasadena, USA.

156. Goebel, D.M., et al., *Energetic Ion Production and Keeper Erosion in Hollow Cathode Discharges*, in *29th International Electric Propulsion Conference*. 2005.

157. Goebel, D.M., et al., *Keeper Wear Mechanisms in the Xips© 25-Cm Neutralizer Cathode Assembly*, in *31st International Electric Propulsion Conference*. 2009: Ann Arbor, USA.

158. Patterson, S.W. and D.G. Fearn. *The Generation of High Energy Ions in Hollow Cathode Discharges*. in *International electric propulsion conference*. 1999. Kitakyushu, Japan.

159. Latham, P.M., A.J. Pearce, and R.A. Bond. *Erosion Processes in the Uk-25 Ion Thruster*. in *International Electric Propulsion Conference*. 1991. Viareggio, Italy.

160. Goebel, D., et al., *Potential Fluctuations and Energetic Ion Production in Hollow Cathode Discharges.* Physics of Plasmas 2007. **14** (10): p. 50-62.

161. Gallimore, A. and J. Rovey, *Gas-Fed Hollow Cathode Keeper and Method of Operating Same*, U.o. Michigan, Editor. 2006: USA.

162. Hofer, R.R., D.M. Goebel, and R.M. Watkins, *Compact High Current Rare-Earth Emitter Hollow Cathode for Hall Effect Thrusters*, C.I.o. Technology, Editor. 2007: USA.

163. Praeger, M., A.J.N. Daykin-Iliopoulos, and S.B. Gabriel, *Vacuum Current Emission and Initiation in an Lab6 Hollow Cathode*, in *SPACE PROPULSION 2018*. 2018: Seville, Spain.

164. Becatti, G., et al., *Life Evaluation of a Lanthanum Hexaboride Hollow Cathode for High-Power Hall Thruster.* Journal of Propulsion and Power, 2017. **34** (4): p. 893-900.

165. Hecker, J.C., *Scientific Foundations of Vacuum Technique.* Journal of the American Chemical Society, 1962. **84** (15): p. 3032-3033.

166. Haring, M.M., *Treatise on Physical Chemistry.* Journal of Chemical Education, 1931. **8** (4): p. 772.

167. Roth, A., *Vacuum Technology*. 1976, Amsterdam ; New York : New York: North-Holland Pub. Co. ; sole distributors for the U.S.A. and Canada, American Elsevier Pub. Co.

168. Anderson, J., *Fundamentals of Aerodynamics*. 2001, Boston: McGraw-Hill.

169. Pedrini, D., et al., *Development of Hollow Cathodes for Space Electric Propulsion at Sitael.* 2017. **4** (2): p. 26.

170. Mikellides, I.G., et al., *Wear Mechanisms in Electron Sources for Ion Propulsion, Ii: Discharge Hollow Cathode.* Journal of Propulsion and Power, 2008. **24** (4): p. 866-879.

171. Company, M.I., *Table of Emissivity of Various Surfaces*. 2003.

172. Anders, A. and S. Anders, *The Working Principle of the Hollow-Anode Plasma Source.* Plasma Sources Science and Technology, 1995. **4** (4): p. 571-575.

173. Goebel, D. and E. Chu. *High Current Lanthanum Hexaboride Hollow Cathodes for High Power Hall Thrusters*. in *32nd International Electric Propulsion Conference*. 2011. Wiesbaden, Germany.

174. Snyder, J.S., et al., *Results of a 2000-Hour Wear Test of the Nexis Ion Engine*, in *29th International Electric Propulsion Conference*. 2005.

175. Snyder, J.S., et al., *Results of a 2000-Hour Wear Test of the Nexis Ion Engine* in *29th International Electric Propulsion Conference*. 2005.

176. Mikellides, I.G., I. Katz, and D.M. Goebel. *Numerical Simulation of the Hollow Cathode Discharge Plasma Dynamics*. in *29th International Electric Propulsion Conference*. 2005. Princeton, USA.

177. Fazio, N., S.B. Gabriel, and I.O. Golosnoy, *Alternative Propellants for Gridded Ion Engines*, in *Space Propulsion 2018*. 2018: Seville, Spain.

178. SpaceX. *Https://Www.Spacex.Com/*. 2019.